

Toppling Analysis of Precariously Balanced Rocks under Earthquake Excitation

Thesis by
Swetha Veeraraghavan

In Partial Fulfillment of the Requirements
for the Degree of
Doctor of Philosophy



California Institute of Technology
Pasadena, California

2015
(Defended May 7th 2015)

© 2015
Swetha Veeraraghavan
All Rights Reserved

Contents

Acknowledgements	v
Abstract	vii
1 Introduction	1
1.1 Motivation	1
1.2 Precariously balanced rocks	3
1.2.1 Formation and age	4
1.2.2 Friction coefficient	5
1.2.3 Past analysis	6
1.3 Rigid body dynamics	10
1.4 Outline	12
2 Rigid body dynamics algorithm	14
2.1 Algorithm	16
2.2 Validation of the algorithm	31
2.2.1 Rocking mode	33
2.2.2 Coupled rocking-sliding mode	34
2.3 Summary	35
3 Toppling analysis of precariously balanced rocks	36
3.1 Introduction	36
3.2 Modeling the geometry of the PBR-pedestal system	38
3.3 Material properties of PBR-pedestal system	43

3.4	Validation of the rigid body dynamics algorithm	44
3.5	Critical toppling intensity of the Echo Cliff PBR	47
3.5.1	Applications of fragility maps	61
3.6	Pacifico Rock	63
3.6.1	Toppling analysis of Pacifico rock	64
3.6.2	Comparison with PSHA	69
3.6.3	Comparison with synthetic ground motion simulations	75
3.7	Summary	77
4	Other Applications	80
4.1	Lower bounds on ground motion at Point Reyes during the 1906 San Francisco Earthquake from train toppling analysis	80
4.1.1	Overturning fragility of the train	84
4.1.2	Hypocenter location of the 1906 San Francisco earthquake	92
4.2	Estimating PGA and PGV from the maximum sliding displacement of a battery rack in Haiti	93
4.3	Estimating the minimum free-field PGA and PGV from maximum sliding displacement of nuclear spent fuel casks	101
4.4	Summary	105
5	Conclusions and future work	108
5.1	Conclusions	108
5.2	Future Work	111
	Appendices	113
	A Feasibility of LCP	114
	B Analytical solution for block's response mode	116
	C Supplemental figures for Echo Cliff PBR	123
	Bibliography	129

Acknowledgements

I am indebted to Caltech for providing me with the opportunity to work in a diverse and intellectually stimulating environment. I would like to thank the Civil Engineering department at Caltech, Southern California Earthquake Center (SCEC), United States Geological Survey (USGS), and National Science Foundation (NSF) for funding this project.

During the course of my graduate studies I had the privilege of working with two advisors. Firstly, I would like to convey my sincere gratitude to Dr. Swaminathan Krishnan for his guidance, patience, and support throughout my graduate study. Secondly, I would like to thank Dr. John F. Hall for co-advising me during the last two years of my graduate study and for his insightful comments which helped in improving the algorithm presented in this dissertation. Next, I would like to thank my thesis dissertation committee members Dr. Thomas H. Heaton, Dr. Kenneth W. Hudnut, and Dr. Dominiki Asimaki for their support and valuable insights on various aspects of the project.

Additionally, I would like to thank Dr. Kenneth W. Hudnut for introducing me to this interesting problem of analyzing precariously balanced rocks (PBRs) and for sharing the data required to create the 3-D geometry of the Echo Cliff PBR. I would like to thank Dr. Matthew Purvance, Dr. James Brune, and Dr. Richard Brune for sharing the results from shake table experiments, the data for creating the other rock models used in this dissertation and also for sharing their insights, understanding, and experience with PBRs. I would also like to thank Dr. Robert W. Graves and Dr. Ramses Mourhatch for sharing the synthetic ground motions from ShakeOut scenario and other similar earthquake scenarios rupturing parts of the San Andreas Fault. I would also like to thank Dr. Thomas H. Heaton and Dr. Susan Hough for suggesting other real world applications for my algorithm. Special thanks to Dr. Ramses Mourhatch for helping me understand the details of probabilistic seismic

hazard analysis.

I would like to thank all my friends and colleagues at Caltech, in particular, Thevamaran Ramathan, Mythili Thevamaran, Srivatsan Hulikal, Jeff Amelang, Aubrie Amelang, and Ellie Amelang for making my stay at Caltech a pleasant and memorable experience.

Finally, I would like to thank my family for their love and support. In particular, I would like to thank my husband, Navaneetha Krishnan, for helping me cope with the ups and downs of graduate study and for being a constant source of encouragement.

Abstract

Toppling analysis of a precariously balanced rock (PBR) can provide insights into the nature of ground motion that has not occurred at that location in the past and, by extension, realistic constraints on peak ground motions for use in engineering design. Earlier approaches have targeted simplistic 2-D models of the rock or modeled the rock-pedestal contact using spring-damper assemblies that require re-calibration for each rock. These analyses also assume that the rock does not slide on the pedestal. Here, a method to model PBRs in three dimensions is presented. The 3-D model is created from a point cloud of the rock, the pedestal, and their interface, obtained using Terrestrial Laser Scanning (TLS). The dynamic response of the model under earthquake excitation is simulated using a rigid body dynamics algorithm. The veracity of this approach is demonstrated by comparisons against data from shake table experiments. Fragility maps for toppling probability of the Echo Cliff PBR and the Pacifico PBR as a function of various ground motion parameters, rock-pedestal interface friction coefficient, and excitation direction are presented. The seismic hazard at these PBR locations is estimated using these maps. Additionally, these maps are used to assess whether the synthetic ground motions at these locations resulting from scenario earthquakes on the San Andreas Fault are realistic (toppling would indicate that the ground motions are unrealistically high).

Chapter 1

Introduction

1.1 Motivation

Critical structures such as nuclear power plants must be protected against earthquake damage by designing them to withstand intense shaking from very low-probability earthquakes (0.0001 per year or a 10000 yr recurrence interval [3, 23]) on regional faults. At a given location, this is currently taken from seismic hazard maps that are developed using probabilistic seismic hazard analysis with past earthquake history as one of the key inputs [104]. Unfortunately, ground motion records of past earthquakes exist only for the past century, and historical oral or written records extend only to the last millennium. As a consequence, characterizing fault behavior and potential ground motions over such long return periods as 10000 years can only be performed based on paleoseismic data with all its limitations and uncertainties [81]. These uncertainties may result in significant under- or over-prediction of seismic hazard in a region. For example, the ground acceleration at the North Anna nuclear power plant exceeded its design acceleration during the 2011 Mineral, Virginia earthquake, resulting in the shutdown of the plant [42].

To reduce the uncertainty, hazard derived from paleoseismic observations must be supplemented or constrained by other indirect methods. Brune [25] proposed a method to achieve this using sensitive geological structures like precariously balanced rocks (PBRs) which have existed in their present precarious conditions for thousands of years. Precariously balanced rocks (PBRs) like the ones shown in Fig. 1.1 are of particular interest. The age of most of these PBRs have been estimated to be at least 12,000 years [15]. The pres-

ence of a PBR in a region is evidence for the fact that earthquake shaking strong enough to overturn it has not occurred there during the rock's existence in that precarious condition. Therefore, the critical toppling intensity of a PBR in conjunction with its age may provide an independent constraint on historic peak ground motion, and, by extension, an estimate of future peak ground shaking in that region.

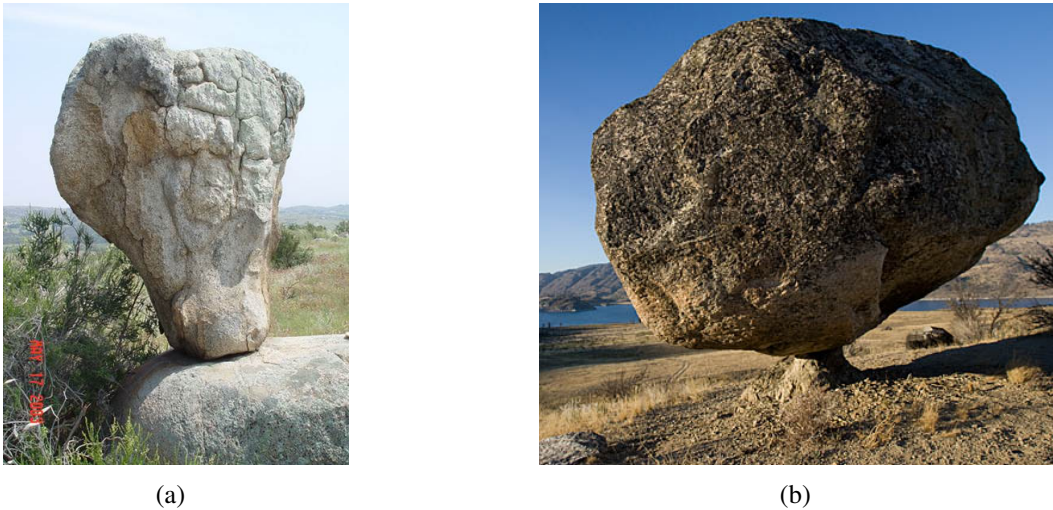


Figure 1.1: (a) Benton rock in Southern California [25]; and (b) Omak rock in Washington.

Fig. 1.2 shows the *PGA* levels from the 2014 national seismic hazard maps (NSHM) for Southern California corresponding to earthquakes that recur at least once every 2475 years. The black diamonds in this figure are the locations of some of the PBRs present within 30 km of the San Andreas Fault (red contour regions with high *PGA*). Under the assumption that these rocks have been present for 12,000 years, they should have experienced the *PGA* levels given by the NSHM at least four times during their lifetime. The high *PGA* levels at the PBR locations from the NSHM do not agree with Brune's preliminary quasi-static analysis [25], according to which most of these rocks would overturn for *PGAs* as low as 0.3 g. This inconsistency of the seismic hazard maps with the existence of the PBRs near major fault zones motivates the current research.

The aim of this research is to accurately estimate the earthquake ground motion required to overturn the PBRs and to use it as an independent test of the probabilistic seismic hazard maps and synthetic ground motions simulations. The results from this analysis will also

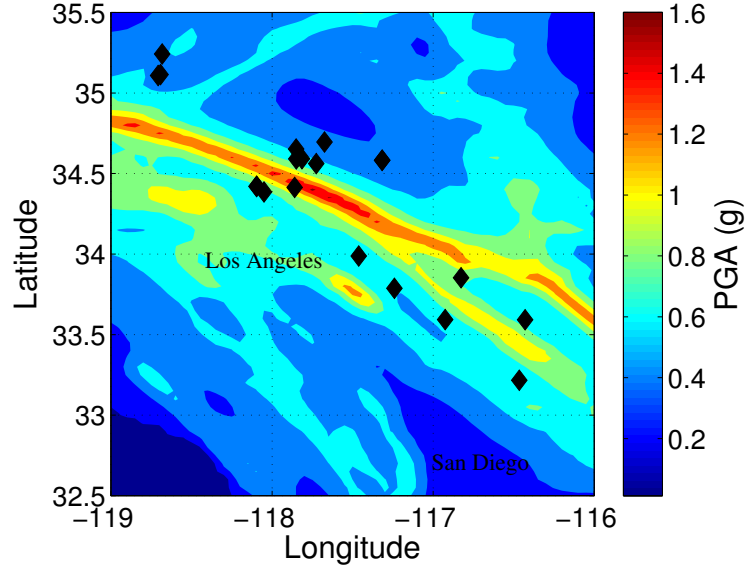


Figure 1.2: 2014 National Seismic Hazard map for 2% probability of exceedance in 50 years for *PGA*. The black diamonds show location of PBRs within 30 km of the San Andreas Fault.

assist in locating sensitive buildings like schools, hospitals, and power plants in areas of low seismic risk and also in adequately and economically designing the buildings located at high seismic risk locations, thereby reducing loss of life and property.

1.2 Precariously balanced rocks

Precariously balanced rocks are those rocks which are more likely to be overturned during earthquakes. Using the minimum constant ground horizontal acceleration, henceforth referred to as the quasi-static toppling acceleration a_g^s , required to overturn them, Brune [25] has classified them as precarious ($0.1 g \leq a_g^s \leq 0.3 g$) or semi-precarious ($0.3 g < a_g^s \leq 0.5 g$). a_g^s may be estimated by in-situ tilt tests in which the force required at the center of mass of the rock to tilt it until it just overturns is measured [9]. A rough estimate of a_g^s may also be obtained from images of the rock [90].

Brune and his family conducted road surveys near major fault zones and cataloged hundreds of PBRs in Southern California and Nevada. Apart from the set of PBRs near the San Andreas Fault shown in Fig. 1.2, they found a band of PBRs located between the San Jacinto and Elsinore fault zones in Southern California [26] and near Yucca mountain in

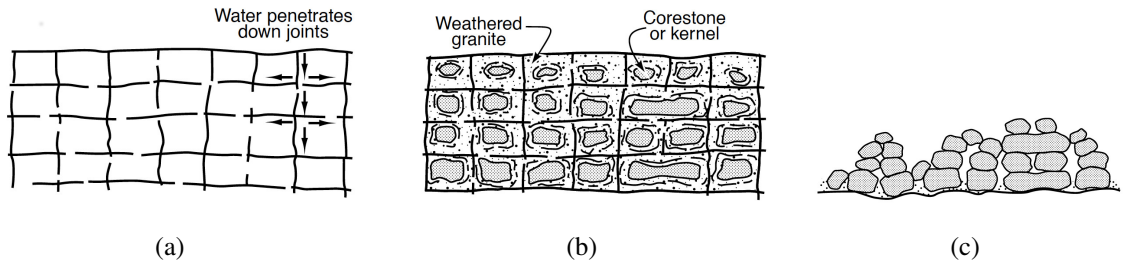


Figure 1.3: Formation of type II PBRs. (a) Water infiltrates through the fractured rock and weathers it into corestones as in (b) which are then exhumed due to erosion to obtain the PBRs in (c) [15].

Nevada [89], which was one of the nuclear waste repositories. The presence of these rocks near major fault zones amplifies the importance of this methodology.

1.2.1 Formation and age

There are two predominant geological processes that result in PBRs [91]. Type I rocks, commonly referred to as hoodoos, are formed when a softer rock lies beneath a relatively weather resistant rock. The difference in their weathering rates results in a bulbous rock sitting on a narrow base. Type II PBRs are formed due to water trickling into a fractured, buried rock mass. The regions of the rock near the fractures are weathered due to the water flow. The unweathered parts of the rock tend to form stacks of boulders as the rock mass is exhumed and the weathered materials are washed away due to erosion [72]. This process is illustrated in Fig. 1.3. Both types of PBRs are present on bedrock, and therefore ground motion amplification and soil-structure interaction do not significantly alter the ground motions experienced by the PBR.

Due to the differences in the formation processes, type I rocks are mostly present in sedimentary environments as opposed to type II rocks which are located in igneous and volcanic environments. In this dissertation, we will be analyzing type II rocks as these types of rocks are more likely to maintain their precarious configuration for longer periods of time than the type I rocks due to their slow weathering rate after surface exposure [18, 103]. The formation process of type II PBRs also guarantees that the PBR and its pedestal are disjoint structures which makes computation of the critical toppling intensity easier.

Bell et al. [15] used varnish microlamination (VML) method to study PBRs in Southern

California. They found that most of the PBRs have been exposed for more than 10,500 radiocarbon years, i.e., approximately 12,000 years, without significant alteration. The VML method uses the rock varnish to estimate the age of the rock. The rock varnish is a dark coating on the rock which increases at a rate of few micrometers per millennium. The chemical composition of this varnish is distinctly different from the rock underneath and is made up of ingredients delivered from the atmosphere by precipitation, aerosols, dust, and dew [40]. The rock varnish is formed and preserved well in semiarid deserts like Southern California and Nevada. Therefore, an accurate estimate of the age of the rock and information about any non-uniform erosion of the rock surface can be obtained by measuring the thickness of the varnish layer and examining its chemical composition at different points on the rock and the pedestal. More details about this method and its accuracy can be found in [73].

1.2.2 Friction coefficient

Friction between rocks is of interest to three different fields: civil engineering, mining engineering, and geophysics. In civil engineering applications like analyzing the stability of a dam or a road cut, the normal stresses on the rocks are usually less than 5 MPa. Mining engineers are interested in designing mine opening at depths as great as 3 km and the rocks at this depth will experience normal stresses around 100MPa. Geophysicists are concerned with earthquakes that occur as deep as 700 km below the earth's surface. Though it is difficult to realize the stresses corresponding to this depth in an experimental setup, the experiments in which the normal stresses on the rock are above 1.5GPa are considered reasonably accurate for geophysics applications.

In a typical friction experiment, a rectangular block is free to slide on a rigid flat surface and the horizontal force required to move the block is applied through a spring. The force vs displacement curve for the block obtained from the experiment is then used to calculate the coefficient of friction, i.e., the ratio of shear to normal stress. Byerlee [27] analyzed the experimental data obtained from various sources for different rock materials by dividing them into the three regimes described above based on their normal stresses. Byerlee found

that the coefficient of friction is independent of the rock type/material in all regimes. For intermediate normal stresses, all the data points suggest that the friction coefficient is 0.85. For high and low levels of normal stresses, the friction coefficient is between 0.6 – 0.85 and 0.6 – 1.0, respectively.

In the case of a PBR balanced on a pedestal, the normal stresses are similar to that encountered in a civil engineering application. Therefore, the coefficient of friction between the rock and the pedestal is between 0.6 and 1.0.

1.2.3 Past analysis

A good starting point for any discussion about the analysis of PBRs is the analysis of a simple 2-D rectangular block. The idea of inferring ground motion characteristics from overturned objects was first attempted by Mallet [80]. Using Dr. C. D. West's formula, Mallet estimated the minimum peak ground acceleration (*PGA*) required to overturn a rectangular block as a product of the acceleration due to gravity with the aspect ratio of the block, i.e., ratio of width to height. This estimate was later tested experimentally through the use of 39 rectangular blocks of varying dimensions overturned on a harmonically forced table [82]. The minimum overturning *PGA* from experiments did not match with those calculated by Mallet in most cases.

Kirkpatrick [66] demonstrated experimentally that the *PGA* estimated by Mallet is the minimum acceleration required to initiate rocking as opposed to overturn the block. In addition, Kirkpatrick analyzed the linearized equation of motion for the rocking response of the block under harmonic excitation and found that the block will overturn at the *PGA* estimated by Mallet under excitations with long time period. He also verified that his analytical solution matches well with experimental results. The linearized response of the rectangular block under harmonic excitation was re-derived by Ikegami and Kishinouye [56, 57] and they obtained an overturning criteria based on work arguments. They also applied these results to explain the overturning of tombstones during the 1946 Nankai and 1949 Imaichi earthquakes. These authors demonstrate the scale effect of how intense ground motions may topple slender but smaller objects, yet not be able to topple larger objects with the

same slenderness.

All the analytical formulation described earlier assume perfectly inelastic impacts between the block and the ground. However, Kimura and Iida [64,65] were the first to account for dynamic energy balance. This analysis revealed that momentum is not conserved before and after each basal impact in the earlier formulations. They enforced conservation of momentum by reducing angular velocity immediately after impact by a ratio r which depends only on the block geometrical parameters. Housner [52] independently derived the expression for the velocity reduction r applied at impact 30 years after the work by Kimura and Iida.

Most of the analysis on the toppling intensity of rectangular blocks and rocks are based on Housner's work. He derived an approximate overturning criteria when the rectangular block is subjected to simple excitations like constant acceleration, sinusoidal pulse, and random excitations. The results obtained by Housner [52] suggest that the block width required for stability does not scale linearly with the block height, which seconds the scale effect demonstrated by Ikegami and Kishinouye [56,57]. Housner also used these results to analyze the damage resulting from the 1960 Chilean earthquake.

This seemingly simple problem of a 2-D rigid rectangular block sitting on a horizontally shaken rigid ground has since then attracted the attention of many researchers. The response of a rectangular block under half-sine pulse and full sine pulse excitations were further analyzed by Shi et al. [96], Anooshehpour et al. [10], and Zhang and Makris [115], and the linear dependence of the critical overturning PGA on the frequency of excitation was noted. Sensitivity of the equation of motion to initial conditions and system parameters were analyzed numerically and results indicated that very small variations in excitation frequency, phase, or amplitude of excitation can result in exponentially diverging responses [11, 12, 24, 48–50, 70, 71, 87, 99, 102, 110–112, 114]. Large velocity reductions applied at impact were shown to reduce to the sensitivity of the numerical block to small variations in initial conditions [70, 112].

The equation of motion for the rocking response of the rectangular block changes depending on the point about which the block rocks. This discontinuous nature of the equation of motion, the external velocity reduction applied at impact, and the nonlinear terms in the

equation of motion make it difficult to obtain an analytical or closed form solution for the critical overturning PGA when the block is subject to earthquake ground motions. In order to generalize observations, several researchers [7, 12, 111] numerically analyzed ensembles of rectangular blocks subjected to ensembles of earthquake ground motions or synthetic earthquake-like waveforms. These researchers found that the overturning probability of the block increased with increase in excitation amplitude and block slenderness and decrease in block width. They also found that vertical ground motion and small variations in the velocity reduction r applied at impact did not systematically affect the overturning probability in their numerical simulations. Kaneko and Hayashi [63] used ensembles of synthetic waveforms matching a target spectrum and found that the overturning probability can be described as a function of PGA and peak ground velocity (PGV).

All the above analysis is focused mainly on the rocking response of the rectangular block. Mochizuki and Kobayashi [83] explored the other possible modes of response, i.e., free-flight, sliding, and coupled sliding with rocking. Ishiyama [58, 59] derived the equations of motion for these modes and the conditions for transition from one mode to another. Shenton [95] obtained the the relationship between horizontal ground acceleration and coefficient of friction required to initiate response of the rectangular block under each of these modes. Many researchers have analyzed the sliding response of the rectangular block subjected to earthquake ground motions both analytically and numerically [41, 94, 100, 105].

The above analyses on a simple 2-D rectangular block has helped in understanding the complex physics behind the problem. There has been limited research on the response of the 3-D rectangular block to earthquake excitation [30, 31]. Some researchers have tried to apply these results to the analysis of PBRs. Coombs et al. [32] was probably the first to investigate the stability of a balanced rock. They estimated the minimum PGA required to overturn the Omak rock [Fig. 1.1(b)] using the same expression as Mallet [80]. They used this acceleration to place constraints on the ground motions experienced at that location during the 1872 Pacific Northwest earthquake. They also inferred a possible epicentral location for the earthquake from this analysis. Weichert [108] updated this analysis through numerical simulations of an equivalent 2-D rectangular block model of the rock.

More recently Purvance et al. [88,91] applied the rigid body rocking dynamics framework to the PBR problem. Following the Yim et al. [111] approach, they numerically simulated the rocking and overturning response of symmetric and asymmetric blocks under synthetically generated random vibration excitations. They used the results from this analysis to develop an empirical expression for estimating the overturning probability of a block as a function of its geometric parameters and various ground motion intensity measures such as peak ground acceleration (PGA), the ratio of peak ground velocity (PGV) to PGA (PGV/PGA), spectral acceleration at 1 s (S_a^{1s}) and 2 s (S_a^{2s}). Their choice of ground motion intensity measures was based on the strong correlation of PGV/PGA with duration of predominant acceleration pulse [88] and the correlation of S_a^{1s} and S_a^{2s} with PGV [85]. They compared the overturning fragility obtained from this empirical relation with results of shake table experiments on blocks and rocks of various sizes and shapes subjected to earthquake ground motion. The empirical relation was able to predict the PGA required to overturn blocks quite well but over-predicted the PGA required to overturn rocks.

The empirical equation, developed for 2-D rectangular blocks with two-point contact, does not account for the 3-D form of the rock or the curved form of basal contact (with multiple contact points) and predicts greater stability for the rock than what is observed in the experiments. To correct for the multiple contact points, Purvance et al. [88] conducted tilt tests on the rocks and adjusted the location of the two sharp contact points in the 2-D block model based on the ratio of the quasi-static toppling acceleration a_g^s to the acceleration due to gravity. They validated this methodology by comparing the results from the empirical relation with experiments on three rocks.

These results are a great starting point to understanding the dynamics of PBRs, but the idealizations and assumptions inherent in these analyses could have a significant impact on their critical toppling intensity. The empirical expression derived by Purvance et al. [91] assumes the response of the object to be restricted to the plane of applied excitation. While this is true for a rectangular block under uni-axial ground excitation, for most rocks this may not be true owing to their 3-D geometry and complex rock-pedestal interface. Moreover, non-destructive tilt tests need to be conducted to obtain realistic results from the empirical relation. But the inaccessible locations of most PBRs make it difficult to perform

tilt tests.

In order to overcome these issues, Purvance et al. [89] developed RIGID to analyze the response of 3-D PBR models to earthquake ground excitation using the discrete element method. They modeled the rock and pedestal as two separate rigid bodies and used the penalty stiffness method, which is analogous to a spring-damper assembly, to model the contact between the rock and the pedestal. Though they validated RIGID against shake table experiments on rectangular blocks, this methodology is not validated against experiments conducted on real rocks. The main limitation of this algorithm is that the stiffness and damping values of the spring-dashpot assembly needs to be calibrated carefully for each rock in order to obtain realistic (low-interpenetration) simulations while keeping computational costs manageable. Additionally, this algorithm is not capable of modeling the sliding and the coupled sliding-rocking response of the PBR. It is for these reasons that this algorithm has not been used lately for the analysis of PBRs and the current practice relies entirely on the empirical expression developed by Purvance et al. [88].

In this dissertation, we present an alternate method to analyze the response of 3-D PBR models to earthquake ground excitation under the assumption that the rock and the pedestal behave like rigid bodies. In the next section, the past work on rigid body dynamics, including the discrete element method adopted in RIGID, are discussed.

1.3 Rigid body dynamics

A rigid body is one which can only rotate and translate in space and cannot deform. All the information about the translational and rotational state of a rigid body at any instant in time can be condensed into four state variables. This is a major advantage of a rigid body dynamics formulation over a finite element formulation where the displacements of many nodes on the object need to be calculated and stored to obtain complete information about the object at any instant in time.

The time evolution of the state variables of a rigid body follow Newton's laws of physics. The main challenge in rigid body dynamics comes in modeling the interaction of one rigid body with another. This interaction is modeled using contact forces/impulses.

There two ways in which the contact can be modeled: penalty stiffness method (soft contact) and constraint based method (hard contact).

Discrete element methods are built on penalty stiffness method. Cundall [35] and Hart et al. [45] developed a three-dimensional distinct element methodology (which is a subset of discrete element method) and applied it to various rock mechanics and geomechanics applications. In this method, slight overlap of the rigid bodies are allowed. The contact forces are proportional to the overlapping area/volume between the two rigid bodies. Therefore, this method is analogous to using a spring-damper assembly to model the contact. Once the contact forces are estimated, they are applied at one “contact point”. Cundall [35] applied the contact forces at the midpoint of the line joining the centroids of the rigid bodies in contact. The algorithms RIGID developed by Purvance et al. [89] and 3DEC [44] are based Cundall’s algorithm with some variations in contact detection techniques.

To estimate the contact forces accurately, the contact stiffness and damping values must be chosen carefully. A low contact stiffness would result in high overlap between the rock and the pedestal yielding unrealistic results. On the other hand, for a high contact stiffness the simulation time step has to be very small to overcome numerical instabilities, which results in high computational cost. In the absence of experimental data regarding the contact stiffness between a PBR and its pedestal, Purvance et al. [89] calibrated the contact stiffness parameters such that the numerical simulation of rectangular blocks using RIGID match the shake table experimental results. The same parameters are then used for simulating PBRs without validating the results with shake table experiments on rocks. The uncertainties in the contact stiffness parameters and the high computational cost make this method unsuitable for analyzing 3-D PBR models.

On the other hand, overlap between rigid bodies is not tolerated in constraint based methods (hard contact). Therefore, contact forces/impulses are calculated to satisfy these non-penetration constraints. There are two ways to achieve this : (i) using impulses alone and (ii) using impulses as well as contact forces. In the first approach [16,17,109], impulses are applied at points where two rigid bodies collide. These impulses are calculated such that the rigid bodies are either touching each other (relative normal velocity is zero) or moving away from each other (relative normal velocity is positive) at the contact points

after the collision. In between collisions, each rigid body is assumed to be under free flight, i.e., the presence of other rigid bodies are not acknowledged. This method is useful for the dynamic simulation of cluttered environments where rigid bodies collide often. However, it is not efficient for simulating scenarios with sustained contact like books stacked on a book-shelf.

In the second approach, impulses are applied to satisfy velocity constraints (similar to the first approach), and if the contact persists, then contact forces are applied to prevent rigid bodies from accelerating towards each other at the contact points. This approach addresses the issue of rigid bodies in sustained contact but is not efficient in simulating large number of rigid bodies colliding with each other due to the additional expense of computing contact forces. Lötstedt [75] was the first to handle contacts in this way. Baraff [13] presented a fast algorithm based on Cottle and Dantzig’s algorithm [33] to compute the contact forces and impulses efficiently.

Each of the methods described above are crafted for problems of a specific type. The focus of this thesis is on simulating response of precariously balanced rocks to ground excitation. Here, the PBR is one rigid body and the pedestal is another rigid body. Initially, the PBR is sitting on the pedestal and the contact between them is maintained for varying periods of time depending on the acceleration imparted to the pedestal. Therefore, the constraint based method using both impulses as well as contact forces is the best way to approach this problem. The problem set up is similar to the one formulated by Baraff [13].

1.4 Outline

The main focus of this dissertation is to provide an independent constraint on historic peak ground motion experienced at a region using precariously balanced rocks. From past literature on analysis of rectangular blocks and PBRs, it can be seen that constraint based rigid body dynamics algorithm using both impulses and contact forces is the best way to analyze the response of a 3-D PBR model to earthquake excitation.

In Chapter 2, limitations of Baraff’s algorithm [13] are discussed following which details of the rigid body dynamics algorithm developed for this special problem are presented.

The algorithm is validated against analytical results for simple geometries like rectangular blocks.

In Chapter 3, the methodology to create and analyze 3-D PBR models subjected to earthquake excitation is presented. The accuracy of the rigid body dynamics algorithm in analyzing complex 3-D PBR models is verified by comparing the results against shake table experiments on a rock. Two PBR models are then created and analyzed under earthquake ground motion for different coefficients of friction and direction of earthquake excitation. The fragility maps obtained from this analysis are then used to perform simple checks on USGS national seismic hazard maps and synthetic ground motion simulations at the location of PBRs.

In Chapter 4, a different application of the rigid body dynamics algorithm is presented wherein quantitative estimates on the ground motion experienced at a region during an earthquake are obtained from qualitative information about the sliding/rocking response of man-made objects like battery-rack, train, and nuclear storage canister.

Chapter 5 concludes the dissertation with comments on possible lines of future research.

Chapter 2

Rigid body dynamics algorithm

In the previous chapter, we concluded that constraint based rigid body dynamics algorithm using both impulses and contact forces is the method that is best suited to analyze the response of 3-D PBR (precariously balanced rock) models to earthquake excitation. In this method, each rigid body is considered as a separate entity and the interaction between the rigid bodies are modeled using impulses and contact forces. These impulses and contact forces are calculated based on velocity and acceleration constraints. Lötstedt [75] was the first to handle contacts in this way. Baraff [13] presented a fast algorithm based on Cottle and Dantzig's algorithm [33] to compute the contact forces and impulses efficiently.

Contact forces play an important role in determining the total acceleration of a rigid body at any instant in time. In Baraff's algorithm, the problem of computing contact forces (normal and frictional contact forces) is posed as an optimization problem. Due to the ill-constrained nature of the optimization problem, it can result in infinite solutions for the contact forces. In certain cases (e.g., friction-less systems), all the contact force solutions lead to the same total acceleration of the rigid body. However, in the presence of static friction forces satisfying Coulomb friction law, all the solutions may not result in the same total acceleration.

For example, let us consider the case where a rigid square cuboid of mass $m = 100$ kg with half width $w = 0.1$ m, half height $h = 0.6$ m, and half depth $d = 0.1$ m is resting on a rigid horizontal ground [Fig. 2.1(a)]. Say the cuboid comes in contact with the ground at only the four corners (O_1 , O_2 , O_3 , and O_4). If gravity g is the only external acceleration on the cuboid, the normal contact forces at all corners can be equal (i.e., $mg/4$) or the

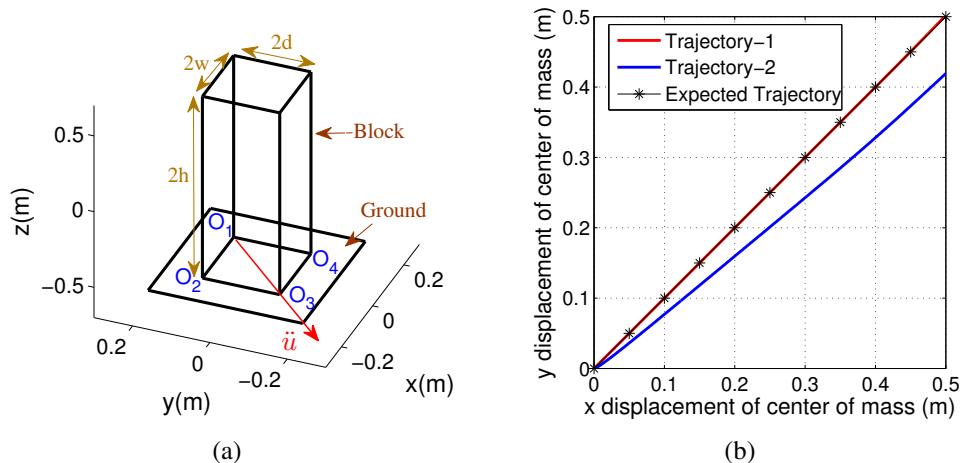


Figure 2.1: (a) Rigid cuboid sitting on rigid ground accelerating with horizontal acceleration \ddot{u} ; (b) Expected horizontal trajectory of the center of mass of the block and two trajectories obtained from implementation of Baraff’s algorithm. Trajectory-1, which matches with the expected trajectory, is obtained when contact force calculation starts with point O_1 , and trajectory-2 is obtained when the contact force calculation starts with point O_2 .

forces at opposite corners can be equal, (i.e., $O_1 = O_3$, $O_2 = O_4$) such that O_1 and O_2 are positive real numbers satisfying $O_1 + O_2 = mg/2$. So, there are infinite combinations of forces that result in zero total translational and rotational acceleration of the cuboid, i.e., the cuboid will remain at rest. In addition to gravity, if the ground constantly accelerates along the diagonal direction opposite to O_1 with a magnitude \ddot{u} , which is greater than the quasi-static toppling acceleration of the cuboid (i.e., the minimum constant ground acceleration required for the cuboid to overturn), then it is expected that the block will rotate about the corner O_1 and overturn. For a static friction coefficient $\mu = 1.2$, which is sufficiently high enough to prevent sliding between the cuboid and the ground, Baraff’s algorithm results in two possible dynamic paths for the cuboid [Fig. 2.1(b)]. For clarity, only the plan (x-y plane) projection of the displacement of the center of mass relative to the ground is presented. The line with asterisk markers is the expected trajectory which is the $x = y$ line due to the symmetry in the geometry of the cuboid and the applied ground acceleration.

Baraff’s algorithm is an iterative procedure in which the forces at the contact points are handled sequentially. Say the algorithm starts at corner O_1 , the normal contact force for point O_1 is calculated such that the normal contact constraints are satisfied for this contact point. Then, the friction force in X-direction is calculated followed by the friction

force in Y-direction such that the friction constraints are satisfied. During the calculation of the friction forces, the normal force is altered so that the normal contact constraints continue to hold. This is repeated for the next contact point O_2 , making sure the normal and frictional constraints for point O_1 are still satisfied. The algorithm terminates when the normal and friction constraints are satisfied at all contact points. This can happen after calculating forces for just corner O_1 or corners O_1 and O_2 etc. Due to the sequential treatment of the contact points, this algorithm leads to different solutions based on the order in which the contact points are considered or the order in which the friction forces are calculated (X direction followed by Y direction). For the above example, if the algorithm starts with contact point O_1 , then it results in trajectory-1, but if O_2 is considered first, then it leads to trajectory-2 [Fig. 2.1(b)]. Both solutions are mathematically correct solutions to the optimization problem. However, the deviation of trajectory-2 from the expected trajectory, caused by artificial twisting of the block about the vertical axis, violates the inherent symmetry of the problem.

Baraff’s algorithm is aimed at obtaining fast simulations for computer graphics and robotics applications for which this iterative algorithm works well. It is the de-facto standard algorithm used in simulation software packages such as Maya and Open dynamics engine [97]. Past works on this topic have focused solely on solving the optimization problem without due regard to solution selection consistent with the physics of the problem (from the infinite set of solutions).

In this chapter, an alternate method to solve the optimization problem formulated by Lötstedt and Baraff is presented. The main idea behind this algorithm is that at each dynamic time step the rigid body will choose the contact force solution that is closest to the equilibrium state of the rigid body at the previous time step. This will always lead to the symmetric solution [e.g., trajectory-1 in Fig. 2.1(b)] if one is present.

2.1 Algorithm

Consider a rigid body rotating and translating in space. Let $\mathbf{u}_{\text{cm}}(t)$ and $\dot{\mathbf{u}}_{\text{cm}}(t)$ be the position vector and the translational velocity vector, respectively, of the center of mass

(*cm*) in the global coordinate system, $\mathbf{R}(t)$ be the rotation matrix between the local and global coordinate systems, which are initially co-located at the *cm*, and $\mathbf{I}(t)$ be the angular momentum of the rigid body about the *cm* in global coordinate system, all at time t . These four quantities are the state variables as they provide complete information about the rigid body at any instant in time. In this chapter, bold lowercase letters are vectors and bold uppercase letters are matrices. All vectors and matrices are in the global coordinate system unless noted otherwise. The rate of change of these state variables with respect to time are given by:

$$\frac{d}{dt} \mathbf{u}_{\text{cm}}(t) = \dot{\mathbf{u}}_{\text{cm}}(t) \quad (2.1)$$

$$\frac{d}{dt} \dot{\mathbf{u}}_{\text{cm}}(t) = \frac{\mathbf{f}_{\mathbf{T}}(t)}{m} \quad (2.2)$$

$$\frac{d}{dt} \mathbf{R}(t) = \boldsymbol{\omega}(t) \times \mathbf{R}(t) \quad (2.3)$$

$$\frac{d}{dt} \mathbf{l}(t) = \boldsymbol{\tau}_{\mathbf{T}}(t) \quad (2.4)$$

Here, $\boldsymbol{\omega}(t)$ is the angular velocity [$\boldsymbol{\omega}(t) = \mathbf{I}^{-1}(t)\mathbf{l}(t)$], $\mathbf{I}(t)$ is the moment of inertia, $\mathbf{f}_{\mathbf{T}}(t)$ is the net force, $\boldsymbol{\tau}_{\mathbf{T}}(t)$ is the net torque about *cm*, and m is the mass of the rigid body. The moment of inertia at time t , $\mathbf{I}(t)$, can be calculated if its value at $t = 0$ is known [$\mathbf{I}(t) = \mathbf{R}^T(t)\mathbf{I}(0)\mathbf{R}(t)$].

The discussion above is for a general rigid body. We are interested in modeling the interaction between a rock and its pedestal, a rigid body which does not rotate. The rock and the pedestal are modeled separately with four state variables each. Let $\mathbf{u}_{\text{cm}}(t)$, $\dot{\mathbf{u}}_{\text{cm}}(t)$, $\mathbf{R}(t)$, and $\mathbf{I}(t)$ be the state variables for the rock and $\mathbf{u}_{\text{p}}(t)$, $\dot{\mathbf{u}}_{\text{p}}(t)$, $\mathbf{R}_{\text{p}}(t)$, and $\mathbf{l}_{\text{p}}(t)$ be the state variables for the pedestal. Since the pedestal can only translate, the rotation matrix of the pedestal, $\mathbf{R}_{\text{p}}(t)$, is always the identity matrix and angular momentum of the pedestal, $\mathbf{l}_{\text{p}}(t)$, is always zero.

The aim of the algorithm is to obtain the state variables for the rock and pedestal at time $t + \Delta t$ given the state of the system at time t . Since the pedestal has an infinite mass and moment of inertia, the contact forces and impulses resulting from the interaction of the pedestal with the rock have no effect on the dynamics of the pedestal. Let $\ddot{\mathbf{u}}_{\text{p}}(t)$ be

the applied pedestal acceleration as a function of time. Then, pedestal displacement and velocity at $t + \Delta t$ may be determined by time-integrating Eqs. 2.1 and 2.2 using the constant average acceleration method:

$$\mathbf{u}_p(t + \Delta t) = \mathbf{u}_p(t) + \frac{\Delta t}{2} [\dot{\mathbf{u}}_p(t) + \dot{\mathbf{u}}_p(t + \Delta t)] \quad (2.5)$$

$$\dot{\mathbf{u}}_p(t + \Delta t) = \dot{\mathbf{u}}_p(t) + \frac{\Delta t}{2} [\ddot{\mathbf{u}}_p(t) + \ddot{\mathbf{u}}_p(t + \Delta t)] \quad (2.6)$$

However, obtaining the state variables for the rock at $t + \Delta t$ is not as simple. The state variables have to be estimated iteratively so that the rock is in dynamic equilibrium at $t + \Delta t$. The outline of the algorithm is shown in Algorithm 1.

Algorithm 1 Rigid body dynamics algorithm

Input: rock state variables at t , pedestal state variables at t and $t + \Delta t$

Output: rock state variables at $t + \Delta t$

```

1: initialization
2: while rock state variables at  $t + \Delta t$  not converged do
3:   update state variables at  $t + \Delta t$  using Eqs. 2.7 - 2.10 // Step 1
4:   if rock penetrates the pedestal then // Step 2
5:     reduce  $\Delta t$ 
6:     go back to initialization
7:   end if
8:   if rock and pedestal in contact then
9:     estimate impulses to resolve collision // Step 3
10:    while normal impulses not converged do
11:      update normal impulses // Step 3(a)
12:      update frictional impulses // Step 3(b)
13:    end while
14:    estimate contact forces // Step 4
15:    while normal forces not converged do
16:      update normal forces // Step 4(a)
17:      update frictional forces // Step 4(b)
18:    end while
19:  else
20:    no contact forces
21:  end if
22: end while

```

The following are the steps to go from time-step iteration k to iteration $k + 1$ (outermost

while loop) for the state variables of the rock.

Step 1: Integrate differential equations.

To estimate the state variables of the rock at $t + \Delta t$, the differential Eqs. 2.1 - 2.4 for the rock are time integrated using constant average acceleration method to yield:

$$\mathbf{u}_{\text{cm}}^{k+1}(t + \Delta t) = \mathbf{u}_{\text{cm}}(t) + \frac{\Delta t}{2} [\dot{\mathbf{u}}_{\text{cm}}(t) + \dot{\mathbf{u}}_{\text{cm}}^k(t + \Delta t)] \quad (2.7)$$

$$\dot{\mathbf{u}}_{\text{cm}}^{k+1}(t + \Delta t) = \dot{\mathbf{u}}_{\text{cm}}(t) + \frac{\Delta t}{2} \left[\frac{\mathbf{f}_{\mathbf{T}}(t)}{m} + \frac{\mathbf{f}_{\mathbf{T}}^k(t + \Delta t)}{m} \right] \quad (2.8)$$

$$\mathbf{R}^{k+1}(t + \Delta t) = \mathbf{R}(t) + \frac{\Delta t}{2} [\boldsymbol{\omega}(t) \times \mathbf{R}(t) + \boldsymbol{\omega}^k(t + \Delta t) \times \mathbf{R}^k(t + \Delta t)] \quad (2.9)$$

$$\mathbf{l}^{k+1}(t + \Delta t) = \mathbf{l}(t) + \frac{\Delta t}{2} [\boldsymbol{\tau}_{\mathbf{T}}(t) + \boldsymbol{\tau}_{\mathbf{T}}^k(t + \Delta t)] \quad (2.10)$$

$\mathbf{R}^{k+1}(t + \Delta t)$ is a rotation matrix, so its determinant should be unity and its inverse should equal its transpose. If these properties are not satisfied by $\mathbf{R}^{k+1}(t + \Delta t)$, Cayley transform [29] is used to project the matrix back onto the admissible space of rotation matrices. If the rock is initially at rest on the pedestal, then $\mathbf{u}_{\text{cm}}(0) = \mathbf{0}$, $\dot{\mathbf{u}}_{\text{cm}}(0) = \mathbf{0}$, $\mathbf{R}(0) = \mathbf{I}$, the identity matrix, $\mathbf{l}(0) = \mathbf{0}$, $\mathbf{f}_{\mathbf{T}}(0) = \mathbf{0}$, $\boldsymbol{\tau}_{\mathbf{T}}(0) = \mathbf{0}$, and $\boldsymbol{\omega}(0) = \mathbf{0}$.

Step 2: Find contact points.

Using the state variables obtained in **Step 1**, the positions of the points on the outer surface of the rock are updated. For example, if α is a point on the rock and $\mathbf{r}_{\alpha}(0)$ is its initial position with respect to the cm , then its updated position vector is:

$$\mathbf{u}_{\alpha}^{k+1}(t + \Delta t) = \mathbf{u}_{\text{cm}}^{k+1}(t + \Delta t) + \mathbf{R}^{k+1}(t + \Delta t) \mathbf{r}_{\alpha}(0) \quad (2.11)$$

Similarly, the positions of points on the pedestal surface are updated. At $t + \Delta t$, if any point of the rock is within ϵ (tolerance) from the surface of the pedestal, then that point is assumed to be a contact point. However, if any point on the rock's surface penetrates a distance more than ϵ into the pedestal, then the system is taken back to an earlier time t_c ($t \leq t_c \leq t + \Delta t$) when no point has penetrated more than ϵ into the surface of the pedestal and the calculations are carried out for the reduced time step.

With no point on the rock's surface penetrating into the pedestal, we look for rock

points that are in contact with the pedestal. If none exist, it implies that the rock is in free-fall under the action of gravity and the contact forces are set to zero. Net force acting on the rock is $\mathbf{f}_T^{k+1}(t + \Delta t) = m\mathbf{g}$, where \mathbf{g} is the acceleration due to gravity, and net torque acting on the rock is $\boldsymbol{\tau}_T^{k+1}(t + \Delta t) = \mathbf{0}$. Since the total force and total torque acting on the rock are known now, we proceed to **Step 5** of the algorithm.

If, on the other hand, at least one point of the rock is in contact with the ground, then we go through **Steps 3** and **4** to prevent the rock from penetrating into the pedestal at this contact point. We start by attaching a coordinate system local to each contact point. The outward normal (\mathbf{n}_α) to the pedestal at contact point α is known from the surface of the pedestal. The unit vectors \mathbf{x}_α and \mathbf{y}_α in the tangential directions to the pedestal surface are obtained by:

$$\mathbf{x}_\alpha = \frac{\hat{\mathbf{x}} - (\hat{\mathbf{x}} \cdot \mathbf{n}_\alpha)\mathbf{n}_\alpha}{\|\hat{\mathbf{x}} - (\hat{\mathbf{x}} \cdot \mathbf{n}_\alpha)\mathbf{n}_\alpha\|_2}; \quad \mathbf{y}_\alpha = \frac{\mathbf{n}_\alpha \times \mathbf{x}_\alpha}{\|\mathbf{n}_\alpha \times \mathbf{x}_\alpha\|_2} \quad (2.12)$$

Here, $\hat{\mathbf{x}} = \{1, 0, 0\}$, the unit vector in the global X direction. For the above example of a rigid cuboid sitting on horizontal ground, $\mathbf{n}_\alpha = \{0, 0, 1\}$, $\mathbf{x}_\alpha = \{1, 0, 0\}$, and $\mathbf{y}_\alpha = \{0, 1, 0\}$ at all contact points.

Step 3: Resolve collisions by applying impulses.

The aim of this step is to ensure that the rock is not moving towards the pedestal at any of the contact points. If contact point α of the rock is moving towards the pedestal, then normal ($j_{n\alpha}\mathbf{n}_\alpha$) and frictional impulses ($j_{x\alpha}\mathbf{x}_\alpha$ and $j_{y\alpha}\mathbf{y}_\alpha$) are applied there in order to instantaneously change its velocity. Say there are q contact points. Let $\mathbf{j} = [\mathbf{j}_n \mathbf{j}_x \mathbf{j}_y]$, where $\mathbf{j}_n = [j_{n1} \ j_{n2} \ \dots \ j_{nq}]$ etc., be the row vector of length $1 \times 3q$ containing the magnitudes of impulses applied at all contact points with respect to their local coordinate systems. Similarly, let $\dot{\mathbf{u}}^- = [\dot{\mathbf{u}}_n^- \ \dot{\mathbf{u}}_x^- \ \dot{\mathbf{u}}_y^-]$ and $\dot{\mathbf{u}}^+ = [\dot{\mathbf{u}}_n^+ \ \dot{\mathbf{u}}_x^+ \ \dot{\mathbf{u}}_y^+]$, where $\dot{\mathbf{u}}_n^- = [\dot{u}_{n1}^- \ \dot{u}_{n2}^- \ \dots \ \dot{u}_{nq}^-]$ etc., be the row vectors of length $1 \times 3q$ containing relative velocities of the contact points on the rock with respect to the pedestal before and after collision, respectively.

Let $\dot{\mathbf{u}}_{\text{cm}}^- = \dot{\mathbf{u}}_{\text{cm}}^{k+1}(t + \Delta t)$ and $\boldsymbol{\omega}^- = \boldsymbol{\omega}^{k+1}(t + \Delta t)$ be the translational and angular velocity, respectively, of the rock before collision. Let $\dot{\mathbf{u}}_{\text{cm}}^+$ and $\boldsymbol{\omega}^+$ be the translational and angular velocity, respectively, of the rock after collision with the pedestal. To simplify

notation, let $\mathbf{r}_\beta = \mathbf{r}_\beta^{k+1}(t + \Delta t)$ be the position vector of contact point β with respect to the center of mass, and $\mathbf{I} = \mathbf{I}^{k+1}(t + \Delta t)$ be the moment of inertia of the rock about cm in the global coordinate system. The translational and angular velocity of the rock after collision may be obtained as follows:

$$\dot{\mathbf{u}}_{\text{cm}}^+ = \frac{1}{m} \sum_{\beta=1}^q j_{n\beta} \mathbf{n}_\beta + \frac{1}{m} \sum_{\beta=1}^q j_{x\beta} \mathbf{x}_\beta + \frac{1}{m} \sum_{\beta=1}^q j_{y\beta} \mathbf{y}_\beta + \dot{\mathbf{u}}_{\text{cm}}^- \quad (2.13)$$

$$\boldsymbol{\omega}^+ = \sum_{\beta=1}^q \mathbf{I}^{-1}(\mathbf{r}_\beta \times j_{n\beta} \mathbf{n}_\beta) + \sum_{\beta=1}^q \mathbf{I}^{-1}(\mathbf{r}_\beta \times j_{x\beta} \mathbf{x}_\beta) + \sum_{\beta=1}^q \mathbf{I}^{-1}(\mathbf{r}_\beta \times j_{y\beta} \mathbf{y}_\beta) + \boldsymbol{\omega}^- \quad (2.14)$$

The relative normal velocity of contact point α with respect to pedestal before and after collision are given by $\dot{u}_{n\alpha}^- = \mathbf{n}_\alpha \cdot [\dot{\mathbf{u}}_{\text{cm}}^- + \boldsymbol{\omega}^- \times \mathbf{r}_\alpha - \dot{\mathbf{u}}_p(t + \Delta t)]$ and $\dot{u}_{n\alpha}^+ = \mathbf{n}_\alpha \cdot [\dot{\mathbf{u}}_{\text{cm}}^+ + \boldsymbol{\omega}^+ \times \mathbf{r}_\alpha - \dot{\mathbf{u}}_p(t + \Delta t)]$, respectively. Similar expressions exist for the relative tangential velocities. Substituting for $\dot{\mathbf{u}}_{\text{cm}}^+$ and $\boldsymbol{\omega}^+$ from Eqs. 2.13 and 2.14 into these expressions for relative velocities after collision, the affine relation between relative velocities after collision and the impulses may be obtained as follows:

$$\dot{\mathbf{u}}^+ = \mathbf{j}\mathbf{C} + \mathbf{d}; \quad \mathbf{C} = \begin{bmatrix} \mathbf{C}_{nn} & \mathbf{C}_{nx} & \mathbf{C}_{ny} \\ \mathbf{C}_{xn} & \mathbf{C}_{xx} & \mathbf{C}_{xy} \\ \mathbf{C}_{yn} & \mathbf{C}_{yx} & \mathbf{C}_{yy} \end{bmatrix}_{3q \times 3q}; \quad \mathbf{d} = \begin{bmatrix} \mathbf{d}_n & \mathbf{d}_x & \mathbf{d}_y \end{bmatrix}_{1 \times 3q} \quad (2.15)$$

$$(C_{nn})_{\alpha\beta} = \frac{1}{m} \mathbf{n}_\alpha \cdot \mathbf{n}_\beta + (\mathbf{r}_\alpha \times \mathbf{n}_\alpha)^T \mathbf{I}^{-1}(\mathbf{r}_\beta \times \mathbf{n}_\beta); \quad \mathbf{d}_n = \dot{\mathbf{u}}_n^-$$

$$(C_{xx})_{\alpha\beta} = \frac{1}{m} \mathbf{x}_\alpha \cdot \mathbf{x}_\beta + (\mathbf{r}_\alpha \times \mathbf{x}_\alpha)^T \mathbf{I}^{-1}(\mathbf{r}_\beta \times \mathbf{x}_\beta); \quad \mathbf{d}_x = \dot{\mathbf{u}}_x^-$$

$$(C_{yy})_{\alpha\beta} = \frac{1}{m} \mathbf{y}_\alpha \cdot \mathbf{y}_\beta + (\mathbf{r}_\alpha \times \mathbf{y}_\alpha)^T \mathbf{I}^{-1}(\mathbf{r}_\beta \times \mathbf{y}_\beta); \quad \mathbf{d}_y = \dot{\mathbf{u}}_y^-$$

$$(C_{nx})_{\alpha\beta} = (C_{xn})_{\beta\alpha} = \frac{1}{m} \mathbf{n}_\alpha \cdot \mathbf{x}_\beta + (\mathbf{r}_\alpha \times \mathbf{n}_\alpha)^T \mathbf{I}^{-1}(\mathbf{r}_\beta \times \mathbf{x}_\beta); \quad \alpha = 1, 2, \dots, q$$

$$(C_{ny})_{\alpha\beta} = (C_{yn})_{\beta\alpha} = \frac{1}{m} \mathbf{n}_\alpha \cdot \mathbf{y}_\beta + (\mathbf{r}_\alpha \times \mathbf{n}_\alpha)^T \mathbf{I}^{-1}(\mathbf{r}_\beta \times \mathbf{y}_\beta); \quad \beta = 1, 2, \dots, q$$

$$(C_{xy})_{\alpha\beta} = (C_{yx})_{\beta\alpha} = \frac{1}{m} \mathbf{x}_\alpha \cdot \mathbf{y}_\beta + (\mathbf{r}_\alpha \times \mathbf{x}_\alpha)^T \mathbf{I}^{-1}(\mathbf{r}_\beta \times \mathbf{y}_\beta);$$

There are a few constraints which the impulses (\mathbf{j}) and the relative velocities after collision

($\dot{\mathbf{u}}^+$) must satisfy. If a contact point α of the rock is moving towards the pedestal (i.e., $\dot{u}_{n\alpha}^- < 0$), the normal impulse at α should push the point away from the pedestal to avoid interpenetration, i.e., $j_{n\alpha} \geq 0$. Next, from Newton's law of restitution, if e is the coefficient of restitution, then $\dot{u}_{n\alpha}^+ = -e\dot{u}_{n\alpha}^-$. However, if the rock is moving towards the pedestal at multiple contact points, the effect of the impulses applied at other points also affect the velocity at α as shown by Eq. 2.15. Therefore, Newton's law of restitution is the lower bound to the velocity after collision, i.e., $\dot{u}_{n\alpha}^+ \geq -e\dot{u}_{n\alpha}^-$. Once $\dot{u}_{n\alpha}^+$ is above this lower bound, there is no longer a need for an impulse at that point, i.e., $j_{n\alpha} = 0$. This constraint can be expressed by the complementarity condition $j_{n\alpha}(\dot{u}_{n\alpha}^+ + e\dot{u}_{n\alpha}^-) = 0$.

Because the impulses are applied instantaneously, no tangible displacement results. Therefore, static Coulomb friction laws are imposed on the friction impulses. This implies that the friction impulses should lie within/on the friction cone, i.e., $\sqrt{j_{x\alpha}^2 + j_{y\alpha}^2} \leq \mu_s j_{n\alpha}$, where μ_s is the static coefficient of friction. Also, the friction impulses should oppose the tangential velocity. In the earlier work by Baraff, this condition is implemented local to each contact point, i.e., the friction impulses at each contact point opposes the corresponding tangential velocity ($\dot{u}_{x\alpha}j_{x\alpha} + \dot{u}_{y\alpha}j_{y\alpha} \leq 0$). However, as seen from Eq. 2.15, the tangential velocity at contact point α is influenced by the friction impulses at all contact points. Therefore, the friction impulses must collectively oppose the tangential velocity at all contact points and result in the least magnitude of tangential velocity at all contact points.

The problem described above can be solved in many ways. Baraff [13] tackles it sequentially one contact point at a time. As illustrated earlier, this leads to different solutions based on the ordering of the contact points. We resolve this problem by collectively solving for all contact points first the normal impulse forces, and then the friction impulse forces. Because these forces are coupled, we repeat this exercise several times in an iterative fashion until there is little change in the forces (to within a tolerance). The computations in impulse iteration $p + 1$ within time step iteration $k + 1$ are described next. To start the iteration, all impulses are initialized to zero.

Step 3(a): Calculating normal impulses.

Using the normal part of Eq. 2.15 and the vectorized form of normal impulse con-

straints, the normal impulse problem is recast as a minimization problem:

$$\left. \begin{aligned} \dot{\mathbf{u}}_n^+ &= \mathbf{j}_n^{p+1} \mathbf{C}_{nn} + \mathbf{j}_x^p \mathbf{C}_{xn} + \mathbf{j}_y^p \mathbf{C}_{yn} + \mathbf{d}_n \\ \mathbf{j}_n^{p+1} &\geq \mathbf{0}; \quad \dot{\mathbf{u}}_n^+ + e \dot{\mathbf{u}}_n^- \geq \mathbf{0} \\ \mathbf{j}_n^{p+1} (\dot{\mathbf{u}}_n^+ + e \dot{\mathbf{u}}_n^-)^T &= 0 \end{aligned} \right\} \Rightarrow \begin{aligned} &\text{minimize } \mathbf{j}_n^{p+1} (\mathbf{j}_n^{p+1} \mathbf{C}_{nn} + \mathbf{d}_n')^T \\ &\text{subject to } \mathbf{j}_n^{p+1} \geq \mathbf{0} \\ &\mathbf{j}_n^{p+1} \mathbf{C}_{nn} + \mathbf{d}_n' \geq \mathbf{0} \end{aligned} \quad (2.16)$$

Here, $\mathbf{d}_n' = \mathbf{j}_x^p \mathbf{C}_{xn} + \mathbf{j}_y^p \mathbf{C}_{yn} + (1+e)\mathbf{d}_n$. This quadratic programming (QP) problem with an objective function having an optimal value of zero is known as a Linear Complementarity Problem (LCP). Baraff [13] has shown that the matrix \mathbf{C} is positive semi-definite. This implies that sub-matrix \mathbf{C}_{nn} is also positive semi-definite. This LCP is feasible, i.e., there exists a \mathbf{j}_n^{p+1} satisfying all the inequality constraints in Eq. 2.16 (details in Appendix A). It is also known that this LCP is solvable for every \mathbf{d}_n' if \mathbf{C}_{nn} is positive semi-definite and the problem is feasible [34]. However, the positive semi-definiteness of the matrix also implies that the LCP/QP may have infinitely many solutions.

Here, we solve this LCP using the Sequential Quadratic Programming (SQP) algorithm [68] of the open source nonlinear optimization software NLOpt [61]. Starting from \mathbf{j}_n^p the optimal solution for \mathbf{j}_n^{p+1} is calculated iteratively based on the local gradient of the objective function (similar to a Newton-Raphson iteration). The resulting solution, therefore, is the solution that is closest to \mathbf{j}_n^p from the infinite set of solutions, i.e., $\|\mathbf{j}_n^{p+1} - \mathbf{j}_n^p\|_2$ is the minimum among all possible solutions to the LCP.

Step 3(b): Calculating friction impulses.

The friction part of Eq. 2.15 is:

$$\begin{bmatrix} \dot{\mathbf{u}}_x^+ & \dot{\mathbf{u}}_y^+ \end{bmatrix} = \begin{bmatrix} \mathbf{j}_x & \mathbf{j}_y \end{bmatrix}^{r+1} \begin{bmatrix} \mathbf{C}_{xx} & \mathbf{C}_{xy} \\ \mathbf{C}_{yx} & \mathbf{C}_{yy} \end{bmatrix} + \mathbf{j}_n^{p+1} \begin{bmatrix} \mathbf{C}_{nx} & \mathbf{C}_{ny} \end{bmatrix} + \begin{bmatrix} \mathbf{d}_x & \mathbf{d}_y \end{bmatrix} \quad (2.17)$$

This equation along with the friction impulse constraints constitute the friction impulse problem. As mentioned previously, there are two constraints on the friction impulses: first,

they should lie on/inside the friction cone, and second, they should collectively oppose the tangential velocity at all contact points. These constraints are considered one by one and the problem is solved iteratively. The computations involved in friction impulse iteration $r + 1$ within impulse iteration $p + 1$ are described next.

First, we define two sets to classify contact points in each friction impulse iteration: \mathbf{S}^r and $\bar{\mathbf{S}}^r$. $\bar{\mathbf{S}}^r$ contains contact points that lie on the surface of the friction cone whose friction forces are assumed to remain unchanged as long as the point belongs to this set. Set \mathbf{S}^r contains the remaining contact points. Let set $\mathbf{N} = \{1, 2, \dots, q\}$ represent the set of all contact points. At the start of the friction impulse iteration, set \mathbf{S}^0 contains all the contact points and set $\bar{\mathbf{S}}^0$ is empty, i.e., $\mathbf{S}^0 = \mathbf{N}$ and $\bar{\mathbf{S}}^0 = \emptyset$.

Step 3(b)(i): Satisfying the “friction impulses oppose tangential velocity” constraint.

In this step, the friction impulses ($j_{x\alpha}^{r+1}$ and $j_{y\alpha}^{r+1}$) for all contact points $\alpha \in \mathbf{S}^r$ are calculated such that the relative tangential velocities of contact points in this set are reduced to zero. As per the definition of set $\bar{\mathbf{S}}^r$, the friction impulses of all contact points $\alpha \in \bar{\mathbf{S}}^r$ are left unchanged, i.e., $j_{x\alpha}^{r+1} = j_{x\alpha}^r$ and $j_{y\alpha}^{r+1} = j_{y\alpha}^r$. For ease of notation, let $\mathbf{j}_{\mathbf{x},\mathbf{S}^r}^{r+1}$ be the vector of frictional impulses in x direction for all contact points in \mathbf{S}^r , and $\mathbf{C}_{\mathbf{xx},\mathbf{SS}}$ be the sub-matrix of $\mathbf{C}_{\mathbf{xx}}$ corresponding to the contact points in \mathbf{S}^r , and so on. Also let, $\mathbf{j}_{\mathbf{x},\mathbf{S}^r}^{r+1} = \mathbf{j}_{\mathbf{x},\mathbf{S}^r}^r + \Delta\mathbf{j}_{\mathbf{x},\mathbf{S}}$ and $\mathbf{j}_{\mathbf{y},\mathbf{S}^r}^{r+1} = \mathbf{j}_{\mathbf{y},\mathbf{S}^r}^r + \Delta\mathbf{j}_{\mathbf{y},\mathbf{S}}$. Using this relation, re-arranging the terms in Eq. 2.17 and setting the tangential velocities for all contact points in set \mathbf{S}^r equal to zero gives:

$$\begin{aligned}
\begin{bmatrix} \mathbf{0} & \mathbf{0} \end{bmatrix} &= \begin{bmatrix} \mathbf{j}_{\mathbf{x},\mathbf{S}} & \mathbf{j}_{\mathbf{y},\mathbf{S}} \end{bmatrix}^{r+1} \underbrace{\begin{bmatrix} \mathbf{C}_{\mathbf{xx},\mathbf{SS}} & \mathbf{C}_{\mathbf{xy},\mathbf{SS}} \\ \mathbf{C}_{\mathbf{yx},\mathbf{SS}} & \mathbf{C}_{\mathbf{yy},\mathbf{SS}} \end{bmatrix}}_{\mathbf{C}'} \\
&+ \underbrace{\begin{bmatrix} \mathbf{j}_{\mathbf{x},\bar{\mathbf{S}}} & \mathbf{j}_{\mathbf{y},\bar{\mathbf{S}}} \end{bmatrix}^{r+1} \begin{bmatrix} \mathbf{C}_{\mathbf{xx},\bar{\mathbf{S}}\mathbf{S}} & \mathbf{C}_{\mathbf{xy},\bar{\mathbf{S}}\mathbf{S}} \\ \mathbf{C}_{\mathbf{yx},\bar{\mathbf{S}}\mathbf{S}} & \mathbf{C}_{\mathbf{yy},\bar{\mathbf{S}}\mathbf{S}} \end{bmatrix} + \mathbf{j}_{\mathbf{n}}^{p+1} \begin{bmatrix} \mathbf{C}_{\mathbf{nx},\mathbf{NS}} & \mathbf{C}_{\mathbf{ny},\mathbf{NS}} \end{bmatrix} + \begin{bmatrix} \mathbf{d}_{\mathbf{x},\mathbf{S}} & \mathbf{d}_{\mathbf{y},\mathbf{S}} \end{bmatrix}}_{\mathbf{d}'} \\
\implies \begin{bmatrix} \Delta\mathbf{j}_{\mathbf{x},\mathbf{S}} & \Delta\mathbf{j}_{\mathbf{y},\mathbf{S}} \end{bmatrix} &= -\mathbf{d}'(\mathbf{C}')^{-1} - \begin{bmatrix} \mathbf{j}_{\mathbf{x},\mathbf{S}} & \mathbf{j}_{\mathbf{y},\mathbf{S}} \end{bmatrix}^r \mathbf{C}'(\mathbf{C}')^{-1} \quad (2.18)
\end{aligned}$$

The matrix \mathbf{C}' may in general be rank deficient. So, there may exist infinitely many so-

lutions for $[\Delta \mathbf{j}_{x,S} \ \Delta \mathbf{j}_{y,S}]$ from the above set of linear equations. However, if the Moore-Penrose pseudo inverse is used for C'^{-1} , then the resulting solution for $[\Delta \mathbf{j}_{x,S} \ \Delta \mathbf{j}_{y,S}]$ is the solution with the least 2-norm. This implies that $[\mathbf{j}_x \ \mathbf{j}_y]^{r+1}$ is the solution closest to $[\mathbf{j}_x \ \mathbf{j}_y]^r$.

Step 3(b)(ii): Satisfying the friction cone constraint.

If friction impulses calculated in the previous step lie outside the friction cone for any point α in \mathbf{S}^r , a scaling factor σ_α is applied to $\Delta j_{x\alpha}$ and $\Delta j_{y\alpha}$ in order to project the friction impulses back to the surface of the friction cone as shown below:

$$(j_{x\alpha}^r + \sigma_\alpha \Delta j_{x\alpha})^2 + (j_{y\alpha}^r + \sigma_\alpha \Delta j_{y\alpha})^2 = \mu_s^2 (j_{n\alpha}^{p+1})^2 \quad (2.19)$$

The positive root of the above quadratic expression is used for σ_α . The contact point $\alpha \in \mathbf{S}^r$, which has the maximum scaling factor (say $\bar{\alpha}$), is then moved to set $\bar{\mathbf{S}}^{r+1}$. This implies that $\mathbf{S}^{r+1} = \mathbf{S}^r \setminus \{\bar{\alpha}\}$ and $\bar{\mathbf{S}}^{r+1} = \bar{\mathbf{S}}^r \cup \{\bar{\alpha}\}$. In accordance with the definition of set $\bar{\mathbf{S}}^{r+1}$, the friction impulses for $\bar{\alpha}$ lie on the surface of the friction cone, and do not change in magnitude or direction as long as it remains in this set. The relative tangential velocity ($\dot{u}_{x\bar{\alpha}}^+$ and $\dot{u}_{y\bar{\alpha}}^+$) when the contact point $\bar{\alpha}$ enters $\bar{\mathbf{S}}^{r+1}$ is stored into $\dot{u}_{x\bar{\alpha}}$ and $\dot{u}_{y\bar{\alpha}}$. In a future friction impulse iteration, if $\dot{u}_{x\bar{\alpha}}^+$ or $\dot{u}_{y\bar{\alpha}}^+$ differ in sign from $\dot{u}_{x\bar{\alpha}}$ or $\dot{u}_{y\bar{\alpha}}$, respectively, then $\bar{\alpha}$ is released from $\bar{\mathbf{S}}$ back to \mathbf{S} . This method of dividing the contact points into sets \mathbf{S}^{r+1} and $\bar{\mathbf{S}}^{r+1}$ offers a simple termination condition for the friction impulse iteration, ensuring convergence is achieved within a few iterations.

Step 3(b)(iii): Termination condition for the friction impulse iteration.

At the end of **Step 3(b)(ii)**, three things can happen: a point may move from \mathbf{S}^r to $\bar{\mathbf{S}}^{r+1}$, few points may move from $\bar{\mathbf{S}}^{r+1}$ to \mathbf{S}^{r+1} , or the sets \mathbf{S}^{r+1} and $\bar{\mathbf{S}}^{r+1}$ remain unchanged from previous friction impulse iteration, i.e., $\mathbf{S}^{r+1} = \mathbf{S}^r$ and $\bar{\mathbf{S}}^{r+1} = \bar{\mathbf{S}}^r$. In the first two scenarios, the algorithm goes back to **Step 3(b)(i)** and continues to the next friction impulse iteration. In the third scenario, when the sets remain unchanged, the friction impulse iteration is terminated with $\mathbf{j}_x^{p+1} = \mathbf{j}_x^{r+1}$ and $\mathbf{j}_y^{p+1} = \mathbf{j}_y^{r+1}$.

Step 3(c): Termination condition for the impulse iteration.

After convergence of the friction impulses \mathbf{j}_x^{p+1} and \mathbf{j}_y^{p+1} , the algorithm goes back to **Step 3(a)** for the next impulse iteration. The impulse iteration is terminated when the

relative change in the normal impulses from the previous impulse iteration is less than a tolerance ϵ_1 , i.e., $\|\mathbf{j}_n^{p+1} - \mathbf{j}_n^p\|_2 \leq \epsilon_1 \|\mathbf{j}_n^p\|_2$. After termination, $\dot{\mathbf{u}}_{\text{cm}}^+$ and $\boldsymbol{\omega}^+$ are calculated using Eqs. 2.13 and 2.14, and $\dot{\mathbf{u}}_{\text{cm}}^{k+1}(t + \Delta t)$ and $\mathbf{I}^{k+1}(t + \Delta t)$ are updated as follows:

$$\dot{\mathbf{u}}_{\text{cm}}^{k+1}(t + \Delta t) = \dot{\mathbf{u}}_{\text{cm}}^+ \quad (2.20)$$

$$\mathbf{I}^{k+1}(t + \Delta t) = \mathbf{I}^{k+1}(t + \Delta t) + \sum_{\beta=1}^q \mathbf{r}_\beta \times j_{n\beta} \mathbf{n}_\beta + \sum_{\beta=1}^q \mathbf{r}_\beta \times j_{x\beta} \mathbf{x}_\beta + \sum_{\beta=1}^q \mathbf{r}_\beta \times j_{y\beta} \mathbf{y}_\beta \quad (2.21)$$

Step 4: Computing the contact forces.

The aim of this step is to calculate contact forces to prevent the rock from accelerating towards the pedestal at the contact points. Let $\mathbf{f} = [\mathbf{f}_n \ \mathbf{f}_x \ \mathbf{f}_y]$, where $\mathbf{f}_n = [f_{n1} \ f_{n2} \ \dots \ f_{nq}]$ etc., be the row vector of length $1 \times 3q$ containing the magnitudes of forces applied at all contact points with respect to their local coordinate systems. Similarly, let $\ddot{\mathbf{u}} = [\ddot{\mathbf{u}}_n \ \ddot{\mathbf{u}}_x \ \ddot{\mathbf{u}}_y]$ be the relative acceleration of the contact points on the rock with respect to the pedestal. The translational ($\ddot{\mathbf{u}}_{\text{cm}}$) and rotational ($\dot{\boldsymbol{\omega}}$) acceleration of the rock are given by:

$$\ddot{\mathbf{u}}_{\text{cm}} = \frac{1}{m} \sum_{\beta=1}^q f_{n\beta} \mathbf{n}_\beta + \frac{1}{m} \sum_{\beta=1}^q f_{x\beta} \mathbf{x}_\beta + \frac{1}{m} \sum_{\beta=1}^q f_{y\beta} \mathbf{y}_\beta + \mathbf{g} \quad (2.22)$$

$$\dot{\boldsymbol{\omega}} = \sum_{\beta=1}^q \mathbf{I}^{-1}(\mathbf{r}_\beta \times f_{n\beta} \mathbf{n}_\beta) + \sum_{\beta=1}^q \mathbf{I}^{-1}(\mathbf{r}_\beta \times f_{x\beta} \mathbf{x}_\beta) + \sum_{\beta=1}^q \mathbf{I}^{-1}(\mathbf{r}_\beta \times f_{y\beta} \mathbf{y}_\beta) + \mathbf{I}^{-1}(\mathbf{l} \times \boldsymbol{\omega}) \quad (2.23)$$

Here, $\mathbf{I}^{-1} = [\mathbf{I}^{k+1}(t + \Delta t)]^{-1}$, $\mathbf{l} = \mathbf{l}^{k+1}(t + \Delta t)$, $\mathbf{r}_\beta = \mathbf{r}_\beta^{k+1}(t + \Delta t)$, $\boldsymbol{\omega} = \boldsymbol{\omega}^{k+1}(t + \Delta t)$, $\ddot{\mathbf{u}}_p = \ddot{\mathbf{u}}_p(t + \Delta t)$, and \mathbf{g} is the acceleration due to gravity in the global coordinate system.

Now, the normal acceleration of contact point α relative to the pedestal is given by $\ddot{u}_{n\alpha} = \mathbf{n}_\alpha \cdot [\ddot{\mathbf{u}}_{\text{cm}} + \dot{\boldsymbol{\omega}} \times \mathbf{r}_\alpha + \boldsymbol{\omega} \times (\boldsymbol{\omega} \times \mathbf{r}_\alpha) - \ddot{\mathbf{u}}_p]$. Similar relations exist for the relative tangential accelerations ($\ddot{u}_{x\alpha}$ and $\ddot{u}_{y\alpha}$) of contact point α . Substituting for $\ddot{\mathbf{u}}_{\text{cm}}$ and $\dot{\boldsymbol{\omega}}$ from Eqs. 2.22 and 2.23 into the above expressions, the affine relation between the relative

accelerations and contact forces at all contact points is obtained:

$$\ddot{\mathbf{u}} = \mathbf{f}\mathbf{A} + \mathbf{b}; \quad \mathbf{A} = \begin{bmatrix} \mathbf{A}_{nn} & \mathbf{A}_{nx} & \mathbf{A}_{ny} \\ \mathbf{A}_{xn} & \mathbf{A}_{xx} & \mathbf{A}_{xy} \\ \mathbf{A}_{yn} & \mathbf{A}_{yx} & \mathbf{A}_{yy} \end{bmatrix}_{3q \times 3q}; \quad \mathbf{b} = \begin{bmatrix} \mathbf{b}_n & \mathbf{b}_x & \mathbf{b}_y \end{bmatrix}_{1 \times 3q} \quad (2.24)$$

$$(A_{nn})_{\alpha\beta} = \frac{1}{m} \mathbf{n}_\alpha \cdot \mathbf{n}_\beta + (\mathbf{r}_\alpha \times \mathbf{n}_\alpha)^T \mathbf{I}^{-1} (\mathbf{r}_\beta \times \mathbf{n}_\beta);$$

$$(A_{xx})_{\alpha\beta} = \frac{1}{m} \mathbf{x}_\alpha \cdot \mathbf{x}_\beta + (\mathbf{r}_\alpha \times \mathbf{x}_\alpha)^T \mathbf{I}^{-1} (\mathbf{r}_\beta \times \mathbf{x}_\beta);$$

$$(A_{yy})_{\alpha\beta} = \frac{1}{m} \mathbf{y}_\alpha \cdot \mathbf{y}_\beta + (\mathbf{r}_\alpha \times \mathbf{y}_\alpha)^T \mathbf{I}^{-1} (\mathbf{r}_\beta \times \mathbf{y}_\beta);$$

$$(A_{xn})_{\beta\alpha} = (A_{nx})_{\alpha\beta} = \frac{1}{m} \mathbf{n}_\alpha \cdot \mathbf{x}_\beta + (\mathbf{r}_\alpha \times \mathbf{n}_\alpha)^T \mathbf{I}^{-1} (\mathbf{r}_\beta \times \mathbf{x}_\beta);$$

$$(A_{yn})_{\beta\alpha} = (A_{ny})_{\alpha\beta} = \frac{1}{m} \mathbf{n}_\alpha \cdot \mathbf{y}_\beta + (\mathbf{r}_\alpha \times \mathbf{n}_\alpha)^T \mathbf{I}^{-1} (\mathbf{r}_\beta \times \mathbf{y}_\beta);$$

$$(A_{yx})_{\beta\alpha} = (A_{xy})_{\alpha\beta} = \frac{1}{m} \mathbf{x}_\alpha \cdot \mathbf{y}_\beta + (\mathbf{r}_\alpha \times \mathbf{x}_\alpha)^T \mathbf{I}^{-1} (\mathbf{r}_\beta \times \mathbf{y}_\beta);$$

$$b_{n\alpha} = \mathbf{n}_\alpha \cdot [\mathbf{g} + \mathbf{I}^{-1}(\mathbf{1} \times \boldsymbol{\omega}) \times \mathbf{r}_\alpha + \boldsymbol{\omega} \times (\boldsymbol{\omega} \times \mathbf{r}_\alpha) - \ddot{\mathbf{u}}_p]$$

$$b_{x\alpha} = \mathbf{x}_\alpha \cdot [\mathbf{g} + \mathbf{I}^{-1}(\mathbf{1} \times \boldsymbol{\omega}) \times \mathbf{r}_\alpha + \boldsymbol{\omega} \times (\boldsymbol{\omega} \times \mathbf{r}_\alpha) - \ddot{\mathbf{u}}_p]$$

$$b_{y\alpha} = \mathbf{y}_\alpha \cdot [\mathbf{g} + \mathbf{I}^{-1}(\mathbf{1} \times \boldsymbol{\omega}) \times \mathbf{r}_\alpha + \boldsymbol{\omega} \times (\boldsymbol{\omega} \times \mathbf{r}_\alpha) - \ddot{\mathbf{u}}_p]$$

The contact points are divided into two sets \mathbf{R} and \mathbf{D} based on the relative tangential velocity. If the relative tangential velocity of a contact point is zero (within a tolerance), then the point belongs to set \mathbf{R} , or else the contact point belongs to set \mathbf{D} . There are a few constraints on the contact forces (\mathbf{f}) and the relative accelerations ($\ddot{\mathbf{u}}$): (i) The normal force at any contact point α should be non-negative, i.e., ($f_{n\alpha} \geq 0$). This condition ensures that the forces only push the rock and the pedestal away and do not make them stick together. (ii) The rock and pedestal should not accelerate towards each other at the contact points, i.e., $\ddot{u}_{n\alpha} \geq 0$. (iii) Normal forces are applied only to make the relative normal accelerations at contact points non-negative, these forces should be zero if this condition is already satisfied at a contact point (i.e., $f_{n\alpha} \ddot{u}_{n\alpha} = 0$).

The conditions on the friction forces vary depending on whether a contact point belongs to set \mathbf{R} or \mathbf{D} . For a contact point α with zero relative tangential velocity and belonging to \mathbf{R} , the forces of friction must satisfy the laws of static Coulomb friction, i.e., the friction

forces should lie on/within the friction cone $\sqrt{f_{x\alpha}^2 + f_{y\alpha}^2} \leq \mu_s(f_{n\alpha})$, and they should oppose the tangential acceleration. As in the case of the impulses, the friction forces should collectively oppose the tangential acceleration of all contact points belonging to \mathbf{R} resulting in the least magnitude of tangential acceleration at these contact points. For a contact point α with non-zero relative tangential velocity and belonging to \mathbf{D} , the forces of friction must comply with laws of kinetic Coulomb friction, i.e., the magnitude of the friction force is $\mu_d f_{n\alpha}$ and the friction forces should directly oppose the relative tangential velocity. Thus,

$$f_{x\alpha} = -\frac{\dot{u}_{x\alpha}}{\sqrt{\dot{u}_{x\alpha}^2 + \dot{u}_{y\alpha}^2}} \mu_d f_{n\alpha}; \quad f_{y\alpha} = -\frac{\dot{u}_{y\alpha}}{\sqrt{\dot{u}_{x\alpha}^2 + \dot{u}_{y\alpha}^2}} \mu_d f_{n\alpha} \quad \forall \alpha \in \mathbf{D} \quad (2.25)$$

Here, μ_d is the kinetic coefficient of friction between the rock and the pedestal. Contact forces are computed iteratively (iterations denoted by “p”) in two alternating steps in a manner analogous to impulse forces (**Step 3**), the first involving the computation of normal forces and the second involving the computation of frictional forces. The contact force iteration is initialized with the contact forces at time t . If the rock is initially resting on the pedestal, the initial values of the contact forces are computed by imposing acceleration due to gravity alone on the rock. The two-step contact force computation is described next.

Step 4(a): Computing normal contact forces.

For ease of notation, let $\mathbf{f}_{n,\mathbf{R}}$ and $\mathbf{f}_{n,\mathbf{D}}$ contain the vector of normal forces for all contact points belonging to sets \mathbf{R} and \mathbf{D} , respectively. Similarly, let $\mathbf{A}_{nn,\mathbf{RR}}$ be the sub-matrix of \mathbf{A}_{nn} corresponding to the points in \mathbf{R} , and so on. Substituting Eq. 2.25 into the normal

part of Eq. 2.24 and re-arranging, we get the following affine relation:

$$\begin{aligned}
\begin{bmatrix} \ddot{\mathbf{u}}_{n,R} & \ddot{\mathbf{u}}_{n,D} \end{bmatrix} &= \begin{bmatrix} \mathbf{f}_{n,R} & \mathbf{f}_{n,D} \end{bmatrix}^{p+1} \begin{bmatrix} \mathbf{A}_{nn,RR} & \mathbf{A}_{nn,RD} \\ \mathbf{A}_{nn,DR} & \mathbf{A}_{nn,DD} \end{bmatrix} \\
&+ \begin{bmatrix} \mathbf{f}_{x,D} & \mathbf{f}_{y,D} \end{bmatrix}^{p+1} \begin{bmatrix} \mathbf{A}_{xn,DR} & \mathbf{A}_{xn,DD} \\ \mathbf{A}_{yn,DR} & \mathbf{A}_{yn,DD} \end{bmatrix} \\
&+ \underbrace{\begin{bmatrix} \mathbf{f}_{x,R} & \mathbf{f}_{y,R} \end{bmatrix}^{p+1} \begin{bmatrix} \mathbf{A}_{xn,RR} & \mathbf{A}_{xn,RD} \\ \mathbf{A}_{yn,RR} & \mathbf{A}_{yn,RD} \end{bmatrix} + \begin{bmatrix} \mathbf{b}_{n,R} & \mathbf{b}_{n,D} \end{bmatrix}^{p+1}}_{\mathbf{b}'} \\
\Rightarrow \begin{bmatrix} \ddot{\mathbf{u}}_{n,R} & \ddot{\mathbf{u}}_{n,D} \end{bmatrix} &= \begin{bmatrix} \mathbf{f}_{n,R} & \mathbf{f}_{n,D} \end{bmatrix}^{p+1} \underbrace{\begin{bmatrix} \mathbf{A}_{nn,RR} & \mathbf{A}_{nn,RD} \\ \mathbf{A}'_{nn,DR} & \mathbf{A}'_{nn,DD} \end{bmatrix}}_{\mathbf{A}'} + \mathbf{b}' \\
\Rightarrow \ddot{\mathbf{u}}_n &= \mathbf{f}_n^{p+1} \mathbf{A}' + \mathbf{b}' \tag{2.26}
\end{aligned}$$

Here, $(A'_{nn})_{\alpha\beta} = (A_{nn})_{\alpha\beta} - \frac{\dot{u}_{x\alpha}}{\sqrt{\dot{u}_{x\alpha}^2 + \dot{u}_{y\alpha}^2}} \mu_d (A_{xn})_{\alpha\beta} - \frac{\dot{u}_{y\alpha}}{\sqrt{\dot{u}_{x\alpha}^2 + \dot{u}_{y\alpha}^2}} \mu_d (A_{yn})_{\alpha\beta}$ for $\alpha \in \mathbf{D}$ and $\beta \in \mathbf{R} \cup \mathbf{D}$. The affine relation between the $\ddot{\mathbf{u}}_n$ and \mathbf{f}_n^{p+1} from Eq. 2.26 along with the normal force constraints may be posed as the following QP:

$$\left. \begin{array}{l} \ddot{\mathbf{u}}_n = \mathbf{f}_n^{p+1} \mathbf{A}' + \mathbf{b}' \\ \mathbf{f}_n^{p+1} \geq \mathbf{0}; \quad \ddot{\mathbf{u}}_n \geq \mathbf{0} \\ \mathbf{f}_n^{p+1} \ddot{\mathbf{u}}_n^T = 0 \end{array} \right\} \Rightarrow \begin{array}{l} \text{minimize } \mathbf{f}_n^{p+1} (\mathbf{f}_n^{p+1} \mathbf{A}' + \mathbf{b}')^T \\ \text{subject to } \mathbf{f}_n^{p+1} \geq \mathbf{0} \\ \mathbf{f}_n^{p+1} \mathbf{A}' + \mathbf{b}' \geq \mathbf{0} \end{array} \tag{2.27}$$

As in the case of the impulses, this is an LCP, i.e., a special QP with the optimal value of objective function equal to zero. However, matrix \mathbf{A}' is not necessarily symmetric or positive semi-definite. This poses a problem as existence of solution is mathematically guaranteed only when the matrix \mathbf{A}' is positive definite or semi-definite or belongs to one of the special classes of matrices discussed in Chapter 3 of [34]. Fortunately, for realistic values of μ_d , the diagonal elements of \mathbf{A}' are in general non-negative and solution does exist for the corresponding LCP. The solution, if and when it exists, may be estimated using an approach analogous to **Step 3(a)**.

Step 4(b): Computing contact frictional forces.

From the previous step, $\mathbf{f}_{n,D}^{p+1}$ is known, and therefore from Eq. 2.25, $\mathbf{f}_{x,D}^{p+1}$ and $\mathbf{f}_{y,D}^{p+1}$ are also known. The aim of this step is to calculate $\mathbf{f}_{x,R}^{p+1}$ and $\mathbf{f}_{y,R}^{p+1}$ such that they oppose $\ddot{\mathbf{u}}_{x,R}$ and $\ddot{\mathbf{u}}_{y,R}$, respectively, at all contact points within/on the static friction cone and belonging to \mathbf{R} . The friction part of the affine relation from Eq. 2.24 is re-ordered to get:

$$\begin{aligned}
\begin{bmatrix} \ddot{\mathbf{u}}_{x,R} & \ddot{\mathbf{u}}_{y,R} \end{bmatrix} &= \begin{bmatrix} \mathbf{f}_{x,R} & \mathbf{f}_{y,R} \end{bmatrix}^{p+1} \begin{bmatrix} \mathbf{A}_{xx,RR} & \mathbf{A}_{xy,RR} \\ \mathbf{A}_{yx,RR} & \mathbf{A}_{yy,RR} \end{bmatrix} \\
+ \begin{bmatrix} \mathbf{f}_{n,R} & \mathbf{f}_{n,D} \end{bmatrix}^{p+1} \begin{bmatrix} \mathbf{A}_{nx,RR} & \mathbf{A}_{ny,RR} \\ \mathbf{A}_{nx,DR} & \mathbf{A}_{ny,DR} \end{bmatrix} &+ \begin{bmatrix} \mathbf{f}_{x,D} & \mathbf{f}_{y,D} \end{bmatrix}^{p+1} \begin{bmatrix} \mathbf{A}_{xx,DR} & \mathbf{A}_{xy,DR} \\ \mathbf{A}_{yx,DR} & \mathbf{A}_{yy,DR} \end{bmatrix} \\
&+ \begin{bmatrix} \mathbf{b}_{x,R} & \mathbf{b}_{y,R} \end{bmatrix} \\
\Rightarrow \begin{bmatrix} \ddot{\mathbf{u}}_{x,R} & \ddot{\mathbf{u}}_{y,R} \end{bmatrix} &= \begin{bmatrix} \mathbf{f}_{x,R} & \mathbf{f}_{y,R} \end{bmatrix}^{p+1} \begin{bmatrix} \mathbf{A}_{xx,RR} & \mathbf{A}_{xy,RR} \\ \mathbf{A}_{yx,RR} & \mathbf{A}_{yy,RR} \end{bmatrix} + \begin{bmatrix} \mathbf{b}'_{x,R} & \mathbf{b}'_{y,R} \end{bmatrix}
\end{aligned} \tag{2.28}$$

This system is similar to Eq. 2.17 and is solved in a manner similar to **Step 3(b)**.

Step 4(c): Termination condition for the contact force iteration.

After computing the friction forces $\mathbf{f}_{x,R}^{p+1}$ and $\mathbf{f}_{y,R}^{p+1}$, the algorithm goes back to **Step 4(a)** for the next contact force iteration. This iteration is terminated when the relative change in the normal forces from the previous contact force iteration is less than a desired tolerance ϵ_1 , i.e., $\|\mathbf{f}_n^{p+1} - \mathbf{f}_n^p\|_2 \leq \epsilon_1 \|\mathbf{f}_n^p\|_2$. Then, the total force $\mathbf{f}_T^{k+1}(t + \Delta t)$ and total torque $\boldsymbol{\tau}_T^{k+1}(t + \Delta t)$ acting on the rock are given by:

$$\mathbf{f}_T^{k+1}(t + \Delta t) = m\mathbf{g} + \sum_{\beta=1}^q f_{n\beta} \mathbf{n}_\beta + \sum_{\beta=1}^q f_{x\beta} \mathbf{x}_\beta + \sum_{\beta=1}^q f_{y\beta} \mathbf{y}_\beta \tag{2.29}$$

$$\boldsymbol{\tau}_T^{k+1}(t + \Delta t) = \sum_{\beta=1}^q \mathbf{r}_\beta \times f_{n\beta} \mathbf{n}_\beta + \sum_{\beta=1}^q \mathbf{r}_\beta \times f_{x\beta} \mathbf{x}_\beta + \sum_{\beta=1}^q \mathbf{r}_\beta \times f_{y\beta} \mathbf{y}_\beta \tag{2.30}$$

Step 5: Termination condition for the time-step iteration k.

After obtaining the total force and torque acting on the rock, the algorithm goes back to **Step 1** for the next time-step iteration. This iteration is terminated when the relative change in the total force and torque from the previous time-step iteration is less than the desired tolerance level ϵ_1 , i.e., $\|\mathbf{f}_T^{k+1} - \mathbf{f}_T^k\|_2 \leq \epsilon_1 \|\mathbf{f}_T^k\|_2$ and $\|\boldsymbol{\tau}_T^{k+1} - \boldsymbol{\tau}_T^k\|_2 \leq \epsilon_1 \|\boldsymbol{\tau}_T^k\|_2$, and the state variables of the rock are deemed to have converged at $t + \Delta t$. After convergence, the algorithm proceeds to the next time integration step. The convergence of the algorithm for each time-step iteration k is not guaranteed. If the number of time-step iterations k exceeds a user defined number of iterations (say 100), the time-step is reduced and the calculations are re-started for the reduced time step.

While it would be ideal for the algorithm to determine the contact force/impulse state that is closest to the previous state of the system (i.e., at time t), our algorithm determines the contact force/impulse state that is closest to the previous iteration of the current step (or the last iteration of the previous step if this is the first iteration of the current step) to achieve faster and more reliable convergence. We have verified that the contact force/impulse configuration closest to the previous state of the system is same as the one closest to the previous step/iteration for simple geometries like 3-D rectangular blocks. We have not yet been able to verify this for rocks due to convergence issues with finding the contact force/impulse configuration closest to the previous state of the system.

2.2 Validation of the algorithm

For a rigid rectangular block placed on a rigid horizontal ground [Fig. 2.2(a)], Shenton H. [95] obtained the relation between the horizontal ground acceleration and the coefficient of friction required to initiate the response of the block in rocking, sliding, or coupled rocking-sliding mode. Shenton H. [95] used force and moment balance equations to arrive at the separatrix between the different response modes. Here, we consider an analogous problem of a rigid rectangular block impacting a rigid horizontal ground. At the instant before the impact, the block is assumed to be translating with a horizontal velocity ($\dot{u}_x > 0$) and a vertical velocity ($\dot{u}_y < 0$) in the presence of gravitational acceleration. Under the assumption that the impact between the block and ground is inelastic, i.e., $e = 0$, the block

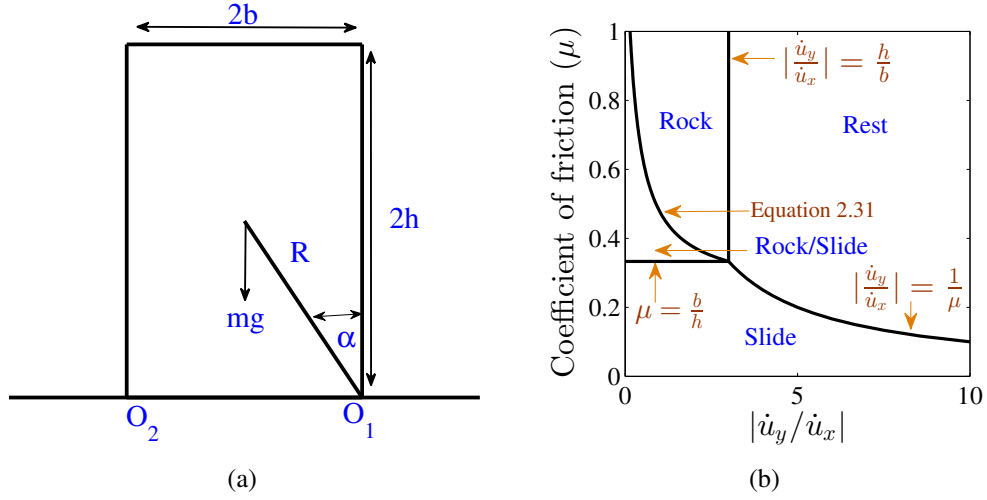


Figure 2.2: (a) Rigid rectangular block and ground (b) motion of block after it impacts the ground as a function of initial velocity and coefficient of friction.

may come to rest, may start to rock, may slide, or may experience sliding coupled with rocking after the impact. Therefore, an approach similar to Shenton's method, involving conservation of linear and angular momentum, may be used to arrive at the separatrix between the different modes as a function of the translational velocities before impact (\dot{u}_x and \dot{u}_y) and the coefficient of friction ($\mu_s = \mu_d = \mu$) between the two surfaces [Fig. 2.2(b)]. The details of this calculation are presented in Appendix B. For example, the separatrix between the rocking mode and the coupled rocking-sliding mode is given by:

$$\left| \frac{\dot{u}_y}{\dot{u}_x} \right| = \frac{4 + \left(\frac{h}{b}\right)^2 - 3\mu\frac{h}{b}}{\mu[1 + 4\left(\frac{h}{b}\right)^2] - 3\frac{h}{b}} \quad (2.31)$$

For this analysis, the rigid block [Fig. 2.2(a)] considered has a half height $h = 0.6$ m, half width $b = 0.2$ m, and mass $m = 100$ kg, and it may only come in contact with the ground at points O_1 and O_2 . The motion of the block after impact is governed by Lagrangian mechanics with the reduced translational and rotational velocity of the center of mass after inelastic impact as initial conditions. These velocities are also obtained by conserving angular and linear momentum as shown in Appendix B. Here, we select two combinations of $|\dot{u}_y/\dot{u}_x|$ and μ corresponding to the rocking and the coupled rocking-sliding modes and compare the solutions obtained from the rigid body dynamics algorithm with that obtained

by time-integrating the equations of motion for the corresponding response modes.

2.2.1 Rocking mode

The block will experience rocking coupled with sliding after impact for $\dot{u}_y = -2.8$ m/s, $|\dot{u}_y/\dot{u}_x| = 1.5$, and $\mu = 0.9$. The angular displacement of the block (θ) is positive when the block rotates about O_2 and negative for rotations about O_1 . The non-linear equation of motion for the rocking mode can be obtained by moment balance about the rocking points O_1 and O_2 :

$$I\ddot{\theta} = mgR\sin(\alpha + \theta) \quad \theta < 0 \quad (2.32)$$

$$I\ddot{\theta} = -mgR\sin(\alpha - \theta) \quad \theta > 0 \quad (2.33)$$

Here, α is a measure of the slenderness of the block [$\alpha = \tan^{-1}(b/h)$], I is the moment of inertia of the block about corner O_1 or O_2 , and R is the distance of the contact points from the center of mass of the block. In the current example, the block starts rocking about corner O_1 after impact with the ground. Therefore, Eq. 2.32 is time integrated using the 4th order Runge Kutta method with the rotational velocity of the block after impact [Eq. B.10] as initial condition. The reduction in the rotational velocity on inelastic impact during rocking, i.e., when point of rotation changes from O_1 to O_2 or vice versa, is modeled using the expression presented by Kimura and Iida [64, 65] and Housner [52]:

$$\frac{\dot{\theta}^+}{\dot{\theta}^-} = \frac{1 + 3\cos(2\alpha)}{4} \quad (2.34)$$

Here, $\dot{\theta}^-$ and $\dot{\theta}^+$ are the rotational velocities of the block before and after impact with the ground. The resulting angular displacement time history [$\theta(t)$] of the block can be easily converted to arrive at the horizontal (x) displacement time history of the block's center of mass, which is then compared against that obtained from rigid body dynamics algorithm Fig. 2.3(a). The good agreement in the results indicate that the rigid body dynamics algorithm is capable of accurately predicting the response mode of the block and simulating the subsequent rocking response of the block.

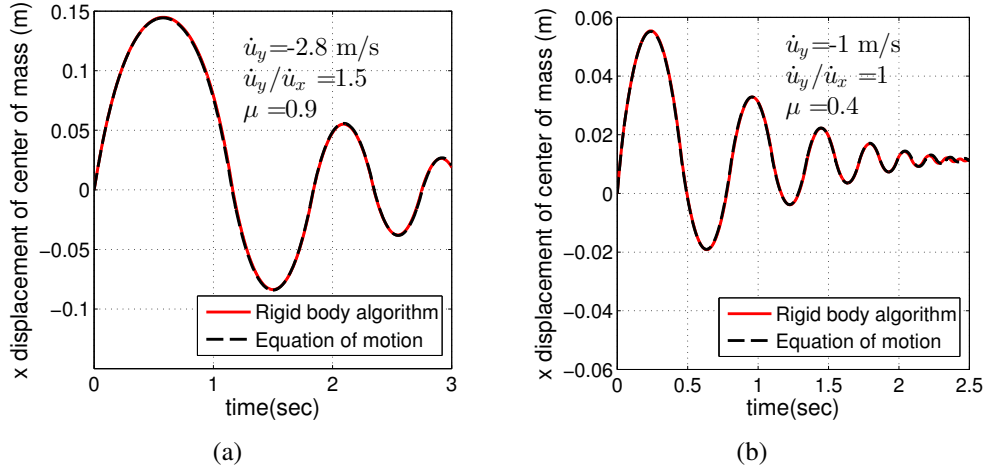


Figure 2.3: Comparison of x displacement time history of center of mass given by the rigid body dynamics algorithm against analytical solution for (a) rocking mode and (b) coupled rocking-sliding mode. For the rocking mode, $\dot{u}_y = -2.8$ m/s, $|\dot{u}_y/\dot{u}_x| = 1.5$ and $\mu = 0.9$. For the coupled rocking-sliding mode, $\dot{u}_y = -1$ m/s, $|\dot{u}_y/\dot{u}_x| = 1$ and $\mu = 0.4$.

2.2.2 Coupled rocking-sliding mode

The block will rock and slide after impact for $\dot{u}_y = -1$ m/s, $|\dot{u}_y/\dot{u}_x| = 1$ and $\mu = 0.4$. The angular displacement of the block (θ) is positive when the block rotates about O_2 and negative for rotations about O_1 . Ishiyama worked out the nonlinear equations of motion for the coupled rocking-sliding mode (Eqs. 1-3 in [58]). These equations of motion are time integrated using the 4th order Runge Kutta method to obtain horizontal (x) displacement time history of the block's center of mass. When the block stops sliding, i.e, when the horizontal velocity of O_1 is zero (within a tolerance), the subsequent rocking response of the block is modeled using Eqs. 2.32-2.34. For the combination of velocities and friction coefficient considered, the block stops sliding before the point of rotation changes from O_1 to O_2 .

The horizontal (x) displacement time history obtained from these differential equations is compared with that obtained from the rigid body dynamics algorithm as shown in Fig. 2.3(b). The results obtained using the rigid body dynamics algorithm agree well with the analytical results.

2.3 Summary

In this chapter, we developed an algorithm to simulate the interaction between the rock and the pedestal. This algorithm is a fairly generic algorithm that is capable of modeling the complex sliding and rocking response of the rock. Unlike the earlier algorithm developed by Baraff, our algorithm is robust and is not sensitive to parameters external to the problem description like the ordering of the points describing the contact interface and choice of coordinate frame. The algorithm is validated against analytical results for the rocking and coupled rocking-sliding response of a simple 2-D rectangular block.

This algorithm can be easily extended to model the interaction between multiple rigid bodies with appropriate changes to the contact detection step. The computation time increases with the number of the rigid bodies as the contact forces and impulses between each pair of rigid bodies need to be estimated. Therefore, while this algorithm may be used to model the response of a stack of rigid bodies, it may not be the best approach to model interaction between thousands of rigid bodies like in granular mechanics simulations.

Chapter 3

Toppling analysis of precariously balanced rocks

3.1 Introduction

The presence of a precariously balanced rock (PBR) in a region is evidence for the fact that earthquake shaking strong enough to overturn it has not occurred there during the rock's existence in that precarious condition. Therefore, the critical toppling intensity of a PBR in conjunction with its age may provide an independent constraint on historic peak ground motion, and, by extension, an estimate of future peak ground shaking in that region. Brune [25] has conducted road surveys near major fault zones and cataloged hundreds of PBRs in Southern California and Nevada. Using the minimum constant ground horizontal acceleration, henceforth referred to as the quasi-static toppling acceleration a_g^s , required to overturn them, he has classified them as precarious ($0.1 g \leq a_g^s \leq 0.3 g$) or semi-precarious ($0.3 g < a_g^s \leq 0.5 g$). a_g^s may be estimated by in-situ tilt tests [9]. A rough estimate of a_g^s may also be obtained from images of the rock [90].

Most PBRs in southern California and Nevada have evolved naturally through weathering of a buried rock mass into corestones, followed by erosion of the overlying surface materials [72]. PBRs thus formed are not connected to their pedestals. The ages of these rocks may be determined using surface exposure dating techniques like varnish microlamination (VML) and cosmogenic ^{36}Cl dating methods [15]. Bell et al. [15] analyzed the varnish on the surfaces of several rocks in southern California and their supporting pedestals using the

VML method. They concluded that most PBRs in southern California have been exposed for at least 10,500 radiocarbon years, i.e., approximately 12,000 calendar years, without significant alteration in their present shape.

The focus in this chapter is on estimating the critical toppling intensity of the PBRs. The current practice relies entirely on the empirical expression developed by Purvance et al. [88]. They numerically simulated the rocking and overturning response of symmetric and asymmetric blocks under synthetically generated random vibration excitations and used these results to develop the empirical expression. This expression estimates the overturning probability of a block as a function of its geometric parameters and various ground motion intensity measures such as peak ground acceleration (PGA), the ratio of peak ground velocity (PGV) to PGA (PGV/PGA), and spectral acceleration at 1 s (S_a^{1s}) and 2 s (S_a^{2s}).

The empirical equation, developed for 2-D rectangular blocks with two-point contact, does not account for the 3-D form of the rock or the curved form of basal contact (with multiple contact points) and predicts greater stability for the rock than what is observed in the experiments. To correct for the multiple contact points, Purvance et al. [88] conducted tilt tests on the rocks and adjusted the location of the two sharp contact points in the 2-D block model based on the ratio of the quasi-static toppling acceleration a_g^s to the acceleration due to gravity. They validated this methodology by comparing the results from the empirical relation with experiments on three rocks.

These results are a great starting point to understanding the dynamics of PBRs, but the idealizations and assumptions inherent in these analyses could have a significant impact on their critical toppling intensity. The empirical expression derived by Purvance et al. [91] assumes the response of the object to be restricted to the plane of applied excitation. While this is true for a rectangular block under uni-axial ground excitation, for most rocks this may not be true owing to their 3-D geometry and complex rock-pedestal interface. Moreover, non-destructive tilt tests need to be conducted to obtain realistic results from the empirical relation. But the inaccessible locations of most PBRs make it difficult to perform tilt tests.

Here, we present an alternate method to analyze the 3-D PBR models using the rigid

body dynamics algorithm detailed in Chapter 2. We validate the algorithm with results from the Purvance et al. [88] rock-on-shake-table experiments and estimate the ground motions required to topple the Echo Cliff PBR [Fig. 3.1(a)] located near the western Santa Monica mountains and the Pacifico rock [Fig. 3.1(b)] present near the San Andreas Fault. The results from the analysis of these rocks are used as independent checks of the seismic hazard map and synthetic ground motion simulations at these locations.

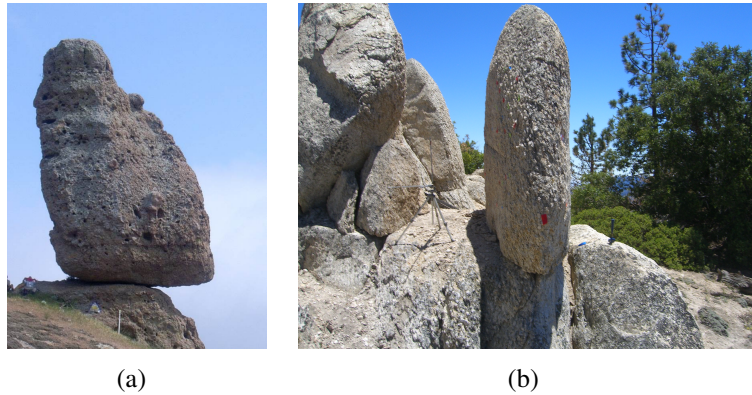


Figure 3.1: A close-up picture of the (a) Echo Cliff PBR located near western Santa Monica mountains and (b) the Pacifico rock located approximately 12 km from the San Andreas Fault.

3.2 Modeling the geometry of the PBR-pedestal system

The rigid body dynamics algorithm discussed in Chapter 2 assumes the rock and the pedestal to be separate rigid bodies. The pedestal is assumed to have infinite mass and mass moment of inertia, implying that it moves integral to the ground. We further assume that the ground and the pedestal only translate, but do not rotate (i.e., rotational ground motions are not considered). The input to the algorithm includes the coordinates of points describing the surfaces of the pedestal and the rock, the volume, mass moment of inertia and center of mass of the rock, and the coefficients of static and kinetic friction at the rock-pedestal interface and coefficient of restitution between the rock and pedestal.

Two popular methods for obtaining the rock and pedestal surficial coordinates are photogrammetry and more recently Terrestrial Laser Scanning (TLS). In the photogrammetry method, pictures taken from different angles are combined to construct the 3-D point cloud

describing the geometry of the rock and its pedestal. Any inexpensive digital camera may be calibrated and used for this purpose. The pictures can be combined using commercial (e.g., PhotoModeler [2]) or open source (e.g., Insight3D [1]) photogrammetry software packages. This method captures the shape of the rock well, but the interface between the rock and pedestal may need to be modified to ensure accurate contact modeling. Purvance et al. [89] used PhotoModeler to create 3-D models of PBRs for use with RIGID.

Laser scanning techniques estimate the position of an object relative to the laser by measuring the time taken for the light beam to reach the object and, upon reflection, travel back to the sensor (which is typically embedded in the laser-emitting device). For imaging a rock, a laser is mounted on a tripod and the laser beam is aimed at different regions of the rock and its pedestal. This gives the coordinates of each point on the rock-pedestal system with respect to the laser coordinate system. A powerful laser within close proximity of the rock may thus be used to obtain an accurate geometric representation of the rock-pedestal system, including details of the rock-pedestal interface. However, this technique requires the use of moderately heavy and sophisticated equipment. The Echo-Cliff PBR [Fig. 3.1(a)], located in the western Santa Monica mountains, was imaged by Hudnut et al. [54] using TLS. This rock is approximately 14 m high and 10 m wide. The rock was scanned from five surrounding locations and the data was combined to construct a single point cloud describing the geometry of the rock and the pedestal [Fig. 3.2(a)].

The modeling of the rock-pedestal system involves the following steps (illustrated using the Echo Cliff PBR-pedestal system as an example):

- 1. Identifying the rock-pedestal “initial interface plane”:**

We start by taking a slice of the dense point cloud (obtained from TLS or photogrammetry) that fully encloses the rock-pedestal interface [Fig. 3.2(b)]. This slice is selected visually (spanning about 0.5 m along the Z axis for the Echo Cliff PBR). We refer to the points within this slice as the “dense interface-point cloud”. In order to stabilize our model under gravity, we assume that the initial contact between the rock and pedestal occurs on the best-fitting plane to the dense interface-point cloud. This “initial interface plane” is mathematically determined using the linear least squares

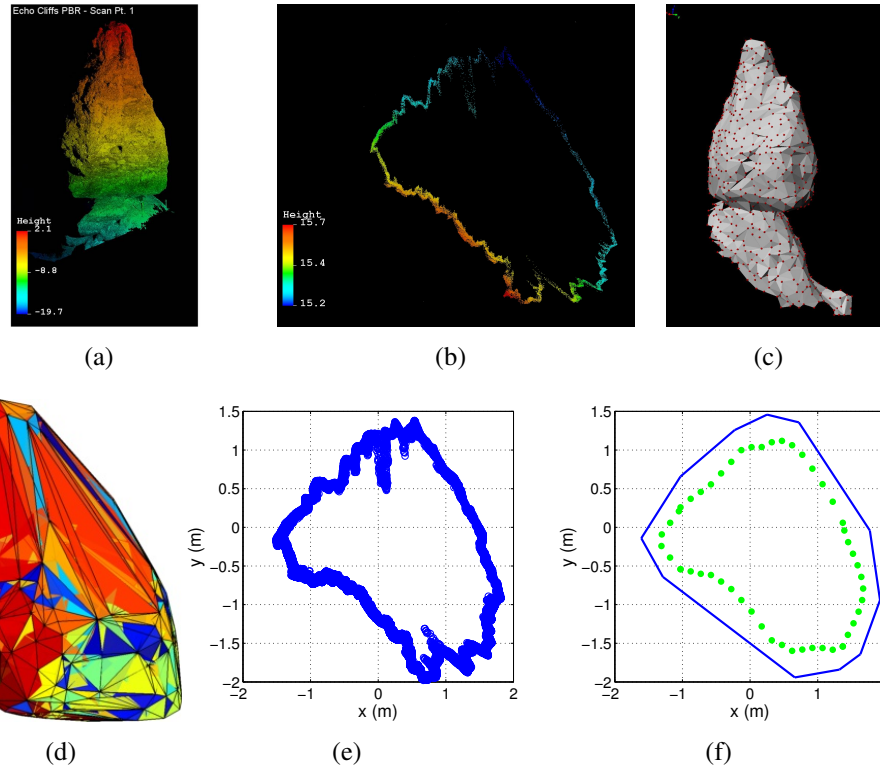


Figure 3.2: Echo Cliff PBR: (a) The dense point cloud obtained from TLS. (b) The slice of points that encloses the rock-pedestal interface (dense interface-point cloud). (c) The pruned coarse point cloud. (d) Delaunay triangulation of the coarse point cloud. (e) Plan (x-y) view of the dense interface point cloud. (f) Inner (green dots) and outer (blue line) loops enveloping the points in (e). The green dots constitute the initial set of contact points.

method. The assumption of a planar contact area is not far from reality as evidenced by the goodness of fit parameter R^2 for the linear least square fit being close to unity.

2. Determining the physical properties of the rock:

The dense TLS point cloud is pruned to extract a coarser point cloud [Fig. 3.2(c)]. To minimize the processing time and computational resources needed, we use the coarser point cloud to characterize the volume of the rock (and its physical properties) and the undulating surface of the pedestal. The points in the coarse point cloud that lie above the initial interface plane are classified as “rock” points and those that lie below the pedestal are classified as “pedestal points”. This is followed by Delaunay triangulation [36] on the coarsely spaced “rock” points, creating a void-free 3-D polygon [Fig. 3.2(d)] formed by a collection of non-overlapping tetrahedrons. Under

the assumption that the density of the rock is constant throughout, the basic physical properties of the rock (mass m , mass moment of inertia \mathbf{I} and center of gravity $c.g.$) are calculated by combining the physical properties of all the tetrahedrons. If the rock surface is more or less convex (as in the case of the Echo Cliff PBR), the 3-D polygon model of the rock is a good geometric representation of the actual rock. If, however, the surface of the rock is substantially concave, it may need to be divided into smaller sub-domains, with a 3-D polygon constructed for each sub-domain. The number and sizes of the sub-domains depend upon the curvatures present and the desired precision in approximating the concave surface of the rock in its geometric model.

3. **Determining the initial contact points:**

The points from the dense interface-point cloud are projected onto the initial interface plane [Fig. 3.2(e)]. Two closed loops that enclose all the points are traced out [Fig. 3.2(f)]. The outer loop is the convex envelope or the 2-D polygon circumscribing all the points in Fig. 3.2(e). The points belonging to the inner loop are manually picked to remove any sharp protrusions and the resulting set of points are then smoothed using a cubic spline. The area within the inner loop is where the rock is initially in contact with the pedestal and the vertices of this polygon are the initial contact points. They are appended to the “rock” points from step (ii). The vertices of the outer polygon are appended to the “pedestal” points also from step (ii). This ensures that the outward normal to the pedestal is unambiguously defined at each of the initial contact points.

4. **Identifying contact point candidates for future time steps:**

The rigid body dynamics algorithm evaluates the rocking and sliding of the rock on the pedestal by time-integrating the equations of motion, iteratively satisfying dynamic equilibrium in the displaced configuration of the rock. The set of points on the rock that are in contact with the pedestal is continuously updated in each iteration of a time step. Smooth and accurate tracking of the rocking and sliding motion of the rock is best achieved using a finely sampled rock surface with a closely spaced

set of candidate contact points to choose from. The coarse cloud of points used in the determination of the physical properties of the rock in step (ii) will not suffice. A higher resolution of points is needed, especially near the rock's base.

To obtain varying resolution of points, we create two 3-D rectangular grid of points, a coarse grid spanning the entire height of the rock-pedestal system (with a grid spacing of 0.6 m for the Echo Cliff PBR) and a finer grid spanning only the part of the rock near its base (with a grid spacing of 0.1 m for the Echo Cliff PBR). The finer grid extends to about 1 m above the highest initial contact point from step (iii). The dense interface-point cloud from step (i) is combined with the “rock” points of step (ii). Delaunay triangulation is performed on this set of points to obtain a second 3-D polygon in the same manner as in step (ii). The grid points from the finer 3-D grid that lie inside or on this 3-D polygon are extracted. Likewise, the grid points from the coarser 3-D grid that lie inside or on the 3-D polygon from step (ii) are also extracted. Of these, the points at a given grid elevation (Z coordinate) constitute the horizontal (X - Y) cross-section of the rock at that elevation. The outermost points at each elevation are combined to describe the outer surface of the rock [Fig. 3.3]. These are all the points at which the rock may come in contact with the pedestal in future time steps.

5. Constructing the pedestal surface:

A piecewise linearly interpolated pedestal surface is created from the “pedestal” points of steps (ii) and (iii). On plan (horizontal), the pedestal surface forms a grid. The outward normal to the pedestal surface at each grid point is calculated based on the vertical elevation of the that grid point and its four closest neighbors. The coordinates of the points constituting the pedestal surface and the outward normal at these points constitute the final set of inputs to the rigid body dynamics algorithm.

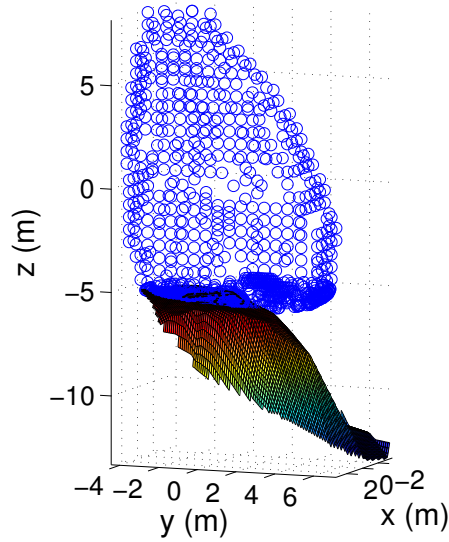


Figure 3.3: Final 3-D model with the pedestal surface and the points representing the nodes on the outer surface of the rock.

3.3 Material properties of PBR-pedestal system

The approximation of the PBR and its pedestal to rigid bodies eliminates the need to characterize stiffness-related properties such as Young's modulus, shear modulus and bulk modulus, and strength-related properties such as fracture toughness and crushing (compressive) strength. Also, the response of a rigid body depends not on the absolute, but on the relative distribution of mass density. If the rock is further assumed homogeneous (i.e., the mass density is uniform), then the dynamic response does not depend on the numerical value of the mass density. The only material-related properties that need to be defined are the coefficients of static friction, kinetic friction, and restitution between the PBR and its pedestal so that relative sliding and impact may be modeled.

Byerlee [27] reviewed the results from friction experiments on different rock types subjected to varying normal stresses. He inferred that the friction coefficient is independent of rock type/material and varies between 0.6 and 1.0 for rocks under low normal stresses (<5 MPa). The weight of a PBR divided by the area of contact with its pedestal is usually less than 5 MPa. For example, the normal stress applied by the Echo Cliff PBR on its pedestal is in the range of 1-1.5 MPa based on commonly encountered rock densities of 2000-3000 kg/m^3 . Therefore, the static and kinetic friction coefficients between a PBR and

its pedestal may be assumed to be in the range of 0.6-1.0.

The rebound velocity of a rigid body upon impact is characterized by the coefficient of restitution. In the shake experiments conducted by Purvance et al. [88], the rebound velocity of the rock upon impact with the table was negligible. Therefore, the coefficient of restitution between the PBR and its pedestal is assumed to be zero and rock-to-pedestal collisions are assumed perfectly inelastic.

3.4 Validation of the rigid body dynamics algorithm

The rigid body dynamics algorithm has been validated against analytical solution of the rocking-sliding-impacting of simple rigid-body assemblies such as a rectangular block on a horizontal surface in Chapter 2. To validate the accuracy of the algorithm in analyzing real rocks with complex 3-D shapes, we use the results from shake table tests of an actual rock [Fig. 3.4(a)] labeled ‘K’ in [88]. Starting with multi-directional images of the rock, obtained from Purvance (personal communication), we constructed the 3-D point cloud describing the rock and its pedestal (a flat surface in this case) using Insight3D [Fig. 3.4(b)]. This software uses the paper targets with unique symbols to align the images precisely and form the 3-D shape. The point cloud obtained using Insight3D does not have sufficient resolution to capture the interface between the rock and the pedestal accurately. Therefore, the points near the rock-pedestal interface need to be manually adjusted with the use of the multi-directional images to ensure accurate contact modeling. Starting with this point cloud, the 3-D geometry of the rock is created using the procedure outline earlier [Fig. 3.5].

Purvance et al. [88] subjected rock ‘K’ to scaled versions of ten single component ground motion waveforms on the shake table. Of these, two are synthetically generated and one is a 2 Hz full sine wave. The remaining ground motion histories are the strong component of recorded ground motion from various earthquakes (N90E component of the 1999 Chi-Chi Earthquake recorded at station TCU074, N0E component of the 1985 Michoacan Earthquake recorded at Caleta de Campos, N51E and N321E components of the 2002 Denali Earthquake recorded at Pump Station 10, N230E component of the 1979 Imperial Valley earthquake recorded at the El Centro Array Station 5, N90E component of

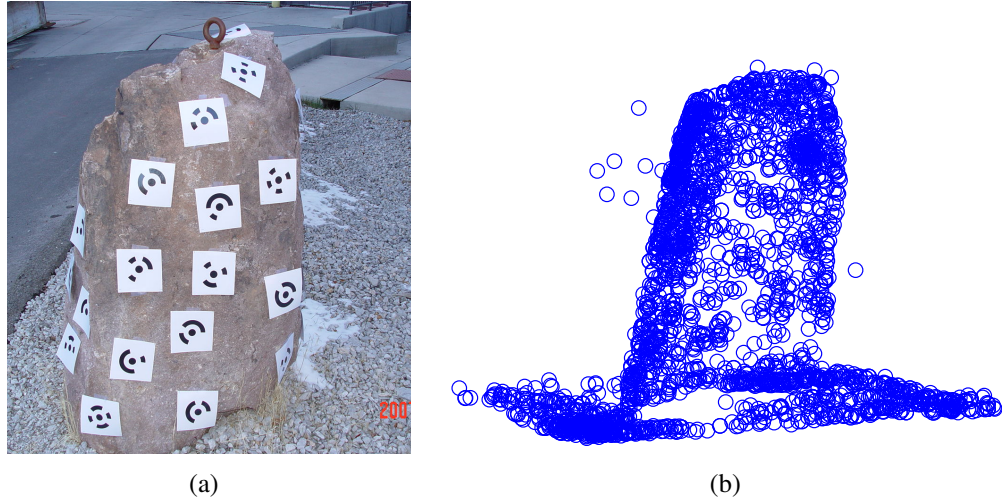


Figure 3.4: (a) An image of Purvance et al.'s rock 'K' and (b) the point cloud obtained by combining the multi-directional images of rock 'K' using Insight3D.

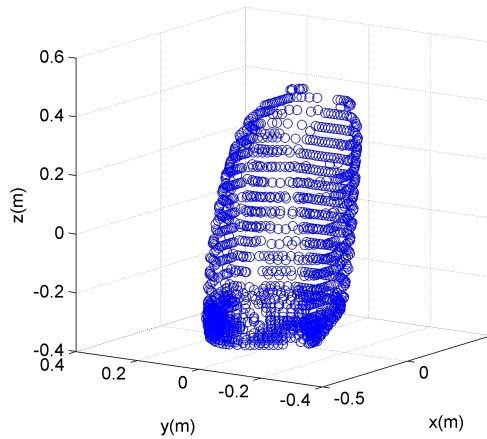


Figure 3.5: 3-D model of Purvance et al.'s rock 'K' created from multi-angle images of the rock.

the 1999 Duzce earthquake recorded at Izmit, and N0E component of the 1999 Chi-Chi Earthquake recorded at station TCU052). The ten waveforms were first normalized such that their PGA is 1 m/s^2 . Then, they are scaled up in steps of 0.025 g from a PGA of 0.1 g to a level at which the rock overturns. The peak ground displacement (PGD) of the records was maintained below the 0.3 m displacement capacity of the shake table by applying a low-frequency filter to the waveforms. The rock is placed on a roughened concrete slab to preclude sliding. Ground motions are applied in the direction in which least PGA is required to initiate rocking. The smallest PGA at which the rock overturns under the scaled versions of the ten waveforms is shown plotted (black squares) as a function of the wave-

form PGV/PGA ratio in Fig. 3.6(a). While the PGV/PGA ratio of a waveform remains unchanged under linear scaling, it does change when a low frequency filter is applied. Therefore, the average PGV/PGA for each waveform is used in developing Fig. 3.6(a).

Here, the 3-D model of the rock is analyzed using the rigid body dynamics algorithm. The pedestal is taken to be a flat horizontal surface as in the experimental setup. The no-slip boundary condition is enforced through the use of a high value of 2.0 for both static and kinetic friction coefficients between the rock and the pedestal. The rock model is analyzed under the same set of scaled ground motion waveforms. The PGD is limited to 0.3 m as in the experiment using a highpass butterworth filter. The smallest PGA at which the rock model overturns under each scaled waveform is indicated by the red filled circles in Fig. 3.6(a). Clearly, the results from the rigid body dynamics algorithm agree well with those from experiments, with the differences in the minimum overturning PGA being less than 0.1 g for most waveforms. The only waveform for which the mismatch exceeds 0.1 g is the sine wave (PGV/PGA=0.09), which has a short duration of 0.5 s. It is unclear as to why the results for the sine wave do not match. One possible reason may be that the rock experienced sliding coupled with rocking. In the shake table experiment for a different rock, sliding was observed at lower values of PGV/PGA, resulting in higher overturning accelerations. It is difficult to judge from the shake table experiment videos whether this rock also experienced sliding at lower PGV/PGA values as the rock's base is not clearly visible.

To verify the empirical expression that they had developed, Purvance et al. [88] approximated the rock to a 2-D rectangular block with two points of contact [Fig. 3.6(b)]. First, they took the two extreme points at which the rock is initially in contact with the concrete slab as the contact points. Using their empirical equation, they estimated the gray region in Fig. 3.6(a) as the combination of PGA and PGV/PGA for which the overturning probability of the rock is between 0.05 and 0.95. It is clear that the shake-table tests demonstrate the rock to be far more fragile than what the empirical equation predicts. Second, they used tilt tests to correct for the positions of the two contact points and re-estimated the overturning fragility. They were able to improve the prediction significantly. Unfortunately, most PBRs are located in difficult terrain and inaccessible locations. It is usually not possible

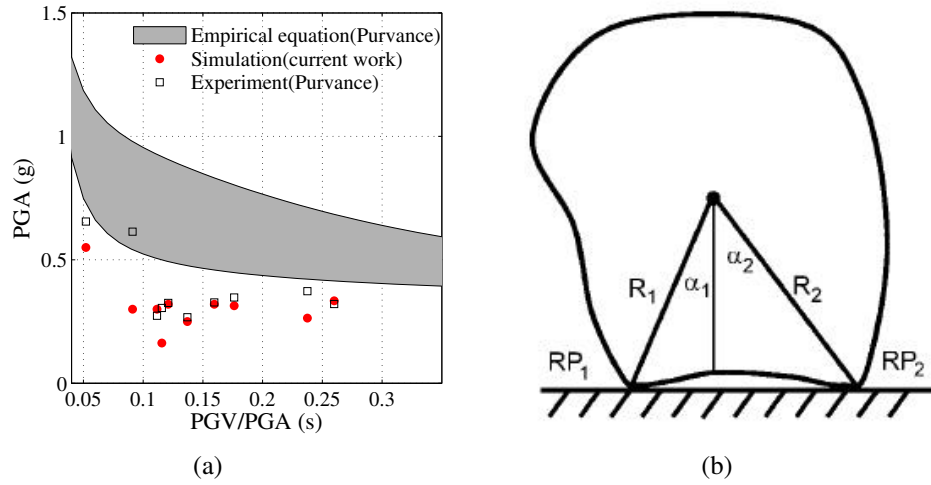


Figure 3.6: (a) The minimum PGA required for Purvance et al.’s rock ‘K’ to overturn under scaled versions of ten ground motion waveforms characterized by their PGV/PGA (black squares: experiment; red circles: rigid body dynamics simulation). The gray region is the combination of PGA and PGV/PGA for which the overturning probability of the rock is between 0.05 and 0.95 from Purvance et al.’s empirical equation [88]. (b) The approximate 2-D block model of the rock used by Purvance et al. with $\alpha_1=0.32$ and $\alpha_2=0.30$.

to perform tilt tests on them. In the absence of tilt tests, our algorithm should clearly be preferred over the empirical equation.

3.5 Critical toppling intensity of the Echo Cliff PBR

Real world PBRs are quite unlike the laboratory-tested regularly shaped rock ‘K’ sitting on a flat horizontal surface. The Echo-Cliff PBR is a case in point. It is asymmetric, resting at the edge of a cliff on a downsloping (with a gradient of about 5°) pedestal [Fig. 3.2(b)], with an overhang of about 4 m (Fig. 3.7). Both the gradient and the overhang are oriented at a counter-clockwise (CCW) angle of approximately 135° to the X axis. As a consequence, the rock may be particularly vulnerable to sliding, rocking, or coupled rocking-sliding along this direction, with gravity aiding the earthquake excitation in toppling the rock. Of course, given the complex asymmetric geometry of the rock-pedestal system, its dynamic response may be sensitive to the directionality of ground motion as well.

The effects of ground excitation direction and sliding are considered separately. To

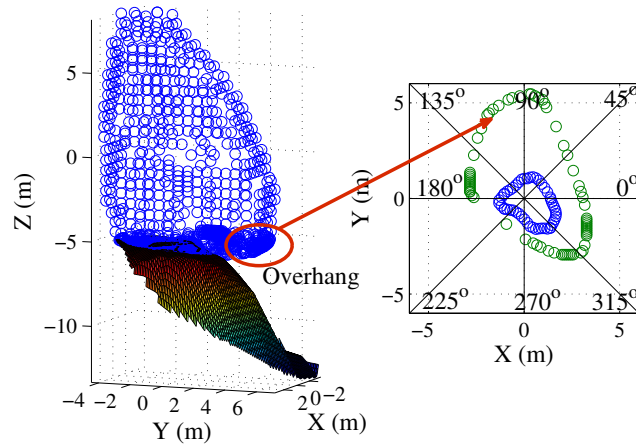


Figure 3.7: 3-D model of the rock and the pedestal. In the figure to the right, plan view of the initial contact interface (blue circles) and the widest part of the rock's base (green circles) are presented. The overhanging part of the rock's base is located around 135° CCW from the X axis.

isolate the effect of the direction of ground excitation, the static and kinetic coefficients of friction between the rock and its pedestal are set to 1.0 (the upper limit of the range of friction coefficients seen in rocks). With friction coefficients being so high, the rock may be expected to experience rocking predominantly with little or no sliding under ground excitation. We estimate the overturning probability of the rock as a function of ground motion parameters by subjecting it to an ensemble of 140 records from worldwide earthquakes with magnitudes greater than 6 and source-to-site distances less than 100 km (see [89] for the complete list of earthquakes).

The records are first normalized such that the PGA of the strong ground motion component is 1 m/s^2 . The response spectra corresponding to the strong ground motion component and the orthogonal horizontal component of these normalized earthquake records are presented in Fig. 3.8. The normalized records are scaled to yield records with PGA from 1 m/s^2 to 19 m/s^2 in steps of 1 m/s^2 . To study the effect of ground motion directionality, 3-component acceleration histories are applied to the pedestal with the strong horizontal component oriented alternately in eight different directions, namely at 0° , 45° , 90° , 135° , 180° , 225° , 270° , and 315° counter-clockwise to the X axis. Note that the pedestal accelerating in the 0° direction will invoke the rock to respond in the opposite direction, i.e., at

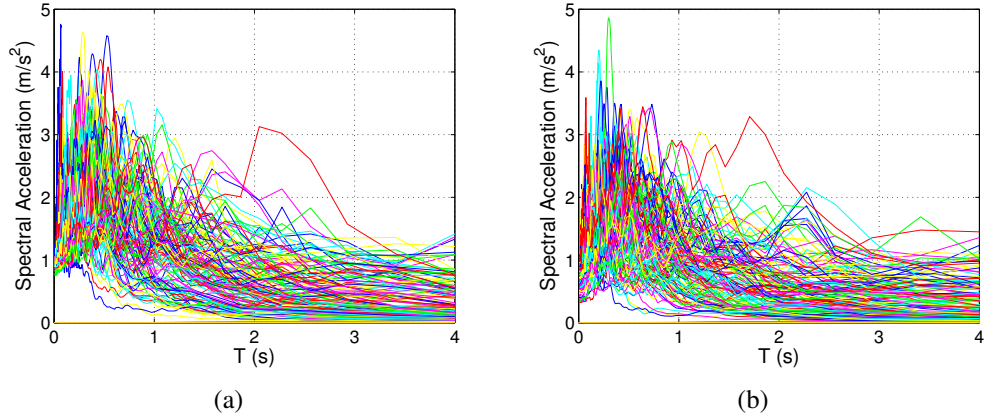


Figure 3.8: Response spectra for the (a) strong ground motion component and (b) orthogonal horizontal component of the 140 normalized ground motions.

180°. The rock-pedestal system is analyzed under the 2660 PGA-scaled earthquake records in each of the 8 directions. The overturning probability of the rock as a function of PGA and PGV/PGA is shown in Fig. 3.9 for each of the eight excitation directions. These plots are developed by binning the 140 scaled records at each PGA level into PGV/PGA bins of 0.05 s width. The overturning probability in each bin at each PGA level is the fraction of records (in that bin and that PGA level) that overturn the model. The sampling of different regions of the domain can be gauged by the thickness of each column. The thicknesses of the columns along the PGV/PGA axis are proportional to the fraction of earthquake records (out of 140) that are sampled in a given PGV/PGA bin. Regions with thinning columns are regions that are sparsely sampled; obviously, the results there may not be as reliable as the densely sampled regions. The colored contour lines correspond to overturning probabilities of 0.1, 0.5, and 0.9.

The overturning probability of the rock is very low for PGA less than 3 m/s^2 [Fig. 3.9]. The quasi-static toppling acceleration of the rock, i.e., the minimum constant ground acceleration that can overturn the rock, varies between $2\text{-}4 \text{ m/s}^2$ depending on the direction of ground excitation. In a few cases at least, it appears that the rock overturns at PGAs smaller than the quasi-static toppling acceleration. For example, if we were to force the rock to topple in the 315°CCW direction, i.e., directly opposing the gradient of the pedestal, the quasi-static toppling acceleration to be applied in the 135° direction would have to be 3.65 m/s^2 .

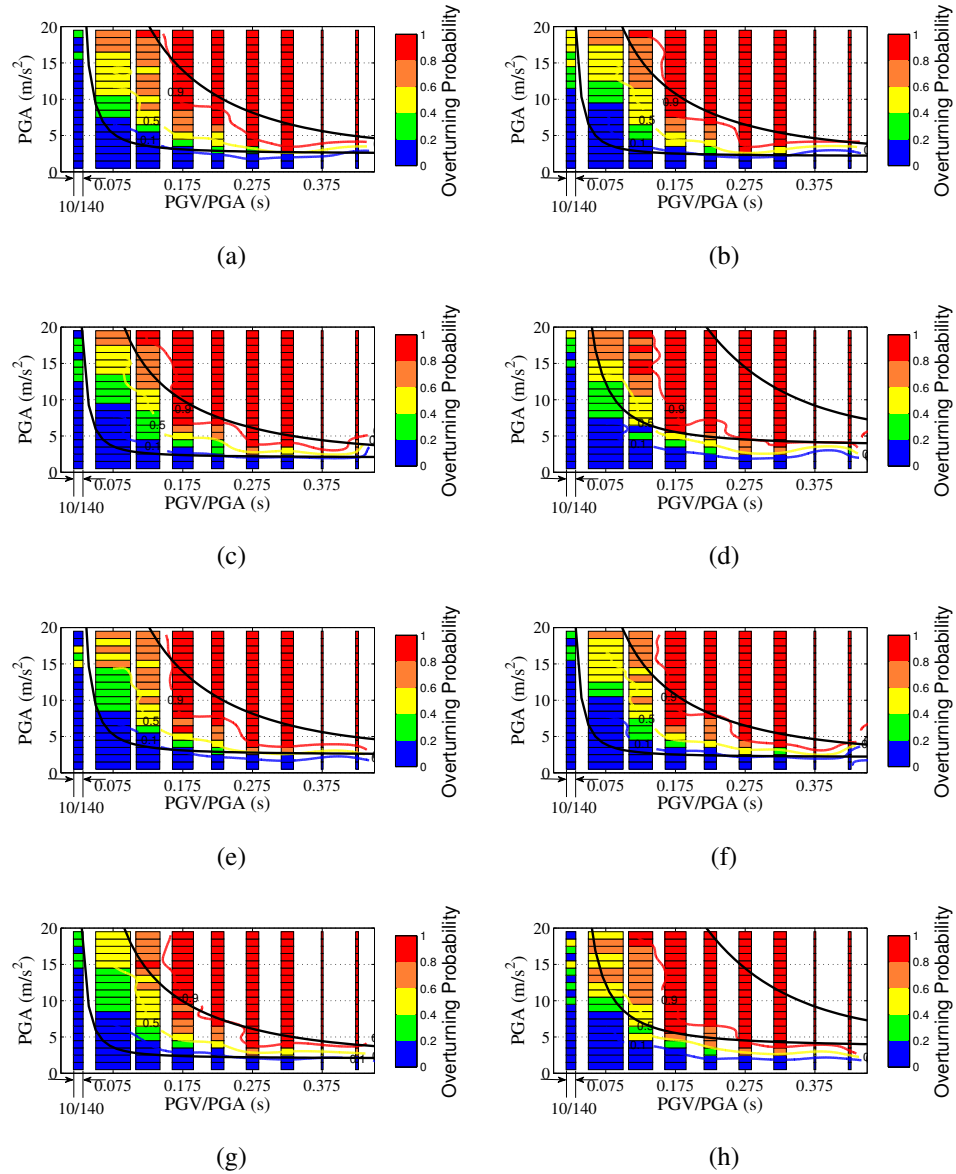


Figure 3.9: Overturning probability of the Echo Cliff PBR as a function of PGA and PGV/PGA under three-component pedestal excitation with the strong horizontal component oriented at (a) 0°, (b) 45°, (c) 90°, (d) 135°, (e) 180°, (f) 225°, (g) 270°, and (h) 315° counter-clockwise (CCW) to the X axis. The upper and lower black lines, predicted by Purvance et al.'s empirical relation, represent the PGA-PGV/PGA combinations corresponding to rock overturning probabilities of 1% and 99%, respectively.

Yet, several ground motion records with PGAs around 2.5 m/s² applied in the 135° direction appear to overturn the rock [Fig. 3.9(d)]. This may be attributed to the absence of strong directionality in the ground motion, causing rocking to initiate in other, perhaps more vulnerable, directions. The histogram of PGAs in the orthogonal horizontal and the

vertical directions for the 140 normalized records are shown in Figs. 3.10(a) and 3.10(b), respectively. A PGA bin width of 0.2 m/s^2 is used. These figures show that the orthogonal horizontal component is almost as intense as the strong ground motion component for half (70) of the earthquake records [Fig. 3.10(a)] and the vertical PGA is more than 0.6 m/s^2 for 65 of the earthquake records [Fig. 3.10(b)]. Figs. 3.11(a) and 3.11(b) show traces of the resultant horizontal ground acceleration at Lamont station from the 1999 Duzce earthquake and at the Cholame station from the 1966 Parkfield earthquake, respectively. These records belong to the set of 70 records whose resultant ground acceleration vectors have no preferred azimuthal direction and whose amplitudes at several azimuths are similar. In these 70 cases, the resultant horizontal PGA is likely to be appreciably larger than the component PGA and may exceed the quasi-static toppling acceleration in the resultant direction, initiating rocking motion in that direction. Alternately (or in concert with ground motion resultant), rocking may initiate in directions in which the rock may have a substantially lower quasi-static toppling acceleration.

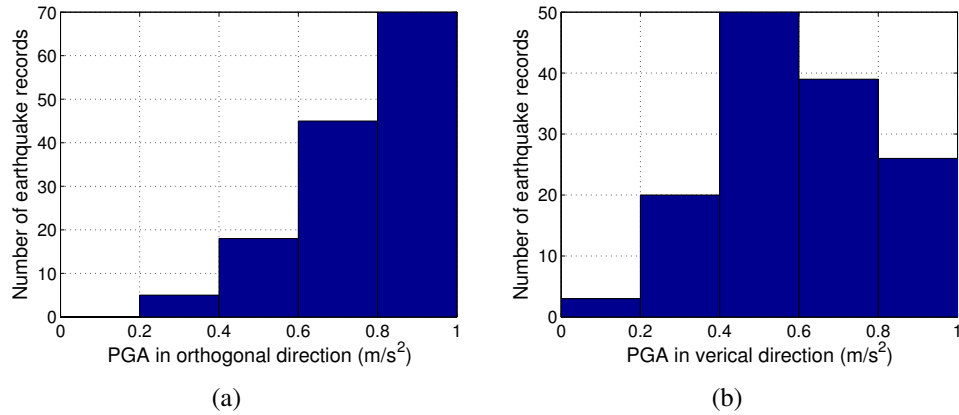


Figure 3.10: Histogram depicting the distribution of PGA of the (a) orthogonal horizontal ground motion component and (b) the vertical ground motion component of the 140 normalized earthquake records.

The absence of directionality in more than half the ground motion records results in little differences in the overturning fragility maps for the eight different ground motion orientations. Adding to that is the extra vulnerability of the rock in the overhang/pedestal-downsloping direction (135° CCW to the X axis), where gravity aids the earthquake excitation in toppling the rock. Fig. 3.12 shows the histogram of the toppling direction of

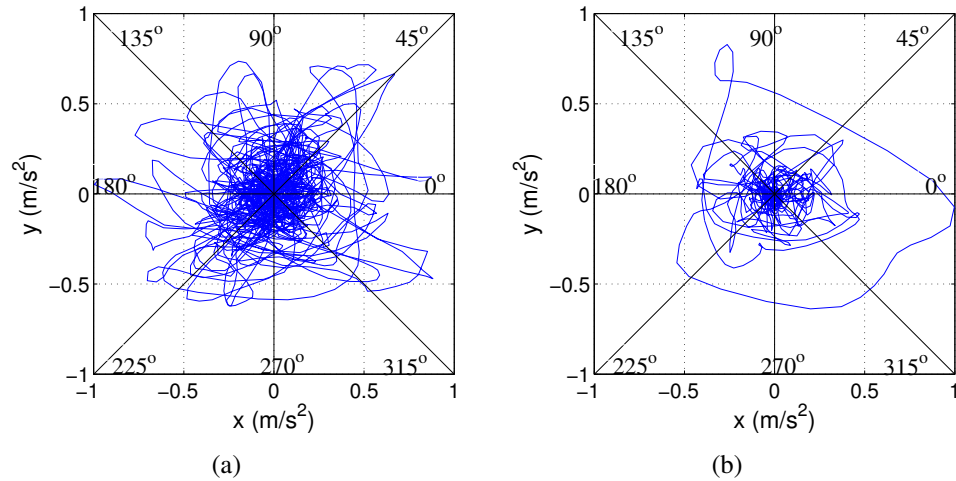


Figure 3.11: The traces of the resultant horizontal ground acceleration at (a) Lamont station from the 1999 Duzce earthquake and (b) Cholame station from the 1966 Parkfield earthquake.

the Echo Cliff PBR. The bins are of width 45° and are centered on 0° , 45° , and so on. The height of a bin corresponds to the fraction of analysis cases out of 21280 (140 records \times 19 scaling factors \times 8 orientations) where toppling occurs at the overturning angles corresponding to that bin. The rock model overturns between 122.5° and 157.5° in approximately 60% of the 21280 cases. Rocking could be initiated in any direction, but the rock finds it easiest to topple in the vicinity of the 135° CCW direction, thanks to the presence of the gradient and the overhang.

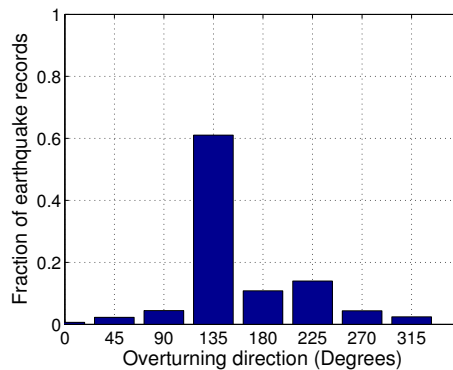


Figure 3.12: Histogram depicting the overturning direction of the Echo Cliff PBR. The height of a bin corresponds to the fraction of analysis cases out of 21280 where toppling occurs at the overturning angles corresponding to that bin.

The PGA required to overturn the rock decreases with increase in PGV/PGA [Fig. 3.9]. Purvance et al. [88] demonstrated that PGV/PGA correlates with the duration of the pre-

dominant acceleration pulse. It follows therefore that as the duration of the acceleration pulse increases, the amplitude required to overturn the rock decreases. To further compare the results from our simulation against those obtained from the empirical relation derived by Purvance et al. [88], we approximate the rock to a 2-D cross section balanced on a plane at two contact points [Fig. 3.13(a)]. These contact points are estimated from the intersection of the direction of excitation with the inner loop of the contact interface [Fig. 3.13(b)]. The input to the empirical equation are the mass of the rock (m), distance of the two contact points from the center of mass (R_1 and R_2), and the mass moment of inertia (I) of the rock about the center of mass in the direction perpendicular to the ground excitation. The mass and mass moment of inertia are taken from the 3-D rock model.

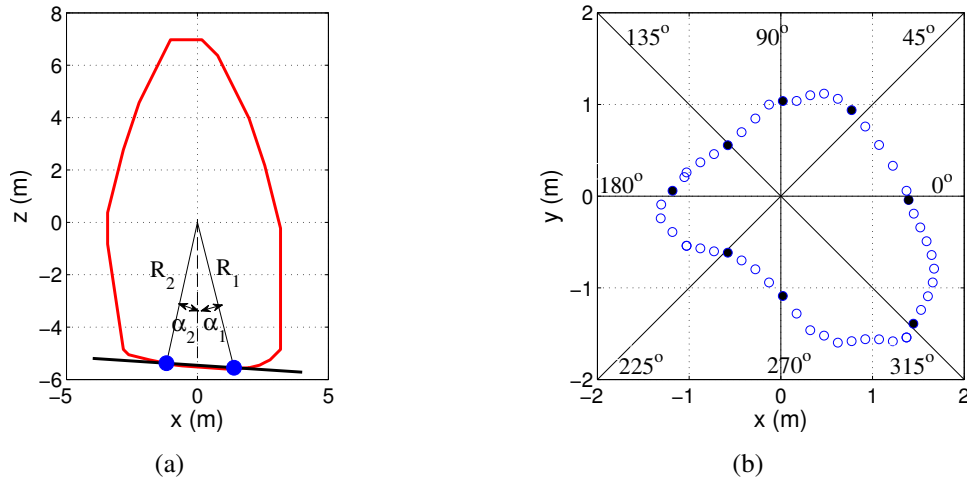


Figure 3.13: (a) 2-D approximation of the rock-pedestal system for excitation applied in the x direction and (b) contact points (black circles) for the 2-D model of the rock in different directions of excitation. The blue circles indicate the initial contact interface between the rock and the pedestal.

The black lines in each subfigure of Fig. 3.9 are the predictions by Purvance et al.'s empirical relation. The probability is 0.99 that PGA-PGV/PGA combinations above the upper line would overturn the Echo Cliff PBR, whereas the probability is 0.01 that PGA-PGV/PGA combinations above the lower line would overturn the rock. The empirical equation is able to predict the PGA-PGV/PGA combinations required for lower overturning probabilities well, but fails to accurately predict the PGA-PGV/PGA combinations required for higher overturning probabilities. In particular, the overturning probability is

significantly under-predicted for ground excitation oriented at 135° and 315° CCW to the X axis [Figs. 3.9(d) and 3.9(h)], the axis along which the pedestal gradient and the rock overhang are present. The errors of prediction by the empirical equation may be attributed to the rock's motion being constrained to the 2-D plane in the direction of strong ground excitation. That this is clearly not the case for this rock may be seen from an analysis of the rock subjected to a simple idealized sawtooth velocity pulse with PGV of 5 m/s and time period T of 3.5 s applied at 0° to the X axis (Fig. 3.14).

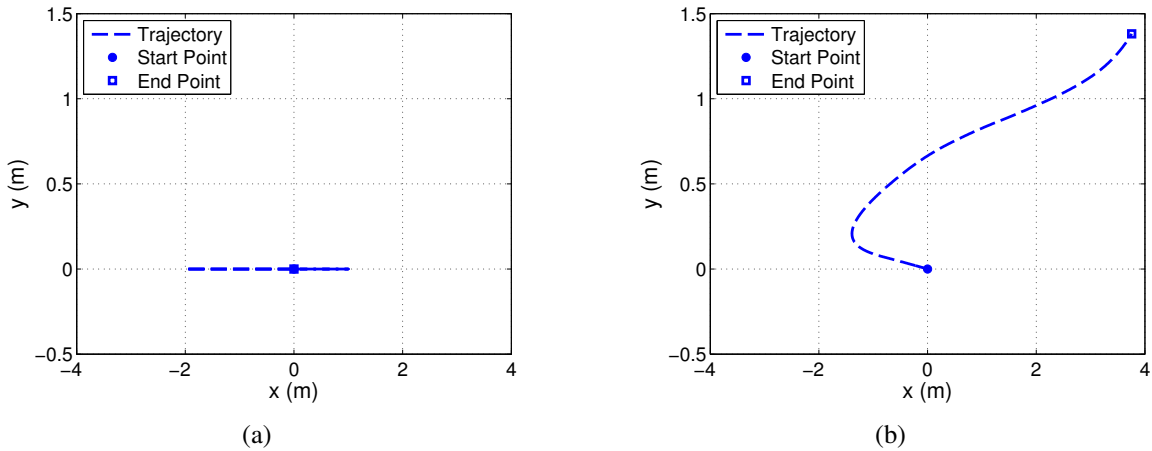


Figure 3.14: 2-D and 3-D rock models subjected to 1-cycle idealized sawtooth waveform excitation with $T = 3.5$ s and $PGV = 5$ m/s applied at 0° to the X axis. Trajectories of the center of mass projected on to the X-Y plane for (a) 2-D rock model with 2-point contact (rock does not topple) and (b) 3-D rock-pedestal model (rock topples).

The sensitivity of the overturning probability of the rock model to other ground motion parameters is explored by plotting it on the PGA-PGD [Fig. 3.15(a)] and the PGA-PGV [Fig. 3.15(b)] planes. Only the results corresponding to the strong component of the ground motion being oriented at 315° CCW to the X axis are presented here. The results corresponding to the other directions are qualitatively similar [refer to Appendix C for the full set of figures]. These figures are developed by binning the 140 scaled records at each PGA level into PGD bins of 0.25 m width [Fig. 3.15(a)] and PGV bins of 0.25 m/s width [Fig. 3.15(b)]. The overturning probability in each bin at each PGA level is the fraction of records (in that bin and that PGA level) that overturn the rock model. It should be noted that the PGA-PGD and PGA-PGV domains in Fig. 3.15 are not uniformly sampled by the 2660 scaled records. The sampling of different regions of the domain can be gauged by the

varying thickness of each column (at each PGA level). The thickness of the column at each PGA level in a given PGD or PGV bin is proportional to the fraction of points (out of 140) being sampled in that bin. It can be seen from the figures that the overturning probability is quite low for PGA, PGV, and PGD below 3 m/s^2 , 0.75 m/s , and 0.25 m , respectively. A small fraction of records with PGA in the range of $10\text{-}15 \text{ m/s}^2$ and PGV in the range of $0.25\text{-}0.5 \text{ m/s}$ are able to overturn the rock model [Fig. 3.15(b)]. Similarly, a small fraction of records in the PGA range of $13\text{-}15 \text{ m/s}^2$ and PGD lower than 0.25 m are able to overturn the rock model [Fig. 3.15(a)]. Also, the PGV required to overturn the rock increases gradually with PGA (follow the red bins with overturning probability in the range of $0.8\text{-}1.0$ in Fig. 3.15(b)). On the other hand, there is no discernible relation between the PGA and PGD required to overturn the rock model.

Figs. 3.15(a) and 3.15(b) do not provide sufficient information on the dependence of the overturning probability on ground motion parameters PGD and PGV. Therefore, a subset of 2046 of the 2660 scaled earthquake records with PGV less than 3 m/s and PGD less than 3 m are used for developing Fig. 3.16. This figure shows the overturning probability of the rock on the PGD-PGV plane. The 2046 records are divided into bins of width 0.25 m/s in PGV and 0.25 m in PGD. The overturning probability in each bin is the fraction of records (in that bin) that overturn the rock model. The varying thicknesses of the column are proportional to the fraction of earthquakes (out of 2046) that are sampled in a given PGV and PGD bin. Beyond a PGV of 0.5 m/s , the PGD required to overturn the rock model decreases with increase in PGV.

The overturning of the rock is likely to be affected by the duration of the strong shaking, defined as the length of the record (in seconds) within which 90% of the seismic energy is contained. Here, we use Anderson's energy integral formulation [8] to determine the duration of the 140 earthquake records. In this method the square of the velocity time history is integrated to arrive at the energy of the record. Figs. 3.17(a) and 3.17(b) show the overturning probability of the rock on the PGV-duration and PGA-duration planes, respectively. Fig. 3.17(a) is developed similar to Fig. 3.16 by dividing the scaled earthquake records with PGV less than 3 m/s into bins of width 0.25 m in PGV and 5 s in duration. Fig. 3.17(b) is developed similar to Fig. 3.9 by dividing the 140 earthquake records at each

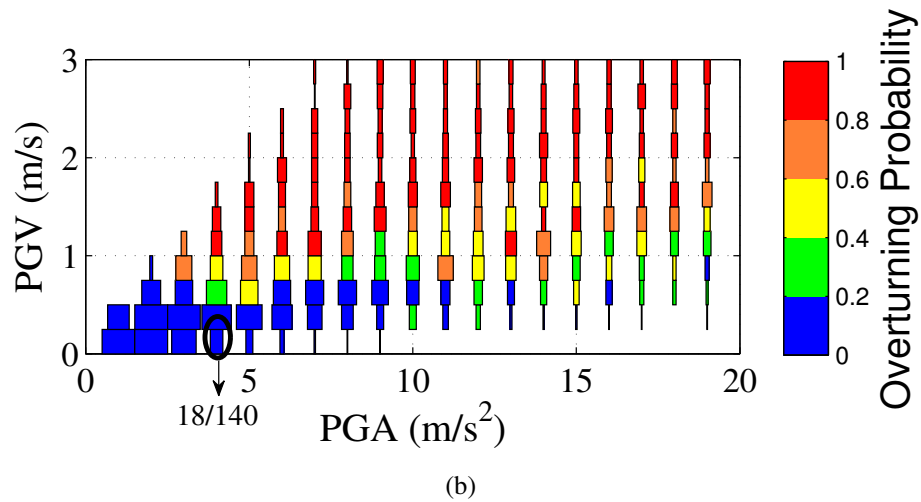
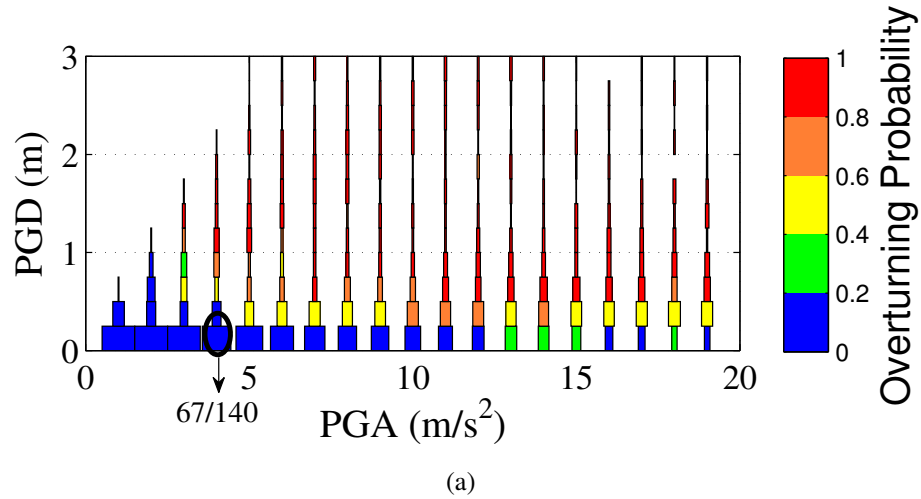


Figure 3.15: Overturning probability of the rock model as a function of (a) PGD and PGA, and (b) PGV and PGA. Each column in the figures contains the results from 140 earthquake records scaled to a specific PGA level. The varying thicknesses of the column are proportional to the fraction of earthquakes (out of 140) being sampled in a given PGD or PGV bin.

PGA level into bins of width 5 s in duration. Fig. 3.17(a) shows that the PGV required to overturn the rock model is more or less independent of the duration of the earthquake. However, the PGA required to overturn the rock model decreases more or less uniformly with duration with the exception of the first and last columns corresponding to duration bins 5-10 s and 45-50 s. A low PGA of 4 m/s^2 seems to suffice to overturn the rock under ground motions with duration between 5 s and 10 s, whereas a high PGA of 7 m/s^2 seems to be needed to overturn the rock under ground motions with longer durations of 45-50 s. This result is surprising. The tiny thickness of these end columns indicate that these regions

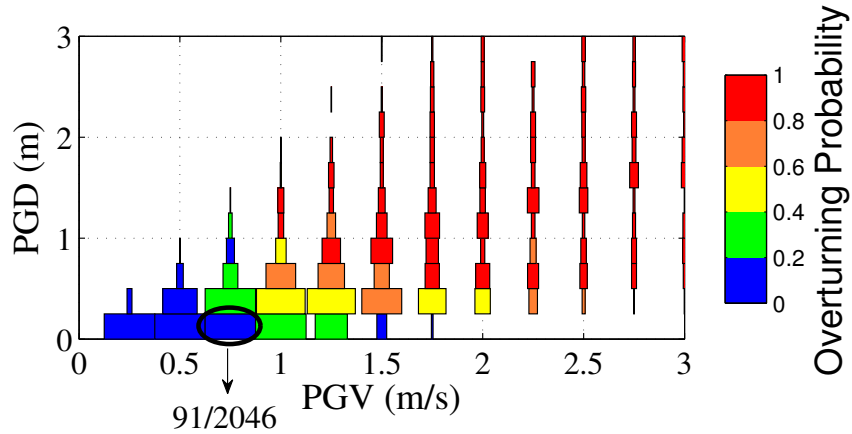


Figure 3.16: Overturning probability of the rock model as a function of PGD and PGV. 2046 out of the 2660 scaled earthquake records which have PGV and PGD less than 3 m/s and 3 m, respectively, are used to create this figure. The 2046 earthquakes are divided into bins of width 0.25 m/s in PGV and 0.25 m in PGD. The varying thicknesses of the column are proportional to the fraction of earthquakes (out of 2046) that are sampled in a given PGV and PGD bin.

of the PGA-duration plane are sampled poorly (very few of the records have durations in these ranges) and these outlier observations may not be reliable.

Next, we vary the rock-pedestal friction coefficients and compare the overturning probabilities of the rock. For this analysis, we orient the strong ground motion component at 315° CCW to the X axis to get the base of the rock moving in its most vulnerable direction (at 135° CCW to the X axis along the pedestal gradient and rock overhang). Here too, we assume the same coefficient for static and kinetic friction. We analyze the rock under the 2660 scaled records for friction coefficients (μ) of 0.6 and 0.8, and compare the results with that obtained earlier for $\mu = 1.0$. When the PBR is subjected to earthquake excitation, it can slide, rock, or exhibit sliding coupled with rocking. For a constant ground acceleration, the response mode of the rock shifts from pure sliding to sliding coupled with rocking and then to pure rocking with increase in the coefficient of friction. For a rigid rectangular block placed on a rigid horizontal ground, Shenton [95] obtained the relation between the constant horizontal ground acceleration and the coefficient of friction required to initiate rocking, sliding, and coupled rocking-sliding of the block. He observed that for a ground excitation amplitude greater than the quasi-static toppling acceleration of the block, it can undergo pure sliding only for friction coefficients below its width to height

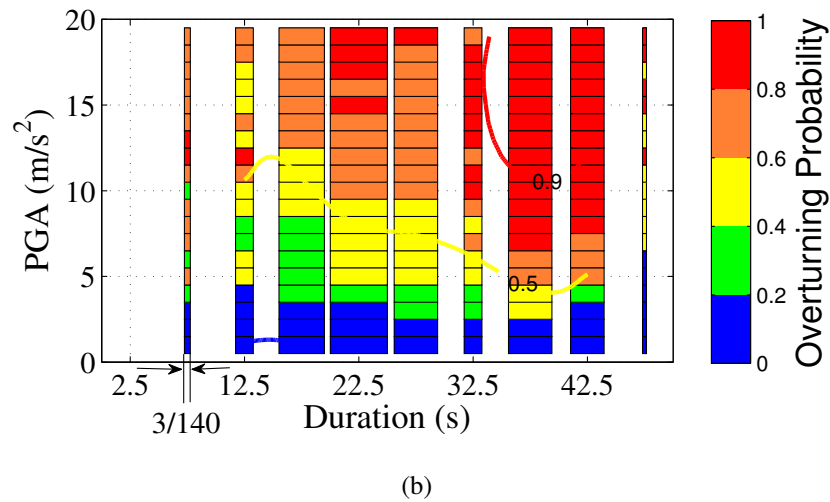
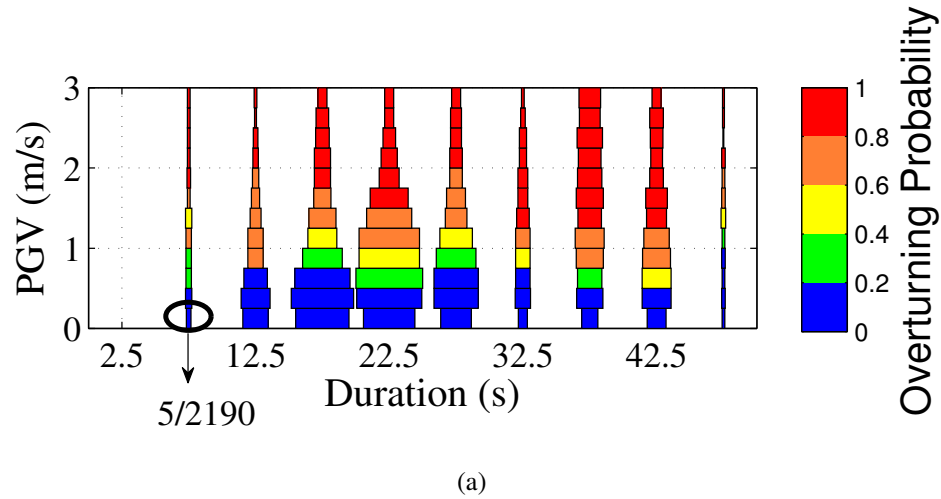


Figure 3.17: Overturning probability of the rock model as a function of (a) PGV and duration, and (b) PGA and duration. 2190 out of the 2660 scaled earthquake records with PGV less than 3 m/s and duration less than 50 s are used for (a). The 2190 earthquakes are divided into bins of width 0.25 m/s in PGV and 5 s in duration. The varying thicknesses of the column are proportional to the fraction of earthquakes (out of 2190) that are sampled in a given PGV and duration bin. Each column in the (b) contains 140 earthquake records scaled to a specific PGA level. The varying thicknesses of the column are proportional to the fraction of earthquakes (out of 140) being sampled in a given duration bin.

ratio. This observation, when applied to the 2-D cross-section of the PBR at 135° [similar to Fig. 3.13(a)] shows that the rock can undergo pure sliding only if μ is less than 0.15. Though the gradual pedestal-gradient is not considered in this simple calculation, it can be shown that the transition from sliding to sliding coupled with rocking will occur at even lower values of friction coefficient when the gradient in contact interface is included.

Therefore, for the range of friction coefficients observed in rocks (0.6-1.0), the PBR will undergo either rocking or sliding coupled with rocking under earthquake excitation.

If the rock were to exhibit only sliding, the relative displacement of the contact points, i.e., points belonging to the inner loop in Fig. 3.2(f), with respect to the pedestal can be used as a measure of the sliding displacement. However, rocking in 3-D can also affect the relative displacements of the contact points with respect to the pedestal. Therefore, the effect of sliding cannot be isolated when the rock exhibits sliding coupled with rocking. Moreover, the alignment of the preferred overturning direction (direction of the overhang) of the rock with the preferred sliding direction (gradient of the contact interface) makes it harder to judge the contribution of sliding to the toppling of the rock model on a case by case basis. However, comparison of the overturning probability of the rock model in the PGD-PGA, PGV-PGA, and PGD-PGV planes for different friction coefficients provide qualitative insights into the effect of sliding on the overturning of the rock model [Figs. 3.18(a) and 3.18(b)].

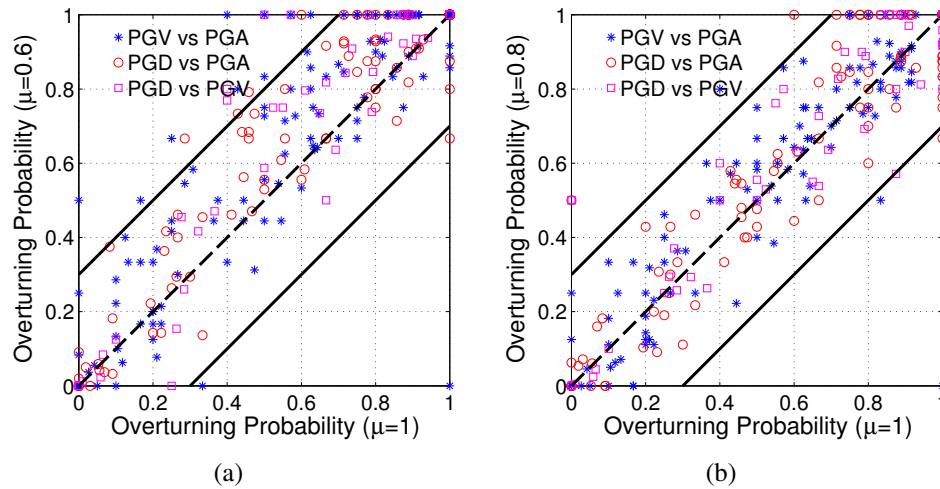


Figure 3.18: Comparison of overturning probability of the Echo Cliff PBR taken from the PGD-PGA, PGV-PGA, and PGD-PGV planes for (a) $\mu = 0.6$ and (b) $\mu = 0.8$ against that for $\mu = 1.0$. Each data point is a direct comparison between the overturning probability of a PGV bin at a given PGA level (blue asterisk), PGD bin at a given PGA level (red circle), and PGD bin at a given PGV range (magenta square) for $\mu = 0.6$ and $\mu = 0.8$ against $\mu = 1.0$. Most of the data points are contained within the solid black lines, which indicate that the overturning probability for $\mu = 0.6$ and $\mu = 0.8$ are within 0.3 of that for $\mu = 1.0$.

The overturning probability from each cell of Figs. 3.15(a), 3.15(b), and 3.16 for $m\mu =$

1.0 is compared against that for the same cell in the corresponding figures developed for $\mu = 0.6$ [Fig. 3.18(a)] and for $\mu = 0.8$ [Fig. 3.18(b)]. Blue asterisks correspond to overturning probabilities taken from the PGV-PGA plane, red circles from the PGD-PGA plane, and magenta squares from the PGD-PGV plane. If the response of the rock was independent of the coefficient of friction, all points would lie on the dashed black diagonal line. The following observations can be made: (i) friction does play a role in the response of the rock; (ii) a lower friction coefficient results in higher probability of overturning (most points on Fig. 3.18(a) and a large majority of the points in Fig. 3.18(b) lie above the dashed diagonal line); clearly, sliding makes the rock more susceptible to toppling over the cliff. (iii) In general, the overturning probabilities for $\mu = 0.6$ and $\mu = 0.8$ are within ± 0.3 of those for $\mu = 1.0$ (indicated by the solid black bounding lines in these figures).

All the analyses so far were conducted using 3-component ground motion. To understand the effect of vertical ground motion on the overturning probability of the rock, we analyze the rock model under just the horizontal ground motion components with the strong component oriented at 315° CCW to the X axis. A friction coefficient of 1.0 is used for this analysis. As for the friction study, the overturning probabilities of the rock taken from the PGD-PGA, PGV-PGA, and PGD-PGV planes under 3-component ground motion are plotted against the corresponding probabilities under 2-component ground motion (without the vertical component) in Fig. 3.19. Once again, if the response of the rock was independent of the vertical ground motion, all points would lie on the dashed black diagonal line. The fact that they are scattered off the diagonal indicates that vertical ground motion does play a role in the rocking-sliding response. However, the fact that they are secularly scattered on either side of the diagonal indicates that vertical ground motion may aid or impede the overturning of the rock. The overturning probabilities under 2-component ground motion (without the vertical component) are well within 0.3 of those under 3-component ground motion.

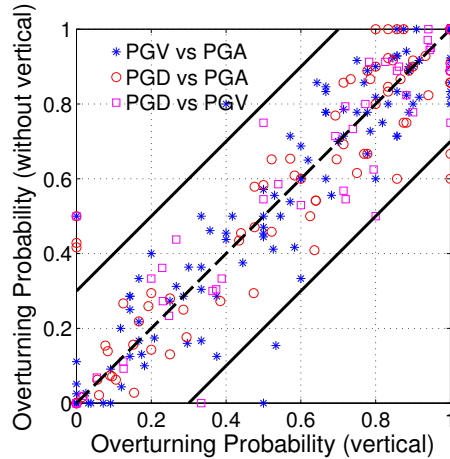


Figure 3.19: Comparison of overturning probability of the Echo Cliff PBR taken from the PGD-PGA, PGV-PGA, and PGD-PGV planes under 3-component ground motion are plotted against the corresponding probabilities under 2-component ground motion (without the vertical component). Each data point is a direct comparison of the overturning probability of a PGV bin at a given PGA level (blue asterisk), PGD bin at a given PGA level (red circle) and PGD bin at a given PGV range (magenta square) from the analysis using 3-component ground motion against that using 2-component ground motion. Most of the data points are contained within the solid black lines, which indicate that the overturning probabilities under 2-component ground excitation are within 0.3 of that under 3-component ground motion.

3.5.1 Applications of fragility maps

The overturning fragility maps generated for the Echo Cliff PBR may be used to check the ground motions predicted for this location (i) by the USGS seismic hazard maps and (ii) by scenario earthquake simulations. Before using the fragility maps for such applications, we first assess whether they can accurately predict the overturning probability of the rock under other recent earthquakes. So, we analyze the rock-pedestal system under ground motions recorded during the 2011 Christchurch earthquake at 20 stations located less than 20 km from the rupture [22]. Of the 20 ground motions considered, 10 records overturn the rock [black asterisks in Fig. 3.20] and the rock does not overturn for the other 10 records [black squares in Fig. 3.20]. A comparison between the overturning probability of the rock (as a function of PGA and PGV/PGA) obtained from the fragility maps with the binary overturning results of the rock obtained from the simulations is presented in Fig. 3.20. For 16 (out of 20) records, the results from the simulations are in good agreement with the fragility maps. The records that overturned the rock have overturning probability in the

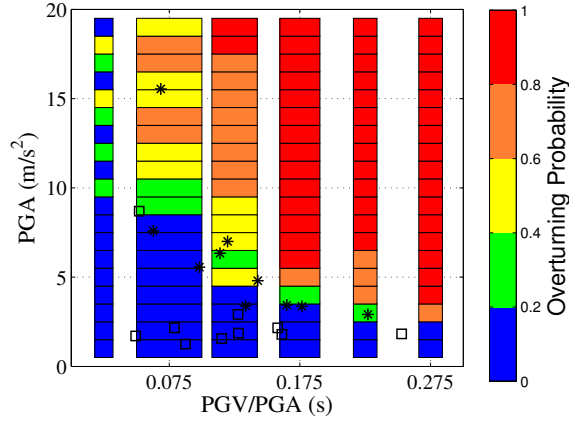


Figure 3.20: Comparison between the results obtained from the rigid body dynamics simulation of the rock under ground motions from 2011 Christchurch earthquake with the overturning probability of the rock as a function of PGA and PGV/PGA obtained from the fragility maps generated earlier. The black asterisks in the figure represent the PGA and PGV/PGA of the 10 ground motion records for which the rock overturned in the simulation. The black squares represent the PGA and PGV/PGA of the ground motion records for which the rock did not overturn.

0.2-0.6 range and the records that did not overturn the rock have overturning probability below 0.2. For three records that overturned the rock, the overturning probability is below 0.2. The overturning probability is in the 0.2-0.4 range for one record that did not overturn the rock. However, this disagreement occurs only very close to the transition region from overturning probability of 0-0.2 to 0.2-0.4.

The 2008 USGS hazard maps [86] specify a PGA of 6.9 m/s^2 and an S_a^{1s} (the 5% damped spectral acceleration at 1 s period) of 5.16 m/s^2 for the Echo Cliff PBR location at the hazard level of 2% probability of exceedance in 50 years (or an earthquake with a 2475-year return period). Because PGV and S_a^{1s} are correlated, the Newmark-Hall relationship [$S_a(1) = 1.056PGV$] may be used to obtain a PGV of 4.89 m/s. The corresponding PGV/PGA works out to 0.7 s. By extrapolating the results from Fig. 3.9 to higher PGV/PGA values, it can be seen that the rock will overturn for this PGA and PGV/PGA combination. Therefore, the seismic hazard at this location may be over-predicted by the USGS hazard maps. Design of buildings based on this level of shaking may be conservative and not cost-effective. We should point out that the findings from this study for this rock site cannot be extended to basin or soil sites.

Because the Echo Cliff PBR is located near the San Andreas fault, it can also be used



Figure 3.21: An image of the Pacifico rock taken by Dr. Jim Brune and Dr. Richard Brune.

to check if the synthetic ground motion at this site from the Southern California ShakeOut scenario violates the existence of the rock. The simulated ShakeOut scenario earthquake, used in the Great California ShakeOut Exercise and Drill, is a M_w 7.80 rupture, initiating at Bombay Beach and propagating northwest through the San Geronio pass, terminating 304 km away at Lake Hughes in the north. Using a source developed by Hudnut et al. [53] and the SCEC-CVM wave-speed model [67, 77, 78], Graves et al. [43] simulated 3-component long-period ground motion waveforms in the greater Los Angeles region. The broadband version of the ground motion at the Echo Cliff PBR location was obtained from Robert W. Graves (personal communication). The PGA, PGV, and PGD of this record are 0.32 m/s^2 , 0.07 m/s , and 0.2 m , respectively. As can be seen from Figs. 3.15(a), 3.15(b), and 3.16, the rock will not overturn for this level of ground motion. Therefore, the synthetic ground motion from the shakeout scenario does not violate the existence of the Echo Cliff PBR at this location.

3.6 Pacifico Rock

Pacifico rock [Fig. 3.21] is one of the precariously balanced rocks identified by Brune which is located approximately 12 km from the San Andreas Fault [92]. The proximity of this rock to the San Andreas Fault and the time period for which the rock has been present in this precarious configuration (approximately 12,000 years [15]) suggest that this PBR may provide an independent constraint on the historic peak ground motion experienced by this region, and, by extension the future ground shaking in this region.

Purvance et al. [92] estimated the overturning probability of this rock as function of PGA and PGV/PGA using the empirical expression derived by Purvance et al. [88]. For this study, they approximated the rock to a 2-D block with 2 contact points (without using inputs from tilt tests) and the resulting parameters of the equivalent 2-D rectangular block are then used as input to the empirical expression. As discussed in Section 3.4, the empirical equation under-predicts the overturning probability of the rock when the parameters for the 2-D block are not corrected using tilt tests. Therefore, the fragility estimates of the rock obtained from this analysis may not be accurate. Here, we conduct 3-D dynamic analysis on the rock-pedestal system to arrive at accurate fragility estimates for the rock and use it as an independent test for the seismic hazard maps and synthetic ground motion simulations rupturing parts of the San Andreas Fault.

3.6.1 Toppling analysis of Pacifico rock

Dr. Jim Brune and Dr. Richard Brune combined multi-angle images of the rock and pedestal using PhotoModeler to arrive at the 3-D point cloud describing the geometry of the rock and the pedestal. Here, we use this point cloud to estimate the physical properties of the rock and to construct the 3-D rock surface and pedestal surface as detailed in Section 3.2. The 3-D geometric model of the rock and its pedestal [orthogonal view from what is presented in Fig. 3.21] and initial contact interface between the two are shown in Figs. 3.22(a) and 3.22(b), respectively. The initial contact interface Fig. 3.22(b) indicates that the rock is very slender in one direction (along the X axis). Therefore, the rock is most likely to exhibit rocking response in the X-Z plane. The rock is resting on a downward sloping (with a gradient of about 8°) pedestal oriented along 135° in the counter clockwise direction (CCW) from the X axis. For high friction coefficients of 1.0 between the rock the pedestal, the rock is not expected to slide. However, for lower friction coefficients of 0.6 or 0.8, the rock may exhibit sliding coupled with rocking.

We first assume the friction coefficient between the rock and pedestal to be 1.0 and estimate the ground motion parameters required to overturn the rock. For this analysis, we use the same 140 earthquake records as in Section 3.5. These ground motions are first

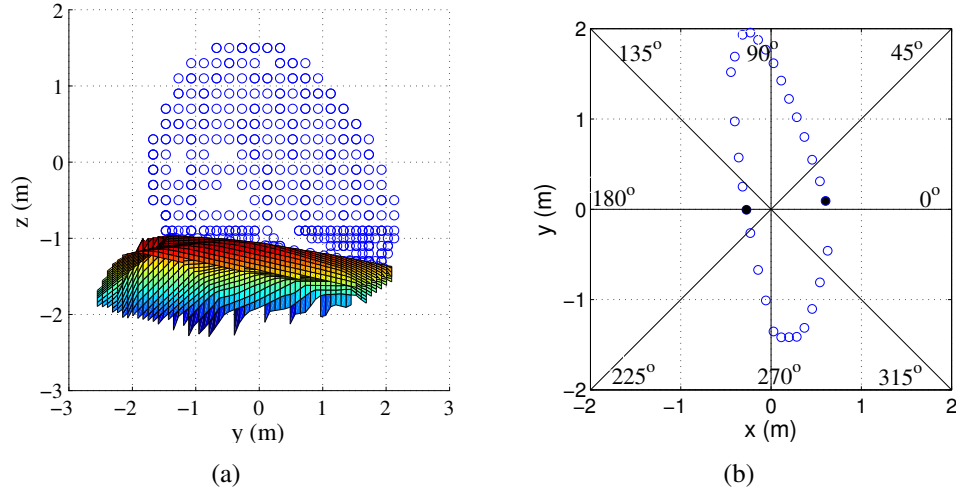


Figure 3.22: (a) 3-D model of the rock-pedestal system and (b) initial contact interface between the rock and its pedestal. The black circles indicate the contact points used to compare the results with Purvance's empirical equation.

normalized such that the PGA of the dominant strong ground motion component is 1 m/s^2 and then scaled from PGA of 1 m/s^2 to 20 m/s^2 in steps of 1 m/s^2 . As the PBR is most sensitive to rocking motion along the X axis, we consider two cases in which the strong ground motion component is applied to the pedestal at: (i) 0° CCW from the X axis and (ii) 180° CCW from the X axis. Note that the pedestal accelerating in the 0° direction will invoke the rock to respond in the opposite direction, i.e., at 180° . The overturning probability of the rock as a function of PGA and PGV/PGA is shown in Fig. 3.23 for the two different directions of ground excitation. These plots are developed similar to Fig. 3.9 by binning the 140 scaled records at each PGA level into PGV/PGA bins of 0.05 s width. The colored contour lines correspond to overturning probabilities of 0.1, 0.5, and 0.9.

As can be seen from Fig. 3.23, the overturning probability of the rock is very low for PGA less than 4 m/s^2 . It can also be seen from these figures that the PGA required to overturn the rock increases with decrease in PGV/PGA and that the results for ground excitation applied at 0° and 180° are qualitatively similar. A similar trend was also observed in the Echo Cliff PBR [Fig. 3.9].

In order to compare the results from our simulation with those obtained from the empirical relation derived by Purvance et al. [88], we approximate the rock to a 2-D cross section balanced on a plane at two contact points as we did for the case of the Echo Cliff PBR. The

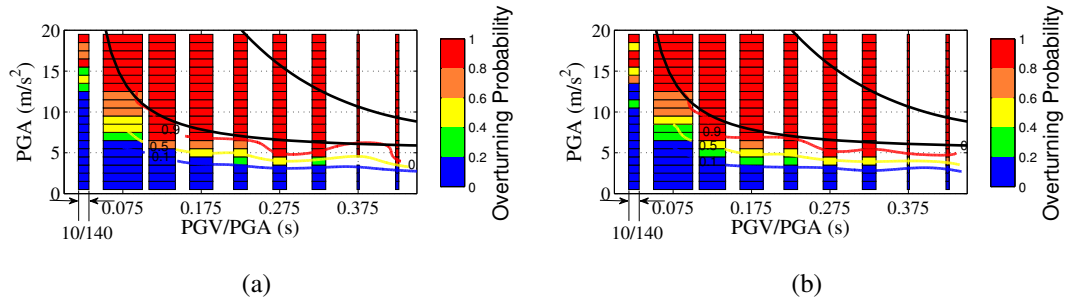


Figure 3.23: Overturning probability of the Pacifico rock as a function of PGA and PGV/PGA under three-component pedestal excitation with the strong horizontal component oriented at (a) 0° and (b) 180° counter-clockwise (CCW) to the X axis. The upper and lower black lines, predicted by Purvance et al.'s empirical relation, represent the PGA-PGV/PGA combinations corresponding to rock overturning probabilities of 1% and 99%, respectively.

black lines in each subfigure of Fig. 3.23 are the predictions by Purvance et al.'s empirical relation. The probability is 0.99 that PGA-PGV/PGA combinations above the upper line would overturn the Echo Cliff PBR, whereas the probability is 0.01 that PGA-PGV/PGA combinations above the lower line would overturn the rock. It can be seen that the empirical equation over-predicts the PGA-PGV/PGA combination required for the rock to overturn even for this fairly simple rock, whose rocking response is more or less contained within the X-Z plane.

To explore the dependence of the overturning probability of the rock model to other ground motion parameters, the overturning probability on the PGA-PGD and the PGA-PGV planes are shown in Figs. 3.24(a) and 3.24(b), respectively. Note that only the figures corresponding to strong component ground motion applied to the pedestal at 0° are presented here. Figs. 3.24(a) and 3.24(b) are developed similar to Figs. 3.15(a) and 3.15(b) by binning the 140 scaled records at each PGA level into PGD bins of 0.25 m width [for Figs. 3.24(a)] and PGV bins of 0.25 m/s width [for Fig. 3.24(b)]. It can be seen from Figs. 3.24(a) and 3.24(b) that the overturning probability is quite low for PGA and PGV below 4 m/s^2 and 0.5 m/s, respectively. A small fraction of records with PGA of 13 m/s^2 and PGV in the range of 0.25-0.5 m/s are able to overturn the rock model [Fig. 3.24(b)]. Unlike PGA and PGV, even small PGDs less than 0.25 m are able to overturn the rock [Fig. 3.24(a)]. In contrast to the observations made for the Echo Cliff PBR [Fig. 3.15(b)], the PGV required to overturn the rock initially decreases with increase in PGA until 8 m/s^2

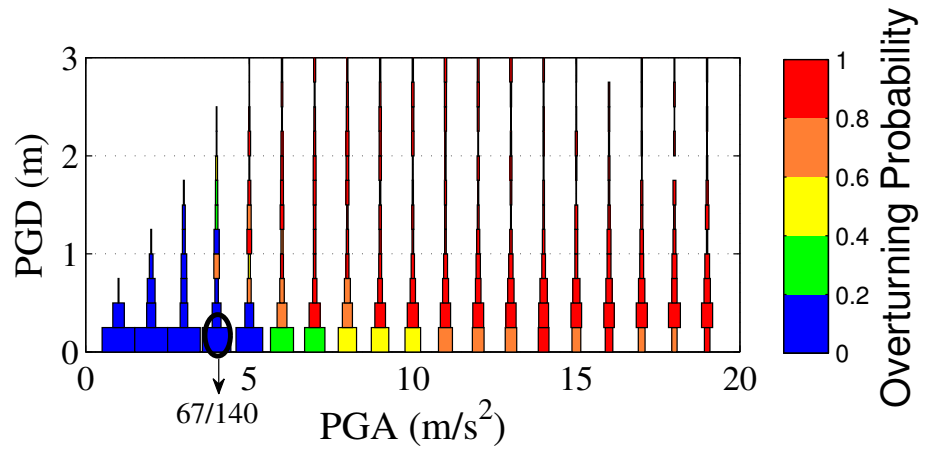
after which it is more or less independent of PGA [Fig. 3.24(b)].

Fig. 3.24(a) and 3.24(b) do not provide sufficient information on the dependence of the overturning probability on ground motion parameters PGD and PGV. Therefore, a subset of the 2660 scaled records with PGV less than 3 m/s and PGD less than 3 m are used for developing Fig. 3.25, which shows the overturning probability of the rock in the PGD-PGV plane. Beyond a PGV of 0.5 m/s, the PGD required to overturn the rock model decreases with increase in PGV. A similar trend was seen in the case of the Echo Cliff PBR [Fig. 3.16].

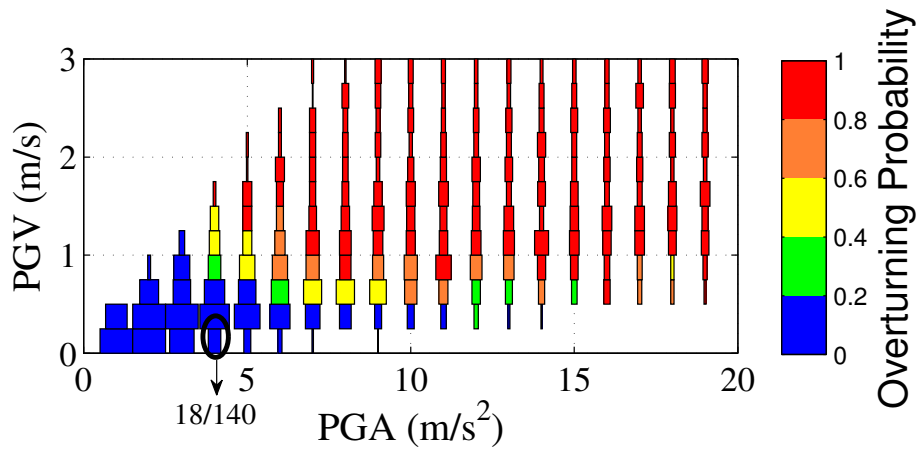
Next, we explore the dependence of overturning probability on ground motion duration. The ground motion duration is calculated as given in Section 3.5 using Anderson's energy integral formulation [8]. Figs. 3.26(a) and 3.26(b) show the overturning probability in the PGV-duration and PGA-duration planes, respectively. As in the case of the Echo Cliff PBR [Figs. 3.17(a) and 3.17(b)], the PGV required to overturn the rock model is more or less independent of the duration of the earthquake. However, the PGA required to overturn the rock model decreases more or less uniformly with duration.

Next, we vary the rock-pedestal friction coefficients and compare the overturning probabilities of the rock. For this analysis, we apply the strong ground motion component to the pedestal along 0° . We analyze the rock under the 2660 scaled records for static and kinetic friction coefficient (μ) of 0.6 and 0.8 and compare the results with that obtained earlier for $\mu = 1.0$. As explained in Section 3.5, the contribution of sliding to the overturning of the rock cannot be isolated. However, comparison of the overturning probability of the rock model in the PGD-PGA, PGV-PGA, and PGD-PGV planes for different friction coefficients provides qualitative insights into the effect of sliding on the overturning of the rock model [Figs. 3.27(a) and 3.27(b)].

The overturning probability from each cell of Figs. 3.24(a), 3.24(b) and 3.25 for $\mu = 1.0$ is compared against that for the same cell in the corresponding figures developed for $\mu = 0.6$ [Fig. 3.27(a)] and for $\mu = 0.8$ [Fig. 3.27(b)]. The following observations can be made from these figures: (i) friction does play a role in the response of the rock, (ii) a lower friction coefficient results in higher probability of overturning (most points on Fig. 3.27(a) and a large majority of the points in Fig. 3.27(b) lie above the dashed diagonal line), (iii) while the overturning probabilities for $\mu = 0.8$ are more or less within ± 0.3 of those for



(a)



(b)

Figure 3.24: Overturning probability of the rock model as a function of (a) PGD and PGA, and (b) PGV and PGA. Each column in the figures contain 140 earthquake records scaled to a specific PGA level. The varying thicknesses of the column are proportional to the fraction of earthquakes (out of 140) being sampled in a given PGD or PGV bin.

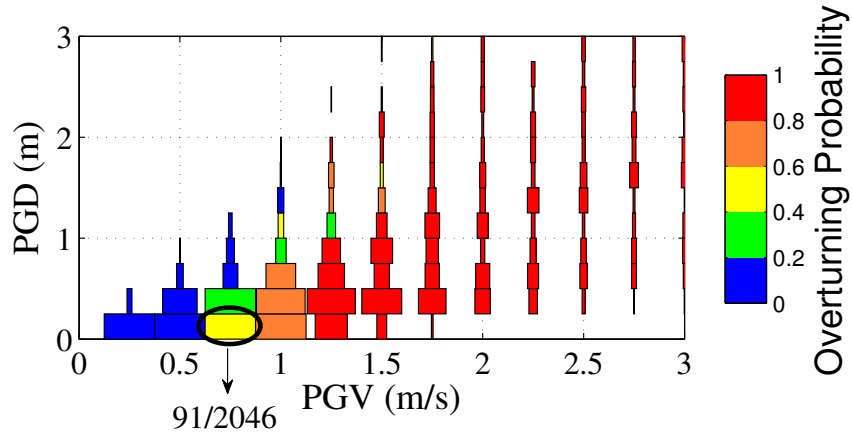


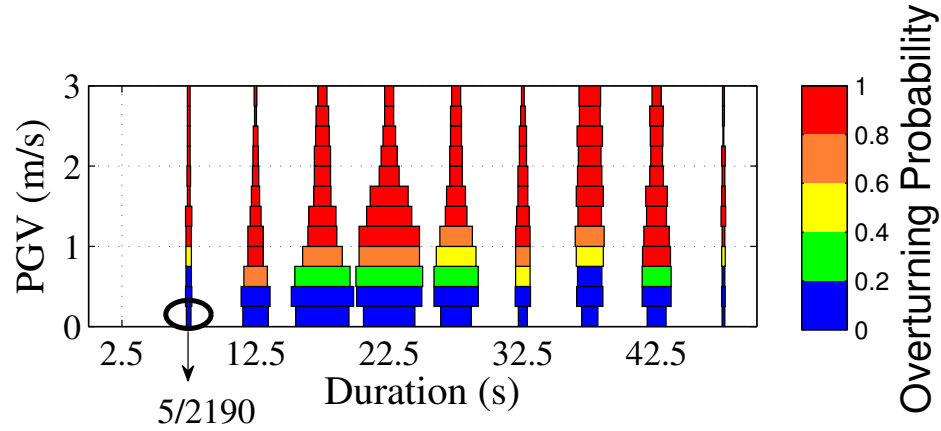
Figure 3.25: Overturning probability of the train model as a function of PGD and PGV. 2046 out of the 2660 scaled earthquake records which have PGV and PGD less than 3 m/s and 3 m, respectively, are used to create this figure. The 2046 earthquakes are divided into bins of width 0.25 m/s in PGV and 0.25 m in PGD. The varying thicknesses of the column are proportional to the fraction of earthquakes (out of 2046) that are sampled in a given PGV and PGD bin.

$\mu = 1.0$ (indicated by the solid black bounding lines in these figures), the overturning probabilities for $\mu = 0.6$ are much higher than those for $\mu = 1.0$ (indicated by the scatter of data points along the $y = 1$ line). Sliding plays a bigger role in overturning the Pacifico rock as compared to the Echo Cliff PBR. This may be attributed to higher gradient in the Pacifico rock-pedestal interface as compared to that of the Echo Cliff PBR.

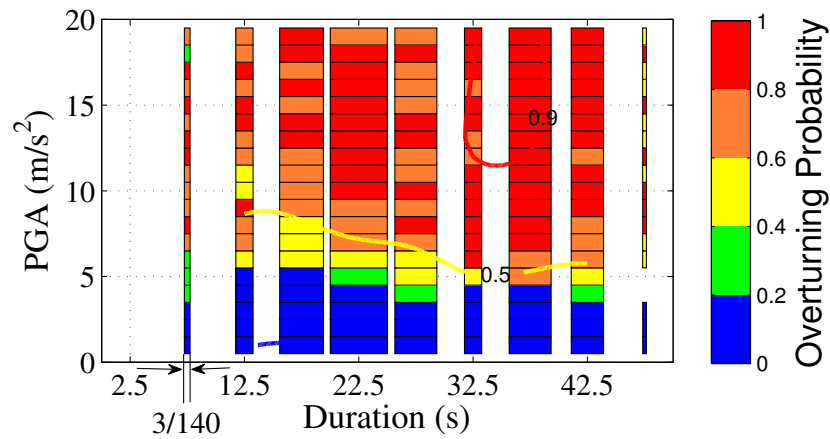
To test the effect of vertical ground motion on the overturning of the Pacifico PBR, the overturning probabilities of the rock taken from the PGD-PGA, PGV-PGA, and PGD-PGV planes under 3-component ground motion are plotted against the corresponding probabilities under 2-component ground motion (without the vertical component) in Fig. 3.28. As in the case of the Echo Cliff PBR, the points are secularly scattered on either side of the diagonal indicating that vertical ground motion may aid or impede the overturning of the rock.

3.6.2 Comparison with PSHA

As seen from Figs. 3.24(a), 3.24(b), and 3.25, the overturning probability of the rock depends on multiple ground motion parameters, mainly a combination of PGV and PGA. It cannot be characterized by a single ground motion intensity measure like PGA or PGV.



(a)



(b)

Figure 3.26: Overturning probability of the rock model as a function of (a) PGV and duration, and (b) PGA and duration. 2190 out of the 2660 scaled earthquake records which have PGV less than 3 m/s and duration less than 50 s are used for figure [(a)]. The 2190 earthquakes are divided into bins of width 0.25 m/s in PGV and 5 s in duration. The varying thicknesses of the column are proportional to the fraction of earthquakes (out of 2190) that are sampled in a given PGV and duration bin. Each column in the figures [(b)] contain 140 earthquake records scaled to a specific PGA level. The varying thicknesses of the column are proportional to the fraction of earthquakes (out of 140) being sampled in a given duration bin.

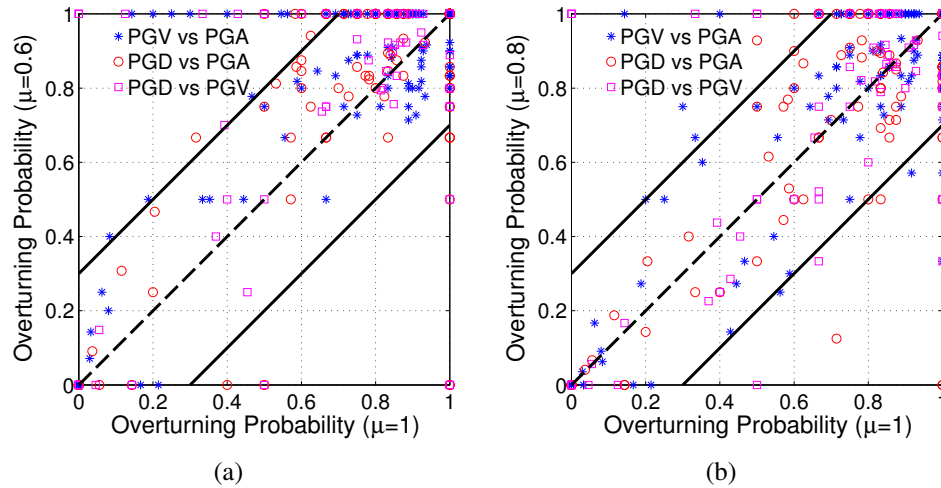


Figure 3.27: Comparison of overturning probability of the Echo Cliff PBR taken from the PGD-PGA, PGV-PGA, and PGD-PGV planes for (a) $\mu = 0.6$ and (b) $\mu = 0.8$ against that for $\mu = 1.0$. Each data point is a direct comparison between the overturning probability of a PGV bin at a given PGA level (blue asterisk), PGD bin at a given PGA level (red circle) and PGD bin at a given PGV range (magenta square) for $\mu = 0.6$ and $\mu = 0.8$ against $\mu = 1.0$. Most of the data points are contained within the solid black lines, which indicate that the overturning probability for $\mu = 0.6$ and $\mu = 0.8$ are within 0.3 of that for $\mu = 1.0$.

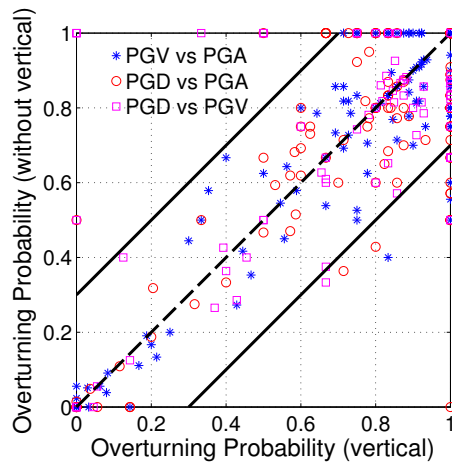


Figure 3.28: Comparison of overturning probability of the Pacifico PBR taken from the PGD-PGA, PGV-PGA, and PGD-PGV planes under 3-component ground motion are plotted against the corresponding probabilities under 2-component ground motion (without the vertical component). Each data point is a direct comparison of the overturning probability of a PGV bin at a given PGA level (blue asterisk), PGD bin at a given PGA level (red circle) and PGD bin at a given PGV range (magenta square) from the analysis using 3-component ground motion against that using 2-component ground motion. Most of the data points are contained within the solid black lines, which indicate that the overturning probabilities under 2-component ground excitation are within 0.3 of that under 3-component ground motion.

The national seismic hazard maps only provide the rate of occurrence of one ground motion intensity measure and do not provide the joint rate of occurrence of two ground motion intensity measures. Vector-valued probabilistic seismic analysis (VPSHA), which gives the joint rate of occurrence of two or more ground motion intensity measures [14], can be used to circumvent this problem.

In order to assess the overturning of the PBR when exposed to numerous earthquakes in an earthquake rupture forecast (ERF), Purvance et al. [92] estimated the simultaneous occurrence rates of ground intensity measures PGA and PGV for all earthquakes in the ERF that have occurred during the age of the PBR using the VPSHA method [14]. This method assumes that the PGA and PGV are log-normally distributed about the median value given by ground motion prediction equations (GMPEs) like the Campbell-Bozorgnia NGA ground motion model [28]. Then, for a forecast earthquake scenario with magnitude M_w recorded at a site R km from the rupture (Boore-Joyner distance) with site conditions S , the joint probability density function of PGA and PGV is given by:

$$f(PGA, PGV|M_w, R, S) = f(PGA|M_w, R, S)f(PGV|PGA, M_w, R, S) \quad (3.1)$$

Here, $f(PGA|M_w, R, S)$ is the probability density function (pdf) of PGA conditional on M_w and R and site conditions S and is given by:

$$f(PGA|M_w, R, S) = \frac{1}{PGA \sigma_{\ln PGA|M_w, R, S}} \phi \left(\frac{\ln PGA - \mu_{\ln PGA|M_w, R, S}}{\sigma_{\ln PGA|M_w, R, S}} \right)$$

Here, $\phi(x)$ is the standard Gaussian pdf with zero mean and standard deviation of 1. $\mu_{\ln PGA|M_w, R, S}$ and $\sigma_{\ln PGA|M_w, R, S}$ are the mean and standard deviation of \ln PGA (natural logarithm of PGA), respectively, obtained from GMPE.

The conditional pdf for PGV [$f(PGV|PGA, M_w, R, S)$ in Eqn. 3.1] is given by:

$$f(PGV|PGA, M_w, R, S) = \frac{1}{PGV \sigma_{\ln PGV|PGA, M_w, R, S}} \phi \left(\frac{\ln PGV - \mu_{\ln PGV|PGA, M_w, R, S}}{\sigma_{\ln PGV|PGA, M_w, R, S}} \right)$$

The mean ($\mu_{\ln PGV|PGA, M_w, R, S}$) and standard deviation ($\sigma_{\ln PGV|PGA, M_w, R, S}$) of the condi-

tional distribution are given by:

$$\begin{aligned}\mu_{\ln PGV|PGA,M_w,R,S} &= \mu_{\ln PGV|M_w,R,S} + \rho_{PGA,PGV} \frac{\sigma_{\ln PGV|M_w,R,S}}{\sigma_{\ln PGA|M_w,R,S}} (\ln PGA - \mu_{\ln PGA|M_w,R,S}) \\ \sigma_{\ln PGV|PGA,M_w,R,S} &= \sqrt{1 - \rho_{PGA,PGV}^2} \sigma_{\ln PGV|M_w,R,S}\end{aligned}$$

In the above equation, $\mu_{\ln PGV|M_w,R,S}$ and $\sigma_{\ln PGV|M_w,R,S}$ are the mean and standard deviation of $\ln PGV$, respectively, obtained from GMPE. $\rho_{PGA,PGV}$ is the correlation coefficient between PGA and PGV, which can also be obtained from the GMPE.

Suppose there are $K = I \times J$ bins in PGA-PGV space with $i = 1, \dots, I$ bins in PGA and $j = 1, \dots, J$ bins in PGV. Say the k^{th} bin contains PGA in the range of $a_1^k - a_2^k$ and PGV in the range of $v_1^k - v_2^k$, then the probability of ground motion occurrence within this bin is given by:

$$\begin{aligned}PO(a_1^k \leq PGA \leq a_2^k, v_1^k \leq PGV \leq v_2^k) \\ = \int_{PGA=a_1^k}^{a_2^k} \int_{PGV=v_1^k}^{v_2^k} f(PGA, PGV|M_w, R, S) dPGA dPGV\end{aligned}$$

The mean rate of occurrence of ground motion in this bin is the product of probability of ground motion occurrence within this bin [$PO(a_1^k \leq PGA \leq a_2^k, v_1^k \leq PGV \leq v_2^k)$] and the rate of occurrence (RT) for this specific forecast earthquake scenario, i.e.,

$$RT(a_1^k \leq PGA \leq a_2^k, v_1^k \leq PGV \leq v_2^k) = RT \times PO(a_1^k \leq PGA \leq a_2^k, v_1^k \leq PGV \leq v_2^k)$$

If there are $n = 1, \dots, N$ forecast earthquake scenarios in a ERF which produce ground motions in the k^{th} bin with occurrence rates $RT_n(a_1^k \leq PGA \leq a_2^k, v_1^k \leq PGV \leq v_2^k)$, then the total occurrence rate of ground motions within this bin is given by:

$$RT_{\bar{N}}(a_1^k \leq PGA \leq a_2^k, v_1^k \leq PGV \leq v_2^k) = \sum_{n=1}^N RT_n(a_1^k \leq PGA \leq a_2^k, v_1^k \leq PGV \leq v_2^k)$$

To apply this VPSHA method to the Pacifico rock, Purvance et al. employed the ERF used to construct the 2002 USGS National Seismic Hazard Maps and various GMPEs like that

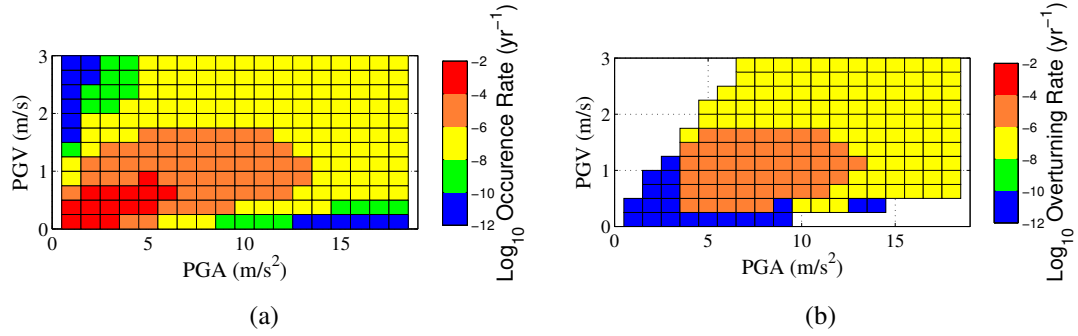


Figure 3.29: (a) Ground motion occurrence rate at the Pacifico rock site estimated by VPSHA methodology using the forecast earthquake scenarios from UCERF3 and (b) the overturning rate of the Pacifico rock obtained by multiplying the overturning probability of the rock with the ground motion occurrence rates in [(a)].

of Abrahamson and Silva (1997), Boore et al. (1997), Sadigh et al. (1997) and Campbell and Bozorgnia (2003). Since this PBR is present close to San Andreas Fault, we use the 10445 plausible earthquake scenarios postulated by United California Earthquake Rupture Forecast (UCERF3) [39] for accurately estimating the seismic hazard at this site. The total rate of ground motion occurrence at the Pacifico rock site estimated by applying the VPSHA methodology to the forecast earthquakes from UCERF3 is shown in Fig. 3.29(a). V_s^{30} (shear wave velocity at 30 m) at the PBR site is estimated to be 760 m/s [92] and the Campbell-Bozorgnia NGA ground motion models (2008) are used to calculate the PGA and PGV experienced at the PBR site from the 10445 forecast earthquake scenarios.

The product of the ground motion rate of occurrence [Fig. 3.29(a)] with the overturning probability of the Pacifico rock obtained in the previous section [Fig. 3.24(b)] gives the overturning rate of the Pacifico rock [Fig. 3.29(b)] in the PGV-PGA plane. Summing over all the bins in Fig. 3.29(b) gives the total overturning rate (\widehat{OR}) of the Pacifico rock to be $5.89 \times 10^{-4} \text{ yr}^{-1}$.

In UCERF3 and in standard probabilistic seismic hazard calculations, the distribution of earthquakes is assumed to follow a time-independent Poisson model. Therefore, the PBR fragility curve, which relates the time for which the PBR has been present at this site (t) to the probability that the ground motion model would overturn it during this time, is

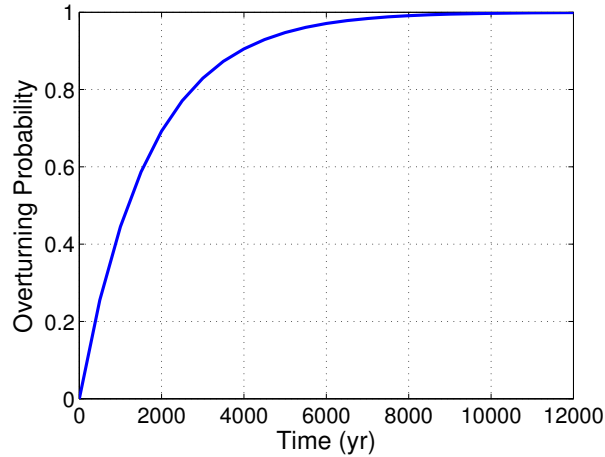


Figure 3.30: Overturning probability of the Pacifico rock as a function of the age of the rock when subjected to ground motions from UCERF3.

given by:

$$OP(t) = 1 - \exp(-\widehat{OR} t)$$

Fig. 3.30 gives the probability that the Pacifico rock would overturn as a function of the age of the rock for the Campbell-Bozorgnia NGA ground motion model applied to the forecast earthquakes from UCERF3. From this figure, it can be seen that the overturning probability is greater than 0.9 if the age of the rock is greater than 4000 years. But Bell et al. [15] estimated the age of the most of the PBRs present in Southern California to be at least 12000 years. Therefore, the seismic hazard at the Pacifico PBR site is over-predicted by the Campbell-Bozorgnia NGA ground motion model applied to UCERF3.

3.6.3 Comparison with synthetic ground motion simulations

Analyzing the Pacifico rock under synthetic ground motions from earthquake scenarios rupturing several distinct segments of the San Andreas Fault can help in verifying that these ground motions do not have characteristics that will overturn this PBR. Here, we use 10 earthquake scenarios generated by Mourhatch et al. [84] with M_w 7.89 rupturing different segments of the San Andreas Fault. These ground motions were generated by mapping the source from the 2002 Denali Earthquake onto the San Andreas Fault at 5 separate locations

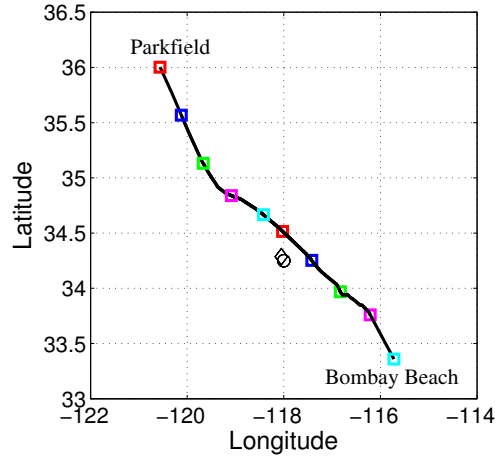


Figure 3.31: The black line indicates the part of the San Andreas Fault between Parkfield and Bombay Beach. The segment between squares of same color indicate ruptured region of the fault in each of the 5 earthquake scenarios. The black rhombus and circle indicate the location of the PBR and the station nearest to the PBR.

along the southern section of the fault starting at Parkfield in Central California and ending at Bombay beach in Southern California. Fig. 3.31 shows the different segments of the San Andreas Fault ruptured in each of the 5 scenarios considered (region between squares of same color). Two alternate rupture directions are considered at each of the 5 rupture segments, north to south rupture and south to north rupture, thus arriving at 10 earthquake scenarios.

The Pacifico rock is analyzed under 3-component ground motions experienced at the station nearest to it [black circle in Fig. 3.31] in each of the 10 earthquake scenarios. The E-W component of the ground motion is applied to the E-W orientation of the rock (along the slender cross-section of the rock). The friction coefficient used for this analysis is 1.0. The PBR rocks in response to the ground motion but does not overturn in any of the earthquake scenarios. Figs. 3.32(a) and 3.32(b) show the ground acceleration time history in the E-W direction and the center of mass displacement time history (with respect to ground) in the same direction, respectively, for one of the earthquake scenarios. These figures show that the PBR starts rocking when the strong ground motion pulse arrives at that location but the rocking response of the rock damps out quickly. There is a small offset (approximately 2 cm) in the final location of rock's center of mass which may be due to a small change in the orientation of the rock while rocking about different contact points and/or sliding.

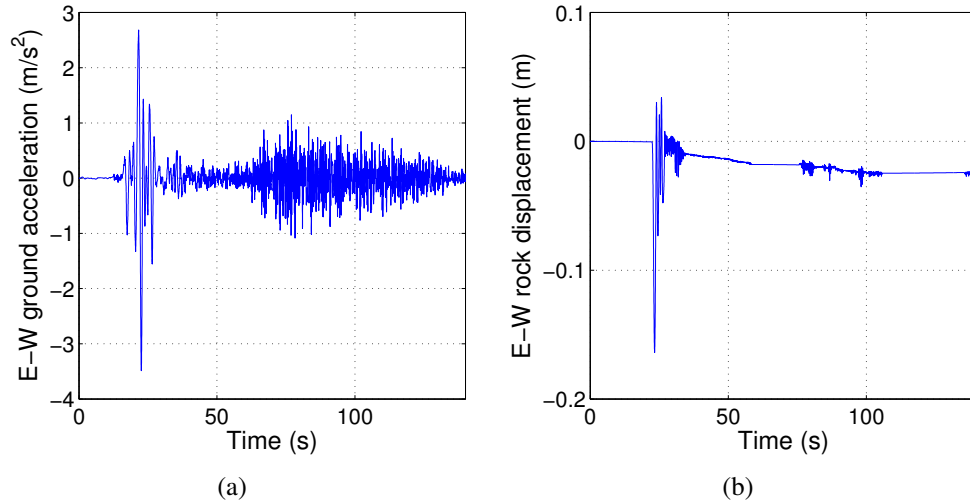


Figure 3.32: (a) E-W ground acceleration time history and (b) E-W center of mass displacement time history with respect to the ground for one of the 10 synthetic ground motions.

A similar reality check was conducted on the Southern California ShakeOut scenario by analyzing the Pacifico PBR under ground motions from 296 sites located 10-15 km from the fault and with the same site characteristics (V_s^{30}) as the Pacifico PBR site. The PBR did not overturn under any of these ground motions.

3.7 Summary

In this chapter, we have presented the methodology used to create 3-D models of PBRs and their supporting pedestals and to analyze them under three-component earthquake ground excitation. The accuracy of the rigid body dynamics algorithm used to analyze the rock models is first established through comparisons against shake-table tests on rocks. Fragility maps are then developed for the Echo Cliff PBR and the Pacifico rock by analyzing these rocks under ground motions from 140 earthquakes.

The overturning probability of the Echo Cliff PBR is quite low for PGA, PGV, and PGD below 3 m/s², 0.75 m/s, and 0.25 m, respectively. Similarly, the overturning probability of the Pacifico rock is quite low for PGA and PGV below 4 m/s² and 0.5 m/s, respectively. But PGDs lower than 0.25 m are also capable of overturning both the PBRs. While the PGV required to overturn the Echo Cliff PBR gradually increased with PGA for the Echo

Cliff PBR, the PGV required to overturn the Pacifico rock is more or less independent of the PGA (beyond PGA greater than 8 m/s^2). These results suggest that while a minimum PGA is required to initiate rocking response of the PBR, the toppling of the rock is dictated by the PGV of the ground motion record.

Additionally, we inferred that the PGV required to overturn the rocks does not depend on the duration of ground excitation whereas the PGA required to overturn the rock models decreases with increase in ground motion duration. Similarly, the PGA required to overturn the rock models also decreased with increase in PGV/PGA. These inferences reinforce the fact that overturning probability is most sensitive to PGV. The results from these analyses are compared with those from the empirical relation developed by Purvance et al. [88] and it is shown that the empirical relation under-predicts the overturning probability of the Echo Cliff PBR as well as the much simpler Pacifico rock.

The effect of the directionality of ground excitation, rock-pedestal interface friction coefficient, and vertical ground motion on the overturning probability of the Echo Cliff PBR was also explored. The overturning probabilities and the direction in which the Echo Cliff PBR overturned was more or less independent of the direction in which the strong component of the ground motion was applied because of two reasons: (i) half of the records selected for the study did not exhibit strong directionality and (ii) the pedestal on which the rock rests has a downsloping gradient (of about 5°) and a major fraction of the base of the rock along the same direction extends beyond the edge of the cliff as an overhang. A lower friction coefficient results in higher probability of overturning. However, the overturning probabilities for $\mu = 0.6$ and $\mu = 0.8$ are within ± 0.3 of those for $\mu = 1.0$. Vertical ground motion does play a role in the rocking-sliding response. However, there is no systematic relationship between vertical ground motion and the overturning probabilities, i.e., vertical ground motion may aid or impede the overturning of the rock. The overturning probabilities under 2-component ground motion (without the vertical component) are well within 0.3 of those under 3-component ground motion.

The Pacifico rock is slender along one direction and therefore it is more susceptible to rocking and overturning along that direction. The contact interface between the Pacifico rock and its pedestal has a downward sloping gradient of about 8° near the preferred direc-

tion of overturning. As the gradient in contact interface between the Pacifico rock is higher than that of the Echo Cliff PBR, the effect of sliding was more pronounced in the Pacifico rock than in the Echo Cliff PBR. However, as in the case of Echo Cliff PBR, there is no systematic relationship between vertical ground motion and the overturning probabilities.

We use the fragility maps generated from this study to test the seismic hazard predictions obtained at the PBR locations from the national seismic hazard maps (for the Echo Cliff PBR) and vector-valued probabilistic seismic hazard analysis (for Pacifico rock). The seismic hazard at both these locations is over-predicted. We also perform a reality check on the Southern California ShakeOut scenario and other synthetic ground motion simulations rupturing segments of the San Andreas Fault by verifying that the ground motions at the location of the PBR do not topple the PBR.

Chapter 4

Other Applications

The focus of the thesis until here has been on modeling the response of precariously balanced rocks to earthquake excitation and using the results to place constraints on the types of ground motions experienced by that region. In this chapter, we outline a methodology to extract quantitative information about earthquake ground motion experienced by a region from qualitative information about the rocking or sliding response of man-made objects like train, battery-rack, and nuclear storage canister.

4.1 Lower bounds on ground motion at Point Reyes during the 1906 San Francisco Earthquake from train toppling analysis

The 18th April, 1906 San Francisco earthquake (M_w 7.8) and the subsequent investigation of this earthquake [69] marked the birth of modern earthquake science in the United States. Mount Hamilton, at a distance of approximately 130 km from the San Andreas fault, was the location closest to the source where ground motion was recorded (by a three-component pendulum). Using this record as a constraint, Boore [21] and Lomax [74] located the earthquake hypocenter offshore (off the coast of San Francisco). Recently, efforts have also been made to recreate strong ground motion from this earthquake using the limited observations and inferences about the distribution of fault slip in that event [4, 98]. Given the sparsity of recorded data, there is still significant uncertainty in the epicentral (and hypocentral)



Figure 4.1: San Francisco- (south-) bound train which overturned at Point Reyes Station during the 1906 San Francisco earthquake [10].

location(s) and the intensity of near source ground motions during this earthquake.

A train, pulled by a narrow gauge locomotive (engine number 14, built in 1891 by Brooks and scrapped in 1935 [37]), overturned near Point Reyes station during this earthquake. The train was traveling south toward San Francisco on a N-S oriented line. An eye-witness account by a conductor documented by Jordan suggests that the train was initially stationary, lurched to the east then to the west, and fell off the track on to its side [62]. A photo of the overturned train, taken after the incident, is shown in Fig. 4.1 and a map with the train location (black circle) in relation to the San Andreas fault (red line) is shown in Fig. 4.2(a).

Estimating the ground shaking intensity (at least in the direction of toppling) needed to overturn the train in the manner documented by Jordan can supplement the limited available data from this earthquake. To this end, Anooshehpour et al. [10] idealized the rocking behavior of the train in 2-D to that of a rigid rectangular block of height 3.76 m and width 0.91 m supported on a rigid horizontal surface. The block was assumed to rock about two corners [O or O' on Fig. 4.2(b)] that correspond to the two sets of train wheels seated on the tracks. Collisions between the wheel and the track during rocking were assumed to be inelastic, i.e., it was assumed that bouncing did not occur upon impact. The fault-normal (orthogonal to the N-S alignment of the train and the line) ground motion was idealized to a full sinusoidal pulse. Their goal was to analytically determine a lower bound on the sine wave amplitude (and the corresponding pulse period) required to overturn the train model in the manner documented by Jordan. From moment balance about the contact point O (and

O'), the equation(s) of motion for the rocking response of a rectangular block subjected to horizontal base excitation $[\ddot{u}_g(t)]$ is (are):

$$\ddot{\theta} + p^2 \sin[-\alpha - \theta(t)] = -p^2 \frac{\ddot{u}_g(t)}{g} \cos[-\alpha - \theta(t)] \quad \theta(t) < 0 \quad (4.1)$$

$$\ddot{\theta} + p^2 \sin[\alpha - \theta(t)] = -p^2 \frac{\ddot{u}_g(t)}{g} \cos[\alpha - \theta(t)] \quad \theta(t) > 0 \quad (4.2)$$

where m is the mass of the block, g is the acceleration due to gravity, R is the distance of the contact point O or O' from the center of mass (c.g.), I is the moment of inertia of the block about either contact point, and $p^2 = mgR/I$.

This equation of motion is nonlinear and discontinuous. The trigonometric terms causing the nonlinearity are often linearized so that an approximate analytical solution may be obtained [10, 52, 99, 111]. Anooshehpour et al. used the linearized form of Eq. 4.1 with $\ddot{u}_g(t) = A \sin(\omega t + \psi)$ and estimated the minimum amplitude A of the sinusoidal ground acceleration required to topple the train to be 0.35 g [3.4 m/s²], 0.5 g [4.9 m/s²], and 1.05 g [10.3 m/s²] at frequencies of 1 Hz, 1.5 Hz, and 2 Hz, respectively. While the response of the train model under idealized pulses did provide interesting insights into the dynamics of the problem, Anooshehpour et al. correctly recognized that the model's response under an earthquake excitation can be significantly different from that under an equivalent idealized pulse [79, 106]. So they sought to analyze the train model under two scaled accelerograms, the Lucerne record from the 1992 Landers earthquake and a synthetic accelerogram at Point Reyes from a hypothetical M_w 8 earthquake rupture propagating northwest on the San Andreas fault with epicenter near the Golden Gate bridge (obtained from John Anderson through personal communication).

While the case of the simple full sine pulse excitation is amenable to solving analytically, this approach becomes intractable for complex excitation histories such as earthquake ground motion. The discontinuity in the equation (Eqs. 4.1 and 4.2), which arises due to a change in the point of rotation from O to O' (or vice-versa) upon impact of the block with the ground, is handled analytically by determining the times at which $\theta(t)$ goes to zero, and switching between the solutions of the two equations at these times. In doing this computation, the discontinuity arising out of the velocity reduction applied at impact to

simulate perfectly inelastic collisions [52] must be honored as well. Another source of discontinuity in the equation of motion is the change in the equation of motion with the form of the ground excitation. Even in the case of a block subjected to a full-sine wave, once this excitation ends, two different equations of motion arise and the time of impact in relation to the excitation period determines which equation of motion needs to be solved next. The solution for $\theta(t)$ in all equations contains *cosh* and *sinh* terms and the time at which $\theta(t)$ goes to zero, i.e., time of impact, cannot be solved analytically. Therefore, different cases have to be formulated based on whether impact occurs before or after excitation ends. If this approach were to be employed for earthquake excitation discretized in a piece-wise linear fashion, there would exist a separate equation of motion for each piecewise part of the excitation and this coupled with the discontinuity in equation of motion arising due to impact would result in an analytically intractable number of cases.

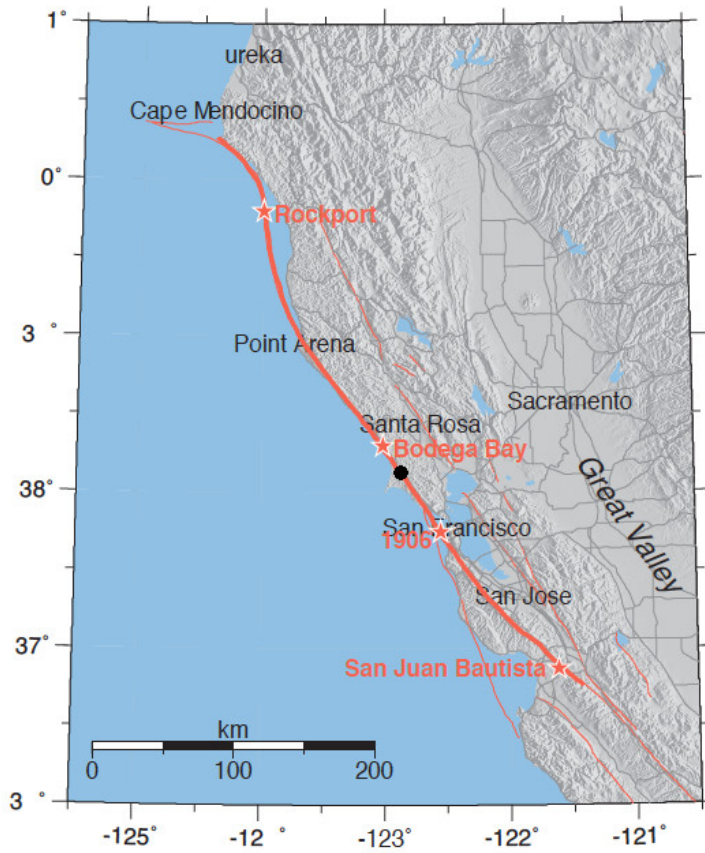
The nonlinearity and discontinuity in the rocking dynamics of the rectangular block also make it difficult to superpose analytical results obtained for simple ground excitations such as sinusoidal pulses and impulses to estimate its response under complex excitation histories such as earthquake ground motion (using Fourier series or other techniques). Recognizing these difficulties, Anooshehpour et al. [10] numerically solved the equations of rocking motion [Eqs. 4.1 and 4.2] for the rectangular train model under the two seismograms, scaled to different levels. The Lucerne record scaled to a PGA level of 0.76 g [7.5 m/s²] topples the train model, whereas the synthetic seismogram from the hypothetical San Andreas fault earthquake scaled to a PGA level of 1.1 g [10.8 m/s²] topples the model. They also used lowpass-filtered (with a corner frequency at 3 Hz) versions of these accelerograms and found that high-frequency ground motion plays a significant role in initiating the rocking motion which can then be sustained with low-amplitude, low-frequency ground shaking.

It has been shown that the solution to the equation of motion is sensitive to small variations in excitation frequency, phase, and amplitude of excitation [60, 113]. Therefore, there is a need to expand the types and number of earthquake records used in establishing the toppling fragility characteristics of the train model in order to estimate the ground motions experienced at Point Reyes station during the 1906 San Francisco earthquake. Furthermore,

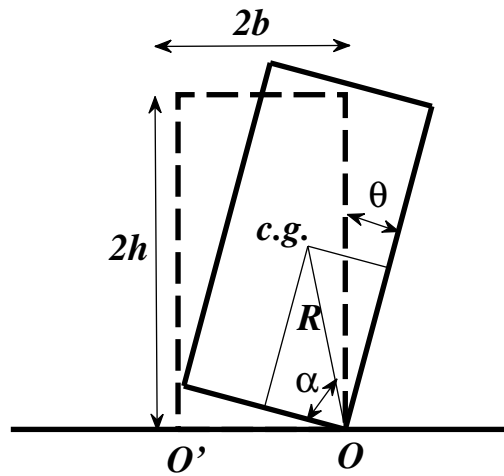
the Anooshehpour et al. [10] analysis was conducted using a single horizontal component of shaking. The effects of vertical ground motion were not considered. Yim et al. [113] showed that vertical ground motion does not systematically affect the rocking response of a rectangular block. However, this result was based on the linearized rocking equation of motion. Here, we analyze the rectangular train model under both vertical as well as horizontal ground motions from 140 worldwide earthquake records to obtain the overturning fragility of the train as a function of ground motion parameters. We also analyze the train model under the ground motions at Point Reyes station from 1906-like earthquake simulations by Aagaard et al. [4] with ruptures initiating at four different locations [indicated by the red stars in Fig. 4.2(a)] to arrive at independent constraints on the possible hypocenter location of the 1906 San Francisco earthquake.

4.1.1 Overturning fragility of the train

There have been numerous analytical, numerical, and experimental studies on the rocking response of a rectangular block under ground excitation [52, 88, 111, 115]. Here, we use the rigid body dynamics algorithm presented in Chapter 2 to analyze the rocking response of the train model under earthquake excitation. While the algorithm is capable of simulating three-dimensional response under 3-component ground motion, we limit ourselves to 2-D analysis here. We concur with Anooshehpour et al. that the train resting on rails may be viewed as a very long rectangular block that will predominantly rock in its shorter direction, i.e., perpendicular to the tracks. Some rolling may have occurred along the tracks, but the response in the two directions may, for all practical purposes, be considered to be uncoupled (given the far greater length of the locomotive compared to its width). We maintain the assumptions of rocking only about the two points where the wheels come in contact with the tracks (denoted by O and O' in Fig. 4.2(b)) and perfectly inelastic collisions upon impact between the wheels and the rails (when the point of rotation switches from O to O' or vice versa). The latter assumption is realized by setting the coefficient of restitution to zero. The rails prevent the train from sliding in the direction perpendicular to the rails. So, a high value of 1.2 is used for static and kinetic coefficients of friction between the train



(a)



(b)

Figure 4.2: (a) A map showing the San Andreas fault (red line) and Point Reyes Station (black circle). The red stars indicate the hypocenter locations for four 1906-like San Francisco earthquake simulations by Aagaard et al. [4]. The star near San Francisco corresponds to the widely accepted hypocenter location. (b) 2-D rectangular block model of the train.

model and the ground to prevent the model from sliding. The suspension system installed in the train is assumed to be sufficiently stiff for the train to behave as a rigid body. This assumption may not be valid for locomotive that have been designed and manufactured in the recent years.

The 140 earthquake records used to analyze the train model come from worldwide earthquakes with magnitudes greater than 6 and source-to-site distances less than 100 km (see [89] for the list of earthquakes). The records are first normalized such that the peak ground acceleration (PGA) of the strong ground motion component is 1 m/s^2 . The normalized records are then scaled to yield records with PGA from 1 m/s^2 to 19 m/s^2 in steps of 1 m/s^2 . Because differentiation is a linear operation, the peak ground displacements (PGD) and the peak ground velocities (PGV) also scale by the same scaling factors as the corresponding PGAs.

A total of 2660 time-history analyses of the train model are performed. In each instance, the strong component of the horizontal ground motion is applied along the width of the train model and the vertical ground motion is applied along its height. The overturning probability of the train model on the PGA-PGD, the PGA-PGV, and the PGV-PGD planes are shown in Figs. 4.3(a), 4.3(b), and 4.3(c), respectively. These plots are developed by binning the 140 scaled records at each PGA level into PGD bins of 0.25 m width [for Figs. 4.3(a) and 4.3(c)] and PGV bins of 0.25 m/s width [for Fig. 4.3(b)]. The overturning probability in each bin at each PGA level is the fraction of records (in that bin and that PGA level) that overturn the model. It should be noted that the PGA-PGD, the PGA-PGV, and the PGV-PGD domains in Fig. 4.3 are not uniformly sampled by the 2660 scaled records. The sampling of different regions of the domain can be gauged by the varying thickness of each column (at each PGA level). The thickness of the column at each *PGA* level in a given *PGD* or *PGV* bin is proportional to the fraction of points (out of 140) being sampled in that bin. For e.g., 60 of the 140 records at a PGA level of 4 m/s^2 have a PGD between 0 m and 0.25 m, whereas 20 of the 140 records at that PGA level have a PGD between 0.25 m and 0.5 m and so on. The thickness of the lower bin with PGD between 0 m and 0.25 m is proportional to 60/140 and the thickness of the upper bin with PGD between 0.25 m and 0.5 m is proportional to 20/140. Regions with thinning columns are regions

that are sparsely sampled; obviously, the results there may not be as reliable as the densely sampled regions.

The colored contour lines correspond to overturning probabilities of 0.1, 0.3, 0.5, 0.7, and 0.9. It can be seen from these figures that a minimum PGA of 4 m/s^2 is required for the train to overturn. For comparison, the quasi-static acceleration needed to uplift one corner of the train model and get it to start rocking is 2.5 m/s^2 . Beyond the PGA threshold of 4 m/s^2 , the overturning probability is independent of the PGA , as indicated by the horizontally aligned contours. We should point out that our records do not sample the low PGA -high PGD or low PGA -high PGD regimes. It is possible that such records do end up toppling the train model. We simply cannot tell from our dataset. From Figs. 4.3(a) and 4.3(b), it appears that the probability of overturning is quite low when the PGV and PGD are below 1 m/s and 0.25 m , respectively, whereas the overturning probability goes up quite rapidly when the PGV and PGD exceed these values. A small fraction of the records with PGV in the range of 0.75 - 1.0 m/s and a PGA in the range of 5 - 10 m/s^2 is able to overturn the train model.

Next, we normalize and scale the ground motion records such that PGV of the strong horizontal ground motion component takes values between 0.25 m/s and 5 m/s in steps of 0.25 m/s . We repeat the analysis of the train model using these scaled ground motion records in order to obtain its overturning probability as a function of PGD and PGV . The scaling with respect to PGV (as opposed to using the results from PGA -scaled records) allows us to populate the PGD - PGV plane more uniformly. The 140 earthquake records at each PGV level are divided into PGD bins of width 0.25 m . The overturning probability within each bin at each PGV level is calculated as the ratio of the number of records that overturn the model to the total number of records in that bin at that PGV level. Fig. 4.3(c) shows this overturning probability on the PGD - PGV plane. Unlike Figs. 4.3(a) and 4.3(b), the contour lines in this figure are not horizontally oriented. Beyond the threshold of 1 m/s , the greater the PGV , the smaller is the PGD needed to overturn the model. A small fraction of the records with PGD in the range of 0 - 0.25 m and a PGV in the range of 1.5 - 2 m/s is able to overturn the train model. Therefore, unlike PGV and PGA there is no real threshold in PGD below which the the train does not overturn.

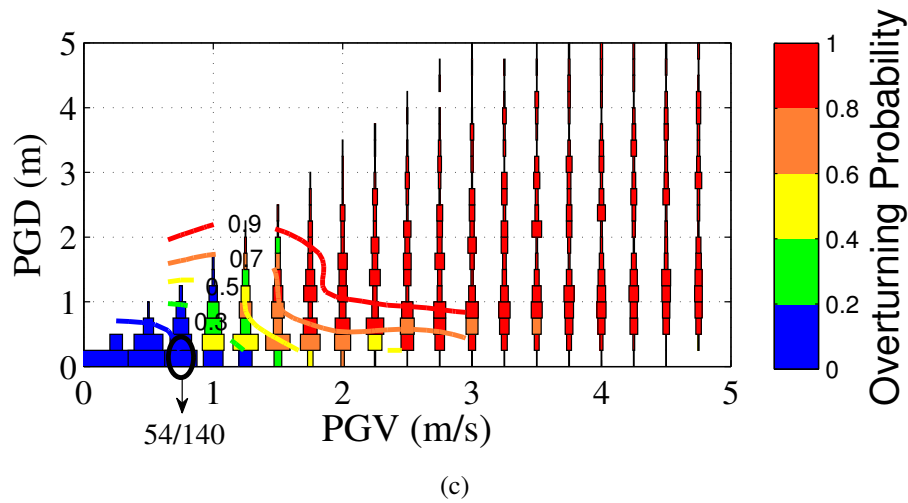
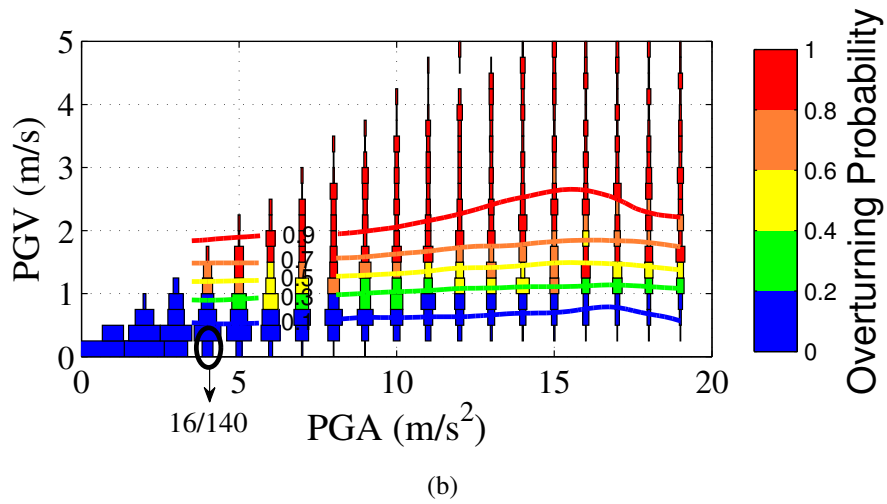
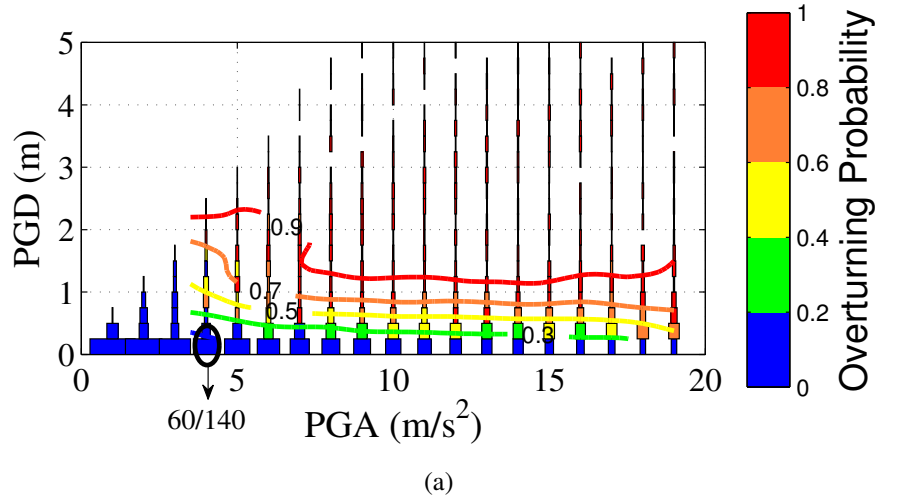


Figure 4.3: Overturning probability of the train model as a function of (a) PGD and PGA, (b) PGV and PGA, and (c) PGD and PGV. Each column in the figures contains 140 earthquake records scaled to a specific PGA level [(a) and (b)] or PGV level [(c)]. The varying thicknesses of the column are proportional to the fraction of earthquakes (out of 140) being sampled in a given PGD or PGV bin.

The near-horizontal contours on Figs. 4.3(a) and 4.3(b) suggest that the train model is not very sensitive to high-frequency parts of the ground motion spectrum beyond the PGA threshold of 4 m/s^2 . To further explore the sensitivity of the overturning probability to the frequency content of the ground motion, we consider three measures of ground motion time period: (i) PGV/PGA, (ii) PGD/PGV, and (iii) the time period (T) that maximizes the pseudovelocity response spectrum. Note that these time period measures do not change when the records are scaled. The PGV/PGA (blue asterisks) and the PGD/PGV (red squares) period measures for the 140 ground motion records are shown plotted as a function of T in Fig. 4.4(a). While there appears to be a linear correlation between PGV/PGA and the time period T that maximizes the pseudovelocity response spectrum, a strong correlation is not observed between PGD/PGV and T.

Using the results from the records scaled to achieve various PGA levels, the overturning probability as a function of PGA and PGV/PGA is shown in Fig. 4.4(b). As before, the 140 records at each PGA level are divided into PGV/PGA bins of width 0.05 s. The thicknesses of the columns along the PGV/PGA axis are proportional to the fraction of earthquake records (out of 140) that are sampled in a given PGV/PGA bin. Similarly, the overturning probability in the PGV-PGD/PGV and PGV-T planes are shown in Figs. 4.4(c) and 4.4(d), respectively. These are developed using the records scaled to achieve various PGV levels. For these figures, the 140 earthquake records at each PGV level are divided into PGD/PGV and T bins of width 0.15 s and 0.5 s, respectively. The PGA and PGV required to overturn the train model decrease more or less monotonically with increasing PGV/PGA and PGD/PGV [Figs. 4.4(b) and 4.4(c)]. However, the PGV required to overturn the train model appears to share a parabolic relationship with T [Fig. 4.4(d)] with the records that have periods near 1.6 s requiring the smallest PGVs to overturn the train model.

To better understand this sensitivity of the train model to time period, let us go back to the equation of motion for the rocking response of the rectangular block [Eqn. 4.2]. Linearizing the equation of motion gives:

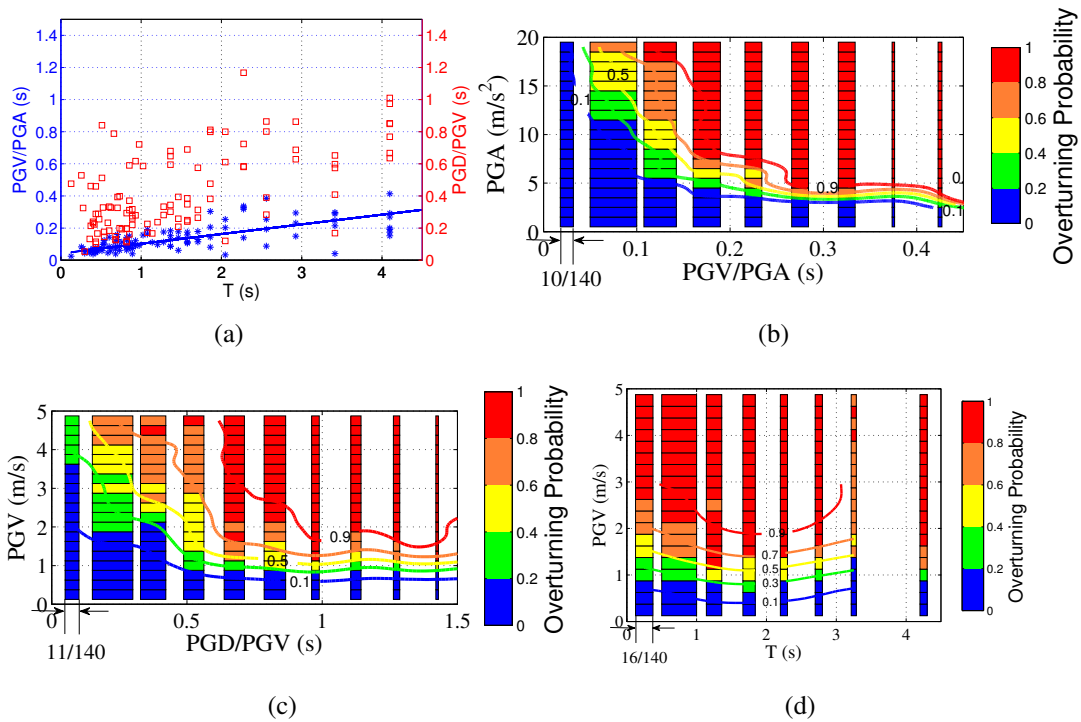


Figure 4.4: (a) PGV/PGA and PGD/PGV of the 140 earthquake records as a function of T , the period at which the peak of the pseudovelocity response spectrum occurs. (b), (c), and (d) Overturning probability of the train model as a function of PGA and PGV/PGA, PGV and PGD/PGV, and PGV and T , respectively. The PGA and PGV required to overturn the train model monotonically decreases with increasing PGV/PGA and PGD/PGV, respectively, but decreases first and then increases with increasing T , attaining a minimum at a T of about 1.6 s. Each row in these figures contain 140 earthquake records scaled to a given PGA [(b)] or PGV [(c) and (d)] level. The column thicknesses are proportional to the fraction of earthquakes (out of 140) that are sampled in a given PGV/PGA, PGD/PGV, or T bin.

$$\ddot{\theta} - p^2\theta(t) = -p^2\left[\frac{\ddot{u}_g(t)}{g} - \alpha\right] \quad \theta(t) > 0 \quad (4.3)$$

The left hand side of the equation of motion is different from that of a spring mass system undergoing simple harmonic motion (SHM) due to the negative sign accompanying θ . As mentioned previously, the free vibration solution for θ is a linear combination of non-periodic *cosh* and *sinh* functions. So rigid bodies do not have a natural propensity to rock at a “natural frequency or period” unlike spring-mass oscillators. The time taken to complete one cycle of rocking is dependent upon the amplitude of rocking [52], unlike SHM where the period of oscillation is a function of the physical properties of the system alone. Therefore, resonance cannot occur in rigid-body rocking driven by external excitation and it is not expected that the rocking response of a rectangular block will be sensitive to excitations with a particular time period.

The dependence of overturning probability on ground motion period (PGV/PGA) was presented in Fig. 4.4. The ground motion duration, which specifies the duration of the earthquake record that contains 90 % of the energy, could also affect the overturning probability. Here, we calculate the duration of the 140 earthquake records using the energy integral formulation developed by Anderson [8]. This method calculates the cumulative energy released by the earthquake by integrating the square of the velocity time history. Figs. 4.5(a) and 4.5(b) show the overturning probability in the PGV-duration and PGA-duration planes, respectively. For these figures, the 140 earthquake records at each PGA or PGV level are divided into duration bins of width 5 s. Fig. 4.5(a) shows that the PGV required to overturn the rock model is more or less independent of the duration of the earthquake. However, the PGA required to overturn the rock model decreases more or less uniformly with duration.

The train overturning fragility maps obtained here may be used to check whether the synthetic ground motions from the 1906 San Francisco earthquake simulations by Aagaard et al. [4] are realistic. They simulated several rupture scenarios using a source model developed by Song et al. [98] and a recently constructed 3-D seismic wave-speed model of

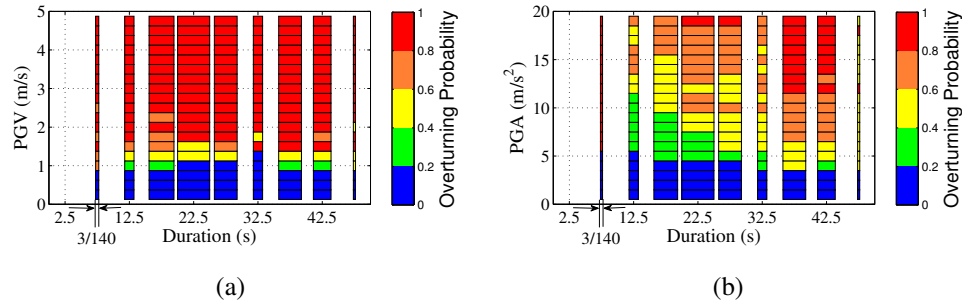


Figure 4.5: Overturning probability of the train model as a function of (a) PGV and duration, and (b) PGA and duration. Each row in these figures contains 140 earthquake records scaled to a given PGV [(a)] or PGA [(b)] level. The column thicknesses are proportional to the fraction of earthquakes (out of 140) that are sampled in a given duration bin.

northern California. Three of these scenarios involved the rupture of the same extent of the northern San Andreas fault, but with rupture initiating at Bodega Bay (to the north of San Francisco), offshore from San Francisco in the middle, and San Juan Bautista at the southern end [Fig. 4.2(a)]. The ruptures nucleating at Bodega Bay and San Francisco are bilaterally propagating ruptures, whereas the rupture originating at San Juan Bautista propagates predominantly in a south-to-north direction. The three scenarios predict PGA between 4.5 m/s^2 and 6.0 m/s^2 , PGV between 0.8 m/s and 1.6 m/s , and PGD between 0.8 m and 1.6 m at Point Reyes. For these ranges of ground motion intensities, the train overturning probability from the fragility maps ranges between 0.4 and 0.8. Thus, Aagaard et al.'s simulations clearly do not over-estimate the ground motion intensities at Point Reyes. They may, in fact, be quite realistic.

4.1.2 Hypocenter location of the 1906 San Francisco earthquake

The ground motion histories at Point Reyes (station SF432) from the three rupture scenarios (with three hypocenter locations) may also be used to determine the most plausible of the three hypocenter locations and could independently verify the estimates by Boore [21] and Lomax [74]. Ground velocity time histories at the Point Reyes Station (station SF432) are retrieved from a USGS repository of these simulations [5]. The train model is analyzed under each of these ground motion histories. The horizontal displacement response histories of the center of mass of the train model with respect to the ground are given in

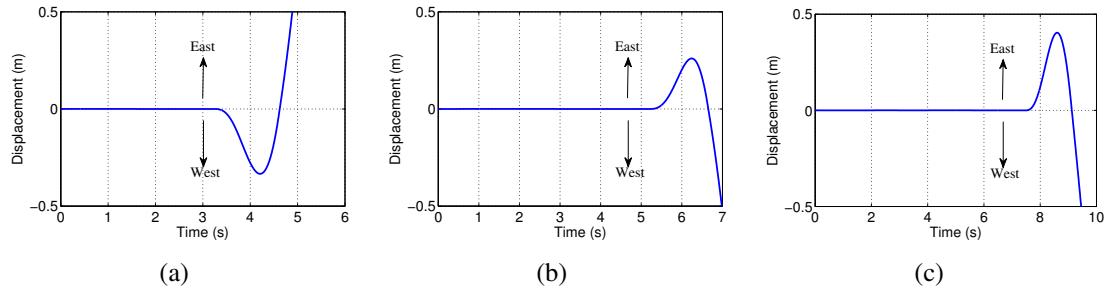


Figure 4.6: Horizontal displacement time histories of the center of mass of the train with respect to the ground when subjected to the synthetic ground motion histories at Point Reyes station from the three 1906-like scenario earthquake simulations by Aagaard et al. [4] with hypocenter located at (a) Bodega Bay (north of Point Reyes), (b) offshore from San Francisco (south of Point Reyes) and (c) San Juan Bautista (further south of Point Reyes). Displacements to the east are positive.

Figs. 4.6(a) (hypocenter at Bodega Bay), 4.6(b) (hypocenter at San Francisco), and 4.6(c) (hypocenter at San Juan Bautista). Displacements to the east are positive. All three ground motions overturn the train model. However, only the scenarios with the hypocenter located south of Point Reyes (i.e., offshore from San Francisco and San Juan Bautista) produce ground motions that overturn the train in the manner documented by Jordan (the train first lurching to the east and then overturning in the west). Therefore, our analysis places the hypocenter of the 1906 earthquake to the south of Point Reyes station. This inference does not conflict with the currently accepted hypocenter location near San Francisco [74].

4.2 Estimating PGA and PGV from the maximum sliding displacement of a battery rack in Haiti

The M 7.0 Haiti earthquake, which occurred on 12th January, 2010, was not recorded by any strong motion instruments in Haiti. Here, we estimate the near source peak ground acceleration (PGA) and peak ground velocity (PGV) from qualitative observations about the displacement of an industrial battery rack present at the Voila building [51]. The battery racks shown in Fig. 4.7(a) have length $l = 141$ cm, height $h = 172$ cm, and width $w = 56$ cm with mass $m = 3490$ kg. Each battery rack was bolted to the tile floor using four bolts before the occurrence of the earthquake. During the main shock event, two of the



Figure 4.7: (a) Battery rack located in the Voila building and (b) photograph of the scratches on the tiles caused by sliding motion of the battery rack during the main shock of the 2010 Haiti earthquake [51].

battery racks [labeled S and N in Fig. 4.7(a)] had displaced from their initial position. From the field study conducted by Hough et al. [51], the bolts holding down rack S appeared to have been pulled out while those holding down rack N appeared to have broken. All the other racks in the room appeared to be undisturbed from their original positions. From the limited data available from the field, Hough et al. inferred that the bolts holding down rack S were most likely improperly installed and thus were pulled out during a strong motion pulse and the collision of rack S with rack N caused the bolts of rack N to break. The sequence in which the bolts holding down rack S were pulled out is unclear. The movement of rack S is clearly marked on the ground [Fig. 4.7(b)]. However, if there was a collision between rack N and rack S , then along with the earthquake ground motion, this collision could have also contributed to the sliding of the battery rack. Hough et al. made qualitative judgements based on the displacement traces of rack N and rack S and estimated the maximum sliding displacement of the unbolted rack S in N-S (short) and E-W directions caused primarily due to earthquake excitation to be in the range of 22 – 27 cm and 24 cm, respectively. Additionally, the scratch marks on the ground indicate that the rack did not rock after it was free to move.

Hough et al. [51] divided this problem into two independent parts: (i) estimating the minimum PGA required to break the bolts, and (ii) estimating the range of PGA required to cause a sliding displacement of 22 – 27 cm in the unbolted battery rack. Since the ground

motion was not strong enough to break the properly installed bolts, the minimum PGA required to break the bolts is the upper limit to the PGA experienced at this location. It should be noted that there may be other failure mechanisms which might cause the bolts to break at lower PGAs. For the first part of the problem, Hough et al. [51] assumed the nominal tensile strength of the 0.25 in diameter steel bolts to be $\sigma_t = 4.14 \times 10^8$ Pa. Using moment balance along the longer edge of the battery rack, they estimated the PGA required to break the bolt to be 8.13 m/s^2 . However, this analysis does not take into account the effect of vertical ground motion.

For the second part of the problem, Hough et al. used the results of a similar analysis conducted by Taniguchi et al. [100] and estimated the range of PGA required to cause the observed sliding displacement to be $2.94 - 6.86 \text{ m/s}^2$. However, the upper bound on the PGA may not be accurate due to the inherent difficulty in applying the results from Taniguchi et al.'s work to this problem. The aim of the Taniguchi et al.'s work was to arrive at a quick estimate for the maximum sliding displacement of a rectangular block placed on a ground during an earthquake. For this analysis, they assumed the coefficient of friction between the block and the ground to be sufficiently low so that the block experiences only sliding response. Using the equations of motion that correspond to the block's sliding mode of response, they obtained an analytical expression for the block's maximum sliding displacement as a function of the input horizontal sinusoidal pulse parameters. They also obtained the block's maximum sliding displacement under the dominant horizontal ground motion from 104 Japanese earthquakes by solving the equation of motion numerically and compared this displacement with that obtained using the equivalent sine wave. Here, the amplitude of the equivalent sine wave is same as the PGA of the earthquake and the time period is the one that maximizes the spectral acceleration of the earthquake. From this comparison, they found that the block's maximum sliding displacement during an earthquake is bounded from above (in approximately 93 of the 104 considered earthquakes) by the displacement under the equivalent sine wave scaled up by a factor of 1.84. Since this analysis only provides an upper bound on the block's maximum sliding displacement under an earthquake, this result cannot be directly extended to the reverse problem of estimating the ground motion parameters given the observed sliding displacement of the block under

an earthquake.

In order to apply Taniguchi et al.'s results to the second part of the battery rack problem, Hough et al. [51] first estimated the coefficient of friction between the battery rack and the ceramic tile floor to be between 0.15 and 0.2 from established values of coefficient of friction between steel and slippery materials like teflon. They confirmed that the unbolted battery rack can only undergo sliding response for this value of friction coefficient. Also, based on the recorded ground motions at the location of the battery rack from the aftershocks, they estimated the predominant period of the main shock ground motion to be between 0.5 s and 1.0 s. Next, from the analytical expression derived by Taniguchi et al. [100] for the block's maximum sliding displacement as a function of the sine wave parameters, Hough et al. [51] calculated the amplitudes (PGAs) of sine waves with time periods between 0.5 s and 1.0 s required to cause the observed sliding displacement scaled down by a factor of 1.84. The range of PGA thus obtained is 2.94–6.86 m/s² for μ between 0.15 – 0.2. However, Taniguchi et al.'s work only implies that the battery rack's maximum sliding displacement under earthquakes with PGA and T belonging to this range is almost always less than the observed displacement of the battery rack. Therefore, this range only constitutes the minimum PGA and T combination required to cause the observed displacement and is not the complete set of ground motion parameters that can cause the observed displacement of the battery rack. Also, this analysis does not include the complete effect of the vertical and the non-dominant component of the ground motion.

Here, we address the issues in the analysis conducted by Hough et al. [51]. We model the battery rack from Haiti as a finite rectangular cuboid with the four corners as contact points and subject it to 140 strong ground motion records (see [89] for the complete list) from worldwide earthquakes with magnitude greater than 6 and distance from epicenter less than 100 km. The dominant component of the ground motion is applied in the N-S (short) direction of the rack. The ground motions are normalized such that PGA of the dominant horizontal ground motion is 1 m/s². The response spectra for these normalized ground motions in the N-S and E-W direction are presented in Figs. 4.8(a) and 4.8(b), respectively. In order to accurately estimate the minimum PGA required to break the bolts, we include the vertical ground acceleration into the calculations performed by Hough et

al. [51]. For each of the 140 normalized ground motions we estimate the scaling factor α required to break the bolt using moment balance along the longer edge as follows:

$$m\alpha A_x \frac{h}{2} - m(g - \alpha A_y) \frac{w}{2} = 2\sigma_t \left(\pi \frac{d^2}{4}\right) w \quad (4.4)$$

Here, A_x and A_y are the horizontal (along N-S) and vertical ground acceleration, respectively, at the time t which maximizes $A_x(t)h + A_y(t)w$, and g is the acceleration due to gravity. The scaling factors obtained have a mean of 9.79 with a standard deviation of 2.4. Therefore, the mean PGA required to break the bolt is 9.79 m/s².

For the second part of the problem of estimating the PGA required to cause the observed maximum sliding displacement of the battery rack, the normalized ground motions are scaled from $PGA = 1 \text{ m/s}^2$ to 20 m/s^2 in steps of 1 m/s^2 . The model of the rack is analyzed under each of the scaled ground motion records. The coefficient of friction between the battery rack and the tile floor is assumed to be between 0.15 and 0.2 [51] and this results in pure sliding response of the battery rack on the tile floor. The maximum displacement of the center of mass of the rack in the horizontal direction as a function of PGA is shown plotted on a log scale in Figs. 4.9(a) and 4.9(b) for $\mu = 0.15$ and $\mu = 0.2$, respectively. Here, the maximum displacement is the peak of the square root of sum of squares (SRSS) of the center of mass displacement time-histories in the two horizontal directions. Based on Hough et al. [51], the ground motion records with spectral acceleration peaks occurring between periods of 0.5 s and 1.0 s, indicated by black lines on Figs. 4.8(a) and 4.8(b), are of particular interest. The green filled circles in Figs. 4.9(a) and 4.9(b) represent the maximum displacement for these earthquake records. For each PGA level, the displacements are assumed to be log-normally distributed. This implies that the logarithm of the displacements are normally distributed. Therefore, the mean (ν) and standard deviation (σ) for the corresponding normal distribution can be obtained for the set of displacements at each PGA level. The black line indicates the line joining the mean (e^ν) for each PGA, the red solid and dashed lines correspond to mean \pm one standard deviation ($e^{\nu \pm \sigma}$) and mean \pm two standard deviations ($e^{\nu \pm 2\sigma}$), respectively. For the normal distribution, the subset of the displacements within two standard deviations from the mean account for 95.45% of

the total set of displacements. Therefore, we consider the earthquake records that produce displacement within two standard deviations of the mean response for obtaining the PGA range. The gray shaded region corresponds to the range of observed sliding displacement (32.5 cm – 36 cm). As can be seen from the Figs. 4.9(a) and 4.9(b), the ranges of the PGA required to cause the observed displacement of 32.5 – 36 cm are 3.0 – 20.0 m/s² and 4.0 – 20.0 m/s² for $\mu = 0.15$ and $\mu = 0.2$, respectively. The upper bound is in reality greater than 20 m/s² but PGA greater than 20 m/s² are uncommon so the upper limit has been truncated to 20 m/s². These ranges do not change significantly when a subset of results from earthquake records with $0.5 \text{ s} < T < 1.0 \text{ s}$ (identified by green-filled circles in Fig. 4.9) is considered. The above ranges are very wide and PGA as high as 20 m/s² are not realistic at a location. However, the PGA required to break the bolt can place a tighter upper bound on PGA experienced at this location.

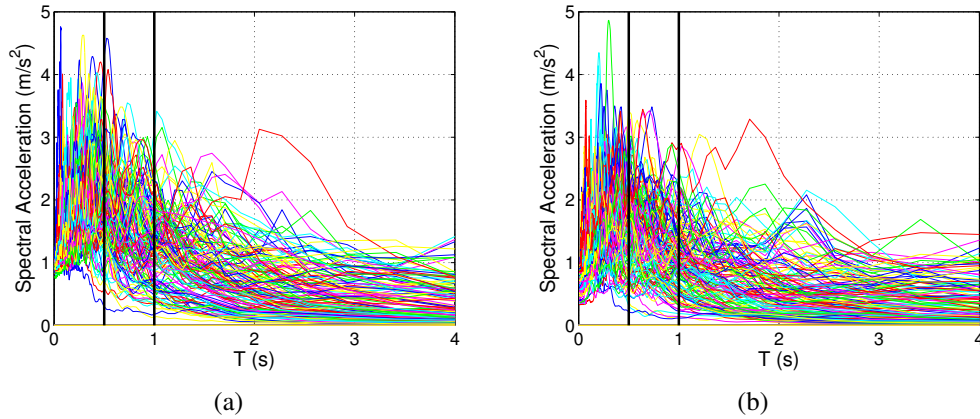


Figure 4.8: Response spectra for the 140 normalized ground motions applied in the (a) N-S and (b) E-W direction of the battery rack. The ground motions which have peak spectral acceleration between $0.5 \text{ s} < T < 1.0 \text{ s}$, indicated by black lines, are the ground motions which are more probable at the Voila building location.

Combining the results from both parts of the problem, the PGA ranges that cause the observed displacement of the battery rack without breaking the properly installed bolts are 3.0 – 9.79 m/s² and 4.0 – 9.79 m/s² for $\mu = 0.15$ and $\mu = 0.2$, respectively. In comparison, Hough et al. [51] estimate PGA to be in the 2.94 – 6.86 m/s² range for the same values of μ . The lower end of this range matches well with our results. As mentioned earlier, the upper limit of the range obtained by Hough et al. is incorrect as their analysis gives only the

minimum PGA and T combination required to cause the observed sliding displacement of the battery rack. From the catastrophic collapse of the very poorly built buildings adjacent to the Voila facility and significant non-structural and light structural damage to the well-built Voila facility, Hough et al. [51] concluded the damage to be consistent with modified Mercalli intensity scale (MMI) VIII. From correlations established between MMI and PGA by comparing horizontal peak ground motions to observed intensities for eight significant California earthquakes, MMI VIII and IX corresponds to PGA ranges of $3.33 - 6.37 \text{ m/s}^2$ and $6.37 - 12.152 \text{ m/s}^2$, respectively [107]. The results from our analysis agree well with these results on the lower limit of the PGA, and the upper limit suggests that the MMI at this location could have been VIII-IX.

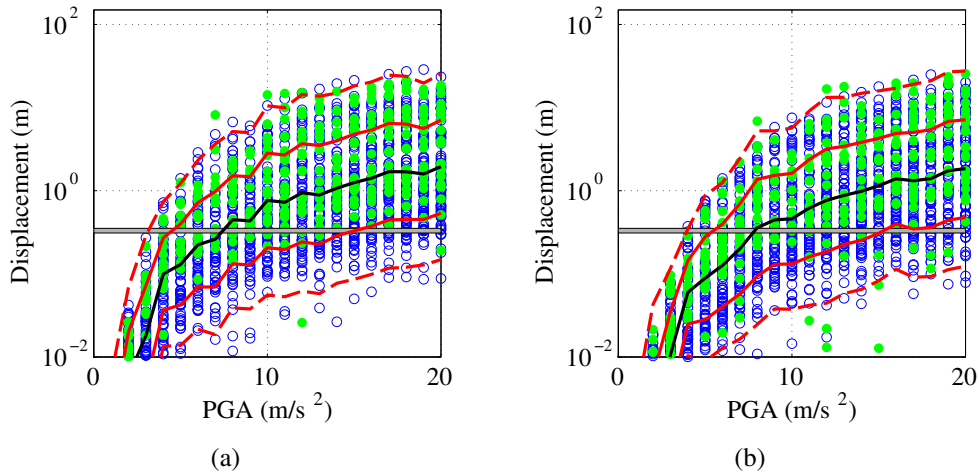


Figure 4.9: The maximum displacement of the battery rack when subjected to 140 earthquake records scaled to different PGA levels for (a) $\mu = 0.15$ and (b) $\mu = 0.2$. The green filled circles are the maximum effective displacement from earthquake records with $0.5 \text{ s} < T < 1.0 \text{ s}$. The black line shows the line joining mean e^ν , the red solid and dashed lines correspond to mean \pm one standard deviation ($e^{\nu \pm \sigma}$) and mean \pm two standard deviations ($e^{\nu \pm 2\sigma}$), respectively. The gray shaded region represents the observed displacement ($0.325 - 0.36 \text{ m}$). The ranges of the PGA required to cause the observed displacement are $3 - 20 \text{ m/s}^2$ and $4 - 20 \text{ m/s}^2$ for $\mu = 0.15$ and $\mu = 0.2$, respectively.

To estimate the corresponding ranges for peak ground velocity (PGV), a similar analysis is conducted by normalizing the 140 earthquake records such that PGV of the dominant horizontal ground motion component is 1 m/s . These normalized ground motions are then scaled from $PGV = 0.5 \text{ m/s}$ to 10 m/s in steps of 0.5 m/s . $PGV = 0.25 \text{ m/s}$ is also considered. The maximum effective displacement of the rack under these scaled records is

shown plotted as a function of PGV for $\mu = 0.15$ and $\mu = 0.2$ on Figs. 4.10(a) and 4.10(b), respectively. As earlier, we consider earthquake records that produce displacements within two standard deviations of the mean response for obtaining the PGV range. The range of the PGV required to cause the observed displacement of 32.5 – 36 cm is 0.5 – 2.5 m/s and 0.5 – 3 m/s for $\mu = 0.15$ and $\mu = 0.2$, respectively. As for PGA, this range does not change significantly when a subset of results from earthquake records with spectral acceleration peaks occurring between $0.5 \text{ s} < T < 1.0 \text{ s}$ is considered. For these 140 PGV normalized ground motions, we estimate the scaling factor α required to break the bolt using Eq. 4.4. The mean PGV required to break the bolt is 1.75 m/s with a standard deviation of 1.14 m/s. Due to the high standard deviation, this mean PGV required to break the bolt cannot be used as the upper bound on the PGV experienced by this location. Therefore, the range of the PGV required to cause the observed displacement of 32.5 – 36 cm is 0.5 – 2.5 m/s and 0.5 – 3 m/s for $\mu = 0.15$ and $\mu = 0.2$, respectively. This PGV range is very wide and therefore the upper bound on the PGV is meaningless. The lower bound on PGV of 0.5 m/s suggests that the modified mercalli intensity at this location is greater than VIII, which does not conflict with the results obtained for PGA.

This analysis shows that the observed sliding displacement of the rack can only provide meaningful lower bounds on ground motions experienced at a location. Higher friction coefficients between the rack and tile floor, which may induce sliding coupled with rocking of the rack, will not affect the lower bounds obtained from this analysis as higher PGA or PGV would be needed to be cause the observed sliding displacements. The fraction of the earthquake ground motion after which the battery rack becomes unbolted also does not affect the lower bound. However, the contribution of the collision between the rack S and N to the sliding displacement may alter the lower bounds.

The upper bounds obtained from the sliding analysis alone are unrealistically high. Even though an upper limit is obtained for PGA from the acceleration required to break properly installed bolts, this still results in a wide range for PGA and the analysis is able to provide only as much insight into the ground motion experienced by the region as can be obtained from MMI intensity of the earthquake.

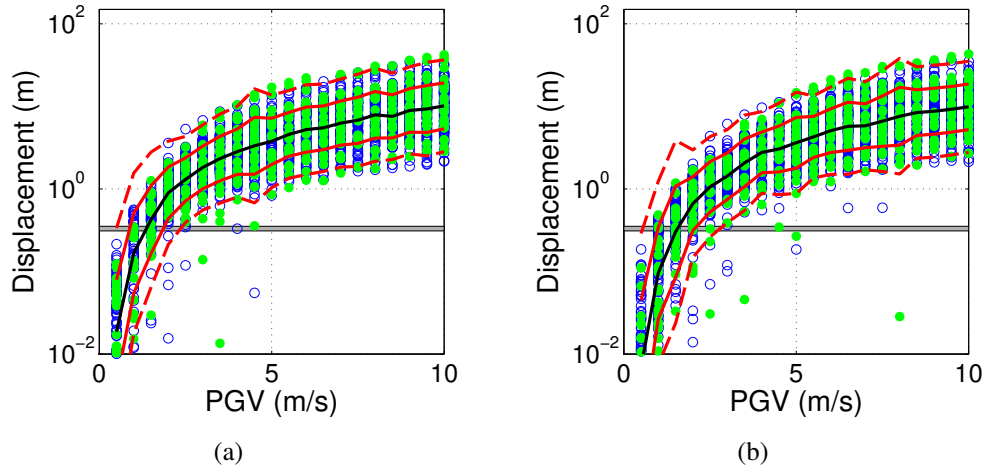


Figure 4.10: The maximum displacement of the battery rack when subjected to 140 earthquake records scaled to different PGV levels for (a) $\mu = 0.15$ and (b) $\mu = 0.2$. The green filled circles are the maximum effective displacement from earthquake records with $0.5 \text{ s} < T < 1.0 \text{ s}$. The black line shows the line joining mean e^ν , the red solid and dashed lines correspond to mean \pm one standard deviation ($e^{\nu \pm \sigma}$) and mean \pm two standard deviations ($e^{\nu \pm 2\sigma}$), respectively. The gray shaded region represents the observed displacement (0.325 – 0.36 m). The ranges of PGV required to cause the observed displacement are 0.5 – 2.5 m/s and 0.5 – 3.0 m/s for $\mu = 0.15$ and $\mu = 0.2$, respectively.

4.3 Estimating the minimum free-field PGA and PGV from maximum sliding displacement of nuclear spent fuel casks



(a)



(b)

Figure 4.11: (a) Spent fuel casks at the North Anna nuclear power plant and (b) photograph depicting sliding displacement of the cask after the 2011 Virginia earthquake [47].

The 2011 M_w 5.8 Mineral, Virginia earthquake caused 25 of the 27 spent fuel casks or dry casks of type TN-32 stored at the North Anna nuclear power plant to slide 1 – 4.5 in

or 0.025 – 0.115 m [Fig. 4.11(b)]. The storage casks are located approximately 18 km from the epicenter of the earthquake. The nearest strong ground motion was recorded at Unit 1 of the nuclear power plant using magnetic tape digital accelerographs. The recorded ground motions at the containment deck and the basement of Unit 1 had peak accelerations of 3.7 m/s² and 2.5 m/s², respectively, and peak velocities of 0.26 m/s and 0.13 m/s, respectively [42]. Unit 1 of the nuclear power plant is situated approximately 2000 ft from the location of the storage cask. Moreover, Unit 1 is founded on bedrock whereas the storage casks are founded on fine sand with bedrock starting 40 – 67 ft beneath the ground surface [93]. This difference in soil profile adds to the difficulty in estimating the free-field ground motion at the location of the storage cask. In the absence of free-field accelerograms, the sliding displacements of the dry casks are the sole constraints on the minimum free-field PGA and/or PGV experienced at this site.

The dry casks [Fig. 4.11(a)] are cylindrical in shape, with height 5.874 m and base radius 1.24 m, and are assumed to be rigid [76]. These casks rest on reinforced concrete pads of dimensions 224' × 32' × 2' [101] which are also assumed to be sufficiently rigid. The coefficient of friction ($\mu_s = \mu_d = \mu$) between the cask and the concrete pad is estimated to be between 0.2 and 0.8 from experimental studies on friction coefficient between steel and concrete [76]. Since the sliding displacements of casks were different, we only analyze the cask with the maximum sliding displacement of 0.115 m to arrive at the minimum free-field PGA and PGV. As we are interested in the minimum free-field PGA and PGV at this site, we assume that the cask exhibited pure sliding response. A higher PGA and PGV would be required to displace the cask if rocking/rolling about the edge is present. To prevent the cask from rocking, we assume the coefficient of friction to be in the lower end of the steel-concrete range ($\mu = 0.2$ and $\mu = 0.3$). The wide friction coefficient range of 0.2 – 0.8 between steel and concrete may have resulted in the different sliding displacements of the 25 casks. The base of the cask is discretized along the circumference into 4 equally spaced points, as this is sufficient to capture the sliding response. We analyze the model of the cask under the same set of 140 strong ground motion records as for the battery rack example. To estimate the PGA range, the ground motion records are normalized and scaled such that PGA varies from 1 m/s² to 20 m/s² in steps of 1 m/s². Unlike, the example of the battery

rack where the PGA required to break the bolts constrained the maximum PGA experienced by the location, we do not have any additional information to constrain the upper limit of the PGA. Therefore, we can only obtain realistic lower bounds on the ground motion at this location. Shown in Figs. 4.12(a) and 4.12(b) are the maximum displacements of the storage cask as a function of PGA. Here, the maximum displacement is the peak of the square root of sum of squares (SRSS) of the center of mass displacement time-histories in the two horizontal directions. As in the battery rack example, we consider earthquake records that produce responses within two standard deviations of the mean response (dashed red line) for obtaining the PGA and PGV values. The minimum PGAs required to cause the observed displacement of 0.115 m (dashed black line) are 3.5 m/s^2 and 5 m/s^2 for $\mu = 0.2$ and $\mu = 0.3$, respectively.

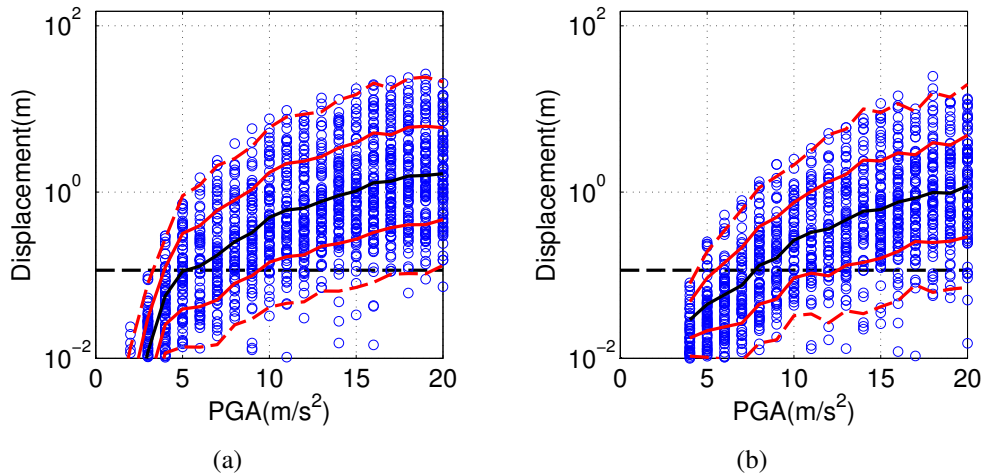


Figure 4.12: The maximum displacement of the storage cask when subjected to 140 earthquake records scaled to different PGA levels for (a) $\mu = 0.2$ and (b) $\mu = 0.3$. The black line shows the line joining mean e^ν , the red solid and dashed lines correspond to mean \pm one standard deviation ($e^{\nu \pm \sigma}$) and mean \pm two standard deviations ($e^{\nu \pm 2\sigma}$), respectively. The dashed black line is the observed displacement of 0.115 m. The minimum PGA required to cause the observed displacement is 3.5 m/s^2 and 5 m/s^2 for $\mu = 0.2$ and $\mu = 0.3$, respectively.

The analysis described above assumes that the concrete pad is rigid and that the ground motion is not amplified due to soil-structure interaction. However, in a parametric finite element analysis conducted by Bjorkman [19], for a concrete pad thickness of 2', clayey silt soil of 100 ft depth with shear wave velocity in the range of 500 – 900 m/s and concrete pad under full loading, the maximum amplification in the PGA experienced by the center

of mass of the cask with respect to the free-field PGA was 1.15. Since the pad thickness and soil conditions at the North Anna storage cask location are similar and the concrete pad was near maximum loading, we use the same amplification factor to get back the free-field PGA from our analysis. Therefore, the minimum free-field PGAs at the location of the storage casks required to cause the maximum observed sliding displacement of 0.115 m are 3 m/s^2 and 4.34 m/s^2 for $\mu = 0.2$ and $\mu = 0.3$, respectively.

In order to compare the free-field PGA at the storage cask location with the nearest ground motion recorded at the basement of Unit 1, we correct the free-field PGA for the difference in soil profiles. When an earthquake wave moves from bedrock to a lower velocity soil layer, the amplitude of the wave is in general amplified. We estimate this amplification factor using the equivalent linear method implemented in DEEPSOIL [46]. This program requires the depth of the soil layer, shear wave velocities and unit weight of the rock and soil layers as input. The values used for the depth, shear wave velocity and unit weight of the soil layer are 18.2 m, 500 m/s and 18.07 kN/m^3 , respectively. The shear wave velocity and unit weight used for the rock layer are 1500 m/s and 25.14 kN/m^3 , respectively. Additionally, the in-built shear modulus and damping ratio curves (Seed and Idriss mean limit 1991) are used for the soil layer. The amplification in PGA for 13 different ground motions are obtained and mean amplification factor of 1.38 is used for this analysis. This mean amplification factor relates the PGA at the soil layer to the PGA at the rock layer, which is same as the PGA at Unit 1. Therefore, the minimum free-field PGA at Unit 1 from our analysis is 2.17 m/s^2 and 3.14 m/s^2 for $\mu = 0.2$ and $\mu = 0.3$, respectively, which agrees well with the PGA of 2.5 m/s^2 recorded at the basement of Unit 1 [42].

To estimate the PGV at the storage cask location, we normalize the 140 ground motion records and scale them to PGV levels of 0.5 m/s – 10.0 m/s in steps of 0.5 m/s. $PGV = 0.25 \text{ m/s}$ is also considered. We analyze the cask model under these scaled records. Shown in Figs. 4.13(a) and 4.13(b) are the maximum effective displacements of the storage cask as a function of PGV. The minimum PGV required to cause the observed displacement (dashed black line) of 0.115 m is 0.5 m/s and 0.75 m/s for $\mu = 0.2$ and $\mu = 0.3$, respectively. Assuming that PGV amplifies similar to PGA due to soil-structure interaction and concrete pad flexibility, the minimum free-field PGV at the location of the

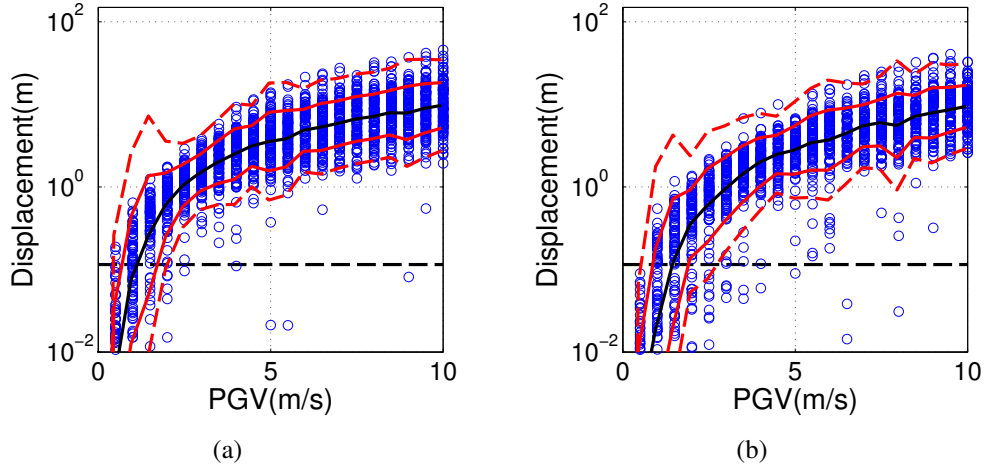


Figure 4.13: The maximum displacement of the storage cask when subjected to 140 earthquake records scaled to different PGV levels for (a) $\mu = 0.2$ and (b) $\mu = 0.3$. The black line shows the line joining mean e^ν , the red solid and dashed lines correspond to mean \pm one standard deviation ($e^{\nu \pm \sigma}$) and mean \pm two standard deviations ($e^{\nu \pm 2\sigma}$), respectively. The dashed black line corresponds to the observed displacement of 0.115 m. The minimum PGV required to cause the observed displacement is 0.5 m/s and 0.75 m/s for $\mu = 0.2$ and $\mu = 0.3$, respectively.

storage cask is 0.44 m/s and 0.65 m/s for $\mu = 0.2$ and $\mu = 0.3$, respectively. To compare the PGV obtained with the recorded PGV at the basement of Unit 1, we estimate the mean amplification in PGV using DEEPSOIL. This amplification factor is 1.39. Therefore, the free-field PGV at Unit 1 from our analysis is 0.32 m/s and 0.47 m/s for $\mu = 0.2$ and $\mu = 0.3$, respectively. The recorded PGV of 0.13 m/s at the basement of the Unit 1 is lower than our estimates. This difference suggests that the limits obtained on the free-field PGV may not be accurate.

4.4 Summary

In this chapter, we explore the problem of estimating the ground motion experienced at a region from qualitative information about the response of an object. For this study, we considered three different real world examples.

The first example was that of a train that overturned at Point Reyes station during the 1906 San Francisco earthquake. We obtained lower bounds on the ground motion experienced at the Point Reyes station during this earthquake by estimating the ground motion

parameters required to overturn a rectangular block model of this train. The minimum PGA, PGV, and PGD required to overturn the train are 4 m/s^2 , 1 m/s , and 0.25 m , respectively. The probability of overturning is quite low when the PGV is below 1 m/s but goes up quite rapidly when the PGV exceeds this value. The train model is also seen to be sensitive to earthquake records with predominant time periods near 1.6 s . It was also observed that the PGV required to overturn the rock model is more or less independent of the duration of the earthquake. However, the PGA required to overturn the rock model decreases more or less uniformly with duration.

The fragility (overturning probability) maps for the train model are used to perform a reality check on the synthetic ground motion at Point Reyes from the 1906-like San Francisco earthquake simulations by Aagaard et al. The maps indicate overturning probabilities of 0.4-0.8 for the train model under the predicted ground motion intensities from three rupture scenarios (with hypocenters in Bodega Bay to the north of Point Reyes and offshore from San Francisco and San Juan Bautista, both to the south of Point Reyes). Clearly, the predictions by the Aagaard et al. simulations are quite realistic. Time history analysis of the train model under synthetic ground motion histories at Point Reyes from the three scenarios shows the train model overturning in all three cases. However, only the ground motions from the two scenarios with the hypocenter to the south of Point Reyes reproduce the eye-witness account of the train lurching to the east and then to the west before toppling. We conclude that the hypocenter for the 1906 San Francisco earthquake must lie to the south of Point Reyes, perhaps offshore from San Francisco as widely believed.

In the next example, we analyzed a battery rack that underwent sliding during the Haiti earthquake of 2010 and estimated the lower bound on the PGA experienced at this location to be 3 m/s^2 and 4 m/s^2 for friction coefficients of 0.15 and 0.2, respectively. The corresponding estimates for the lower bounds on the PGV experienced at this location are 0.5 m/s^2 for friction coefficients of 0.15 and 0.2. We showed that realistic upper bounds on PGA or PGV cannot be obtained from the sliding analysis of the battery rack.

In the last example, we analyzed a nuclear storage canister that underwent sliding during the 2011 Mineral, Virginia earthquake and estimated the minimum free-field PGA experienced at that site to be 3 m/s^2 and 4.34 m/s^2 for friction coefficients of 0.2 and 0.3,

respectively. These PGA values compare well with the nearest recorded ground motions.

From this analysis, we conclude that only lower bounds on the ground motions experienced at a region can be obtained from sliding displacement or overturning of an object under earthquake excitation.

Chapter 5

Conclusions and future work

5.1 Conclusions

This dissertation has been motivated by the prospect of using precariously balanced rocks (PBRs) to provide an independent constraint on historic peak ground motion experienced by a region. To achieve this goal the critical toppling intensity of a PBR needs to be accurately estimated. Earlier approaches to estimate this critical toppling intensity approximate the 3-D rock-pedestal geometry to a simple 2-D geometry resting on a plane at two contact points. An empirical equation [88] is then applied to the parameters of the 2-D rock geometry to obtain overturning probability of the rock as a function of ground motion intensity measures. Shake table experiments suggest that this approach under-predicts the fragility of most rocks, accentuating the need for dynamic analysis of 3-D rock-pedestal models. To this end, we have developed a methodology to create 3-D models of PBRs and their supporting pedestals and to analyze them under three-component earthquake ground excitation.

We approximated the rock and pedestal to two separate 3-D rigid bodies and we developed an algorithm to simulate the interaction between the rock and the pedestal. This algorithm is a fairly generic algorithm that is capable of modeling the complex sliding and rocking response of the rock. Constraint based method is used to model the contact between the rock and the pedestal, with external accelerations being balanced by contact forces. Thus, rock-pedestal interpenetration (to within a user-specified tolerance) is automatically avoided even without the use of spring-damper assemblies. The algorithm is

validated against analytical results for the rocking and coupled rocking-sliding response of a simple 2-D rectangular block.

The accuracy of the rigid body algorithm in analyzing the 3-D rock models is then established through comparisons against shake-table tests on rocks conducted by Purvance et al. [88]. Fragility maps are then developed for the Echo Cliff PBR and the Pacifico PBR by analyzing the rock under ground motions from 140 earthquakes. The Echo Cliff PBR is located in the Western Santa Monica mountains and the Pacifico PBR is located approximately 12 km from the San Andreas Fault. The fragility maps generated from this analysis contain information about the dependence of the overturning probability of the rocks on the ground motion intensity measures like peak ground acceleration (PGA), peak ground velocity (PGV), peak ground displacement (PGD), and duration of ground excitation. From this analysis, we infer that the overturning probability of the Echo Cliff PBR is quite low for PGA and PGV below 3 m/s^2 and 0.75 m/s , respectively. Similarly, the overturning probability of the Pacifico rock is quite low for PGA and PGV below 4 m/s^2 and 0.5 m/s , respectively. But PGDs lower than 0.25 m are also capable of overturning both these rocks.

The effect of the directionality of ground excitation and rock-pedestal interface friction coefficient on the overturning probability of the two PBRs was also explored. The overturning probabilities and the direction in which both the PBRs overturned was more or less independent of the direction in which the strong component of the ground motion was applied because of two reasons: (i) half of the records selected for the study did not exhibit strong directionality and (ii) both the rocks have a preferred direction of overturning. The preferred overturning direction for the Echo Cliff PBR is governed by a major fraction of the base of the rock extending beyond the edge of the cliff as an overhang. The Pacifico rock, on the other hand, is slender along one direction and this governs the direction of overturning for this rock. Both the rocks rest on a downward sloping pedestal which is more or less aligned with the preferred overturning direction of the rock. Therefore, lower friction coefficient of 0.6 between the rock and pedestal led to higher overturning probabilities in both rocks when compared to friction coefficient of 1.0.

We use the fragility maps generated from this study to test the seismic hazard predic-

tions obtained at the PBR locations from the national seismic hazard maps (for the Echo Cliff PBR) and vector-valued probabilistic seismic hazard analysis (for Pacifico rock). The seismic hazard at both these locations are over-predicted. We also perform a reality check on the Southern California ShakeOut scenario and other synthetic ground motion simulations rupturing segments of the San Andreas Fault by verifying that the ground motions at the location of the PBR do not topple the PBR.

Apart from analyzing the response of PBRs to ground excitation, we also estimate the ground motion experienced at a region from qualitative information about the rocking/sliding response of an object. A train overturned at Point Reyes station during the 1906 San Francisco earthquake. We obtained lower bounds on the ground motion experienced at the Point Reyes station during this earthquake by estimating the ground motion parameters required to overturn a rectangular block model of this train. The minimum PGA, PGV, and PGD required to overturn the train are 4 m/s^2 , 1 m/s and 0.25 m , respectively. The fragility (overturning probability) maps for the train model were also used to perform a reality check on the synthetic ground motion at Point Reyes from the 1906-like San Francisco earthquake simulations by Aagaard et al. Time history analysis of the train model under synthetic ground motion histories at Point Reyes from the three scenarios (with hypocenters in Bodega Bay to the north of Point Reyes and offshore from San Francisco and San Juan Bautista, both to the south of Point Reyes) shows the train model overturns in all three cases. However, only the ground motions from the two scenarios with the hypocenter to the south of Point Reyes reproduce the eye-witness account of the train lurching to the east and then to the west before toppling. We conclude that the hypocenter for the 1906 San Francisco earthquake must lie to the south of Point Reyes, perhaps offshore from San Francisco as widely believed.

Finally, we analyze the sliding response of objects like battery racks (which underwent sliding during 2010 Haiti earthquake) and nuclear storage canister (which underwent sliding during 2011 Mineral, Virginia earthquake) to estimate the lower bounds on ground motions experienced at these regions. We found that the lower bound on PGA was quite sensitive to the friction coefficient. For example, the lower bound experienced at the site of the battery rack was 3 m/s^2 and 4 m/s^2 for friction coefficients of 0.15 and 0.2, respectively,

between the battery rack and the floor. Similarly, the lower bounds on PGA at the nuclear storage canister site was 3 m/s^2 and 4.34 m/s^2 for friction coefficients of 0.2 and 0.3, respectively. The lower bounds on PGV, on the other hand, were not significantly affected by the friction coefficients.

Earlier research on PBRs concluded that the rocking response of PBRs and the rectangular train model can provide constraints on PGA at that location. From this study, we conclude that the overturning probability of the rock/rectangular block is most sensitive to PGV. A minimum PGA is required to initiate rocking response of the rock/rectangular block but if the PGV is less than a threshold, then the rocking response damps out quickly. We also concluded that overturning analysis of train and sliding analysis of battery rack and canister provide only lower bounds on ground motion experienced at the region. Since the PBRs have not yet overturned, they provide an upper bound instead of lower bound on the peak historic ground motion at that location.

5.2 Future Work

The approach presented in this dissertation can be extended to create accurate fragility maps for the many rocks cataloged by Brune et al. [26] in order to obtain region-wide seismic hazard assessment for Southern California. The comparisons with vector-valued probabilistic seismic hazard analysis detailed in Section 3.6.2 may also be employed to test the accuracy of the different ground motion prediction models. We have used the Campbell-Bozorgnia NGA ground motion attenuation model [28], but the same analysis can be repeated using other NGA attenuation relations like those developed Abrahamson and Silva [6], Boore and Atkinson [20], Idriss [55], and so on. Note that this approach can only judge whether the ground motion model is consistent with the existence of the PBR.

Apart from the use of the rigid body dynamics algorithm to analyze precariously balanced rocks, this algorithm may be used to simulate the falling of rocks. Any rock-fall simulation involves modeling the rolling, sliding and bouncing of rocks on a slope. This analysis is further complicated by the irregular shape of the rock. The algorithm developed for the analysis of PBRs is well suited to solve this problem. The results from this simula-

tion might help in judging the appropriate height and location of fence required to prevent the rock from rolling onto a road.

The existing rigid body dynamics algorithm may also be extended to model the response of multi-body systems such as the stacked column structures found in Greece and linked structures such as robotic arms.

Appendices

Appendix A

Feasibility of LCP

In this appendix, we demonstrate that the LCP in Eq. 2.16 is feasible, i.e., there exists a \mathbf{j}_n^{p+1} satisfying all the inequality constraints. Say, the normal vector \mathbf{n}_α (size 1×3) at all contact points ($\alpha = 1, 2, \dots, q$) are arranged into the matrix \mathbf{J} of size $q \times 3$. Similarly, say the row vectors $\mathbf{r}_\alpha \times \mathbf{n}_\alpha$ (size 1×3) at all contact points are arranged into the matrix \mathbf{K} . Then, from the definition of the \mathbf{C}_{nn} in Eq. 2.15, \mathbf{C}_{nn} can be rewritten as:

$$\mathbf{C}_{nn} = \frac{1}{m} \mathbf{J} \mathbf{J}^T + \mathbf{K} \mathbf{I}^{-1} \mathbf{K}^T \quad (\text{A.1})$$

Now, from Farkas's alternative [38], either there exists a non-negative \mathbf{j}_n^{p+1} satisfying $\mathbf{j}_n^{p+1} \mathbf{C}_{nn} + \mathbf{d}'_n \geq \mathbf{0}$, or there exists a positive row vector \mathbf{h} (size $1 \times q$) satisfying $-\mathbf{h} \mathbf{C}_{nn} \geq \mathbf{0}$ and $\mathbf{h} \cdot \mathbf{d}'_n < 0$ (where \cdot represents element-wise multiplication). Say there exists a \mathbf{h} meeting the specified requirements. Since \mathbf{h} is a positive vector, $-\mathbf{h} \mathbf{C}_{nn} \mathbf{h}^T \geq 0$. However, \mathbf{C}_{nn} is positive semi-definite. Therefore, $\mathbf{h} \mathbf{C}_{nn} \mathbf{h}^T = 0$. Now substituting for \mathbf{C}_{nn} from Eq. A.1, we get:

$$\begin{aligned} \mathbf{h} \mathbf{C}_{nn} \mathbf{h}^T = 0 &\implies \mathbf{h} \left(\frac{1}{m} \mathbf{J} \mathbf{J}^T + \mathbf{K} \mathbf{I}^{-1} \mathbf{K}^T \right) \mathbf{h}^T = 0 \\ &\implies \frac{1}{m} \mathbf{h} \mathbf{J} \mathbf{J}^T \mathbf{h}^T + \mathbf{h} \mathbf{K} \mathbf{I}^{-1} \mathbf{K}^T \mathbf{h}^T = 0 \\ &\implies \frac{1}{m} \|\mathbf{J}^T \mathbf{h}^T\|^2 + (\mathbf{K}^T \mathbf{h}^T)^T \mathbf{I}^{-1} (\mathbf{K}^T \mathbf{h}^T) = 0 \end{aligned}$$

Since moment of inertia, \mathbf{I} , is positive definite:

$$\mathbf{h}\mathbf{C}_{\text{nn}}\mathbf{h}^T = 0 \implies \mathbf{J}^T\mathbf{h}^T = \mathbf{0}; \quad \mathbf{K}^T\mathbf{h}^T = \mathbf{0}$$

From the definition of \mathbf{J} :

$$\mathbf{J}^T\mathbf{h}^T = \mathbf{0} \implies \sum_{\alpha=1}^q \mathbf{n}_{\alpha}^T h_{\alpha} = 0$$

Here, h_{α} is the α^{th} element of the vector \mathbf{h} . In the types of problems we are considering, the vertical component (i.e., global Z) of the outward normal vector to the pedestal surface at all contact points is positive. Since \mathbf{h} is also a positive vector, $\sum_{\alpha=1}^q \mathbf{n}_{\alpha}^T h_{\alpha}$ can never be zero. Therefore, a positive vector \mathbf{h} (size $1 \times q$) satisfying $-\mathbf{h}\mathbf{C}_{\text{nn}} \geq \mathbf{0}$ and $\mathbf{h} \cdot \mathbf{d}'_{\text{n}} < \mathbf{0}$ does not exist. The non-existence of \mathbf{h} mandates the existence of a non-negative $\mathbf{j}_{\text{n}}^{p+1}$ satisfying $\mathbf{j}_{\text{n}}^{p+1}\mathbf{C}_{\text{nn}} + \mathbf{d}'_{\text{n}} \geq \mathbf{0}$, thereby ensuring the feasibility of the LCP.

Appendix B

Analytical solution for block's response mode

Say a rigid rectangular block of mass m [Fig. B.1(a)] impacts the ground. Let \dot{u}_y and \dot{u}_x be the vertical and horizontal translational velocities of the block's center of mass, respectively, just before impacting the ground. Assuming that the coefficient of restitution (e) between the block and the ground is zero, the block may come to rest, may start to rock, may slide, or may experience sliding coupled with rocking after impact with the ground. Here, we derive the conditions on the initial velocities (\dot{u}_y and \dot{u}_x) and the friction coefficient (μ) between the block and the ground required to initiate response of the block in each mode. For all calculations performed in this section, the static and kinetic friction coefficients are assumed to be the same and the block is assumed to have negative vertical velocity and positive horizontal velocity before impact, i.e., $\dot{u}_y \leq 0$ and $\dot{u}_x \geq 0$, respectively.

Say \dot{u}_y^+ and \dot{u}_x^+ are the vertical and horizontal translational velocities of the block's center of mass, respectively, after impact with the ground. Similarly, let $\omega^- = 0$ and ω^+ be the angular velocity of the block before and after impact, respectively, about the z axis passing through its center of mass. Let j_{n1} and j_{n2} be the normal impulses acting at contact points O_1 and O_2 , respectively, and j_{x1} and j_{x2} be the frictional impulses acting at contact points O_1 and O_2 , respectively.

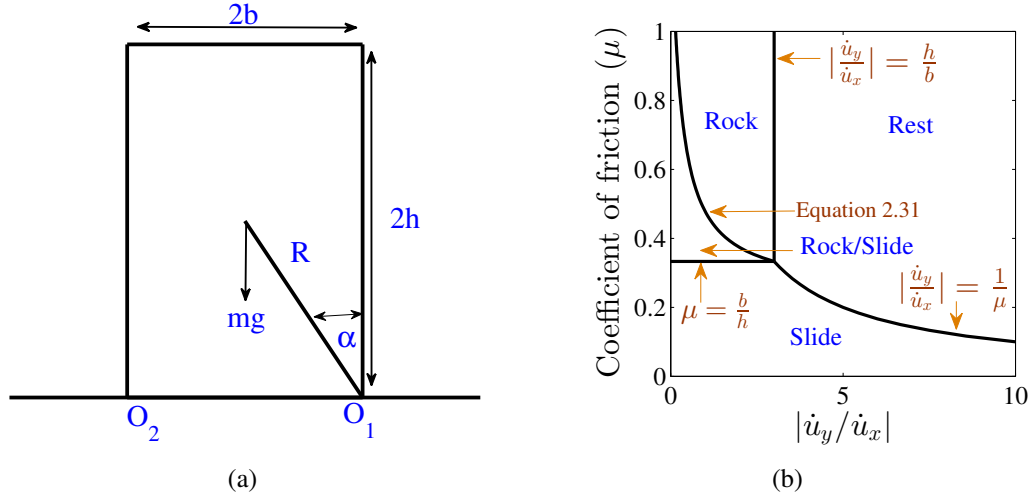


Figure B.1: (a) Rigid rectangular block and ground (b) motion of block after it impacts the ground as a function of initial velocity and coefficient of friction.

Case 1: Impact to rest

If the block comes to rest after impact, then \dot{u}_y^+ , \dot{u}_x^+ , and ω^+ are zero. Conservation of linear and angular momentum gives:

$$m\dot{u}_y^+ = m\dot{u}_y + j_{n1} + j_{n2} \implies j_{n1} + j_{n2} = -m\dot{u}_y \quad (\text{B.1})$$

$$m\dot{u}_x^+ = m\dot{u}_x + j_{x1} + j_{x2} \implies j_{x1} + j_{x2} = -m\dot{u}_x \quad (\text{B.2})$$

$$I\omega^+ = b(j_{n1} - j_{n2}) + h(j_{x1} + j_{x2}) \implies j_{n1} - j_{n2} = -\frac{h}{b}(j_{x1} + j_{x2})$$

Solving these equation gives:

$$j_{n1} = -\frac{1}{2}m\dot{u}_y + \frac{h}{2b}m\dot{u}_x$$

$$j_{n2} = -\frac{1}{2}m\dot{u}_y - \frac{h}{2b}m\dot{u}_x$$

For $\dot{u}_y < 0$ and $\dot{u}_x > 0$, the normal impulse at contact point O_1 is greater than that at O_2 , i.e., $j_{n1} > j_{n2}$. Since the normal impulses can only push the block and ground away from each other and not pull them towards each other, we require the normal impulses to

be non-negative. This gives:

$$j_{n2} \geq 0 \implies -\frac{\dot{u}_y}{\dot{u}_x} \geq \frac{h}{b} \implies \left| \frac{\dot{u}_y}{\dot{u}_x} \right| \geq \frac{h}{b}$$

Next, the friction impulses should satisfy Coulomb's friction law, i.e., $|j_{x1}| \leq \mu j_{n1}$ and $|j_{x2}| \leq \mu j_{n2}$. Assume that both the friction impulses oppose the horizontal tangential velocity of the block, i.e., $j_{x1} \leq 0$ and $j_{x2} \leq 0$. The Coulomb's friction cone constraint combined with Eqs. B.1 and B.2 yields:

$$\begin{aligned} m\dot{u}_x &= |j_{x1}| + |j_{x2}| \leq \mu(j_{n1} + j_{n2}) = -\mu m\dot{u}_y \\ \implies \frac{1}{\mu} &\leq \left| \frac{\dot{u}_y}{\dot{u}_x} \right| \end{aligned}$$

Now, say $j_{x2} \geq 0$ and $j_{x1} \leq 0$, then the Coulomb's friction cone constraint combined with Eqs. B.1 and B.2 gives:

$$\left. \begin{aligned} j_{x2} + m\dot{u}_x &= |j_{x1}| \leq \mu j_{n1} \implies j_{x2} \leq \mu j_{n1} - m\dot{u}_x \\ j_{x2} &\leq \mu j_{n2} \end{aligned} \right\} \implies \frac{1}{\mu} \leq \left| \frac{\dot{u}_y}{\dot{u}_x} \right|$$

The same constraint is obtained when $j_{x2} \geq 0$ and $j_{x1} \leq 0$. Therefore, the conditions on μ and $|\dot{u}_y/\dot{u}_x|$ required for the block to come to rest after impact are:

$$\frac{1}{\mu} \leq \left| \frac{\dot{u}_y}{\dot{u}_x} \right|; \quad \frac{h}{b} \leq \left| \frac{\dot{u}_y}{\dot{u}_x} \right|$$

Case 2: Impact to sliding

If the block slides after impact, then \dot{u}_y^+ and ω^+ are zero, whereas \dot{u}_x^+ is positive. Conservation of linear and angular momentum gives:

$$m\dot{u}_y^+ = m\dot{u}_y + j_{n1} + j_{n2} \implies j_{n1} + j_{n2} = -m\dot{u}_y \quad (\text{B.3})$$

$$m\dot{u}_x^+ = m\dot{u}_x + j_{x1} + j_{x2} \implies j_{x1} + j_{x2} = m(\dot{u}_x^+ - \dot{u}_x) \quad (\text{B.4})$$

$$I\omega^+ = b(j_{n1} - j_{n2}) + h(j_{x1} + j_{x2}) \implies j_{n1} - j_{n2} = -\frac{h}{b}(j_{x1} + j_{x2}) \quad (\text{B.5})$$

Now, Coulomb's friction law requires that the friction impulses oppose the translational velocity of the block and lie on the friction cone, i.e., $j_{x1} = -\mu j_{n1}$ and $j_{x2} = -\mu j_{n1}$. Solving Eqs. B.4 and B.5 along with the relations from the friction law gives:

$$j_{n1} = -\frac{1}{2}m\dot{u}_y \left(1 + \mu\frac{h}{b}\right)$$

$$j_{n2} = -\frac{1}{2}m\dot{u}_y \left(1 - \mu\frac{h}{b}\right)$$

As earlier, the normal impulses j_{n1} and j_{n2} have to be non-negative. The above expressions show that $j_{n1} > j_{n2}$ for $\dot{u}_y < 0$. Therefore:

$$j_{n2} \geq 0 \implies \mu \leq \frac{b}{h}$$

Next, Eqs. B.3 and B.4 combined the relations from the friction law may be used to calculate \dot{u}_x^+ . The resulting equation for expression for \dot{u}_x^+ is:

$$\dot{u}_x^+ = \dot{u}_x + \mu\dot{u}_y > 0 \implies \frac{1}{\mu} > \left| \frac{\dot{u}_y}{\dot{u}_x} \right|$$

Therefore, the conditions on μ and $|\dot{u}_y/\dot{u}_x|$ required for the block to slide after impact are:

$$\mu \leq \frac{b}{h}; \quad \frac{1}{\mu} > \left| \frac{\dot{u}_y}{\dot{u}_x} \right|$$

Case 3: Impact to rocking

If the block rocks after impact, then \dot{u}_y^+ and \dot{u}_x^+ are positive whereas ω^+ is negative. Since the block starts rocking about O_1 , the contact impulses at the O_2 are zero, i.e., $j_{n2} = 0$ and $j_{x2} = 0$. Conservation of linear and angular momentum gives:

$$m\dot{u}_y^+ = m\dot{u}_y + j_{n1} \implies \dot{u}_y^+ = \dot{u}_y + \frac{1}{m}j_{n1} \quad (\text{B.6})$$

$$m\dot{u}_x^+ = m\dot{u}_x + j_{x1} \implies \dot{u}_x^+ = \dot{u}_x + \frac{1}{m}j_{x1} \quad (\text{B.7})$$

$$I\omega^+ = bj_{n1} + hj_{x1} \implies \omega^+ = \frac{1}{I}(bj_{n1} + hj_{x1}) \quad (\text{B.8})$$

Here, the moment of inertia, I , for the block about its center of mass is $m(b^2 + h^2)/3$. Additionally, the block rocking about O_1 implies that the horizontal and vertical velocities of that contact point after impact, \dot{u}_{x1} and \dot{u}_{y1} , respectively, are zero. These velocities are given by:

$$\begin{aligned}\dot{u}_{x1} = \dot{u}_x^+ + h\omega^+ = 0 &\implies \dot{u}_x^+ = -h\omega^+ \\ \dot{u}_{y1} = \dot{u}_y^+ + b\omega^+ = 0 &\implies \dot{u}_y^+ = -b\omega^+\end{aligned}$$

These above equations along with Eqs. B.6-B.8 can be solved simultaneously to arrive at:

$$\begin{aligned}j_{x1} = \frac{m}{4(b^2 + h^2)}[3bh\dot{u}_y - (4b^2 + h^2)\dot{u}_x]; \quad j_{n1} = \frac{m}{4(b^2 + h^2)}[3bh\dot{u}_x - (b^2 + 4h^2)\dot{u}_y] \\ \dot{u}_x^+ = \frac{3h}{4(b^2 + h^2)}(b\dot{u}_y + h\dot{u}_x); \quad \dot{u}_y^+ = \frac{3b}{4(b^2 + h^2)}(b\dot{u}_y + h\dot{u}_x)\end{aligned}\tag{B.9}$$

$$\omega^+ = \frac{3}{4(b^2 + h^2)}(b\dot{u}_y + h\dot{u}_x)\tag{B.10}$$

The above solutions for j_{x1} and j_{n1} should satisfy the static Coulomb friction law and $j_{n1} \geq 0$. The solution for j_{n1} shows that it is always positive for $\dot{u}_x \geq 0$ and $\dot{u}_y \leq 0$. Similarly, the solution for j_{x1} shows that $j_{x1} \leq 0$. The static friction cone constraint gives:

$$|j_{x1}| \leq \mu j_{n1} \implies \frac{4 + \frac{h^2}{b} - 3\mu\frac{h}{b}}{\mu(1 + 4\frac{h^2}{b}) - 3\frac{h}{b}} \leq \left| \frac{\dot{u}_y}{\dot{u}_x} \right|$$

The solution for ω^+ should be negative. This gives:

$$\omega^+ < 0 \implies \left| \frac{\dot{u}_y}{\dot{u}_x} \right| < \frac{h}{b}$$

Therefore, the conditions on μ and $|\dot{u}_y/\dot{u}_x|$ required for the block to rock after impact are:

$$\frac{4 + \frac{h^2}{b} - 3\mu\frac{h}{b}}{\mu(1 + 4\frac{h^2}{b}) - 3\frac{h}{b}} \leq \left| \frac{\dot{u}_y}{\dot{u}_x} \right|; \quad \left| \frac{\dot{u}_y}{\dot{u}_x} \right| < \frac{h}{b}$$

Case 4: Impact to sliding coupled with rocking

If the block slides as well as rocks after impact, then \dot{u}_y^+ and \dot{u}_x^+ are positive whereas ω^+ is negative. Since the block starts rocking about O_1 , the contact impulses at the O_2 are zero, i.e., $j_{n2} = 0$ and $j_{x2} = 0$. Conservation of linear and angular momentum gives:

$$m\dot{u}_y^+ = m\dot{u}_y + j_{n1} \implies \dot{u}_y^+ = \dot{u}_y + \frac{1}{m}j_{n1} \quad (\text{B.11})$$

$$m\dot{u}_x^+ = m\dot{u}_x + j_{x1} \implies \dot{u}_x^+ = \dot{u}_x + \frac{1}{m}j_{x1} \quad (\text{B.12})$$

$$I\omega^+ = bj_{n1} + hj_{x1} \implies \omega^+ = \frac{1}{I}(bj_{n1} + hj_{x1}) \quad (\text{B.13})$$

Here, the moment of inertia, I , for the block about its center of mass is $m(b^2 + h^2)/3$. Additionally, the block rocking and sliding about O_1 implies that the vertical velocity of that contact point after impact, \dot{u}_{y1} , is zero. The velocities of contact point O_1 are given by:

$$\begin{aligned} \dot{u}_{x1} &= \dot{u}_x^+ + h\omega^+ \\ \dot{u}_{y1} &= \dot{u}_y^+ + b\omega^+ = 0 \implies \dot{u}_x^+ = -h\omega^+ \end{aligned} \quad (\text{B.14})$$

The friction impulse at O_1 should oppose the horizontal velocity of the contact point and should lie on the friction cone, i.e., $j_{x1} = -\mu j_{n1}$. Substituting this information into Eq. B.14 gives:

$$j_{n1} = -\frac{m(b^2 + h^2)}{4b^2 + h^2 - 3\mu hb}\dot{u}_y$$

The normal impulse should be non-negative. This gives:

$$j_{n1} \geq 0 \implies \frac{4b^2 + h^2}{3hb} \geq \mu$$

The solution for the normal impulse can be used to solve for the other unknown quantities:

$$\dot{u}_x^+ = \dot{u}_x - \frac{\mu(b^2 + h^2)}{4b^2 + h^2 - 3\mu hb} \dot{u}_y; \quad \dot{u}_y^+ = \frac{3b}{4b^2 + h^2 - 3\mu hb} (b - \mu h) \dot{u}_y \quad (\text{B.15})$$

$$\omega^+ = \frac{3}{4b^2 + h^2 - 3\mu hb} (b - \mu h) \dot{u}_y \quad (\text{B.16})$$

$$\dot{u}_{x1} = \dot{u}_x + \frac{\mu(b^2 + 4h^2) - 3bh}{4b^2 + h^2 - 3\mu hb} \dot{u}_y$$

The rotational velocity of the block after impact (ω^+) is negative and the horizontal velocity of the contact point O_1 (\dot{u}_{x1}) after impact is positive. This gives:

$$\begin{aligned} \omega^+ < 0 &\implies \frac{b}{h} \leq \mu \\ \dot{u}_{x1} > 0 &\implies \frac{4 + \frac{h^2}{b} - 3\mu \frac{h}{b}}{\mu(1 + 4\frac{h^2}{b}) - 3\frac{h}{b}} > \left| \frac{\dot{u}_y}{\dot{u}_x} \right| \end{aligned}$$

There are two bounds for μ . The upper and lower bounds for μ are obtained from $j_{n1} \geq 0$ and $\omega^+ < 0$, respectively. However, for a h/b of 3 considered in the example above, the upper bound on μ is above 1. So, it does not play a significant role in constraining the region where sliding coupled with rocking occurs in the in $\mu - |\dot{u}_y/\dot{u}_x|$ space. Therefore, the conditions on μ and $|\dot{u}_y/\dot{u}_x|$ required for the block to slide and rock after impact are:

$$\frac{4 + \frac{h^2}{b} - 3\mu \frac{h}{b}}{\mu(1 + 4\frac{h^2}{b}) - 3\frac{h}{b}} > \left| \frac{\dot{u}_y}{\dot{u}_x} \right|; \quad \frac{b}{h} \leq \mu$$

Appendix C

Supplemental figures for Echo Cliff PBR

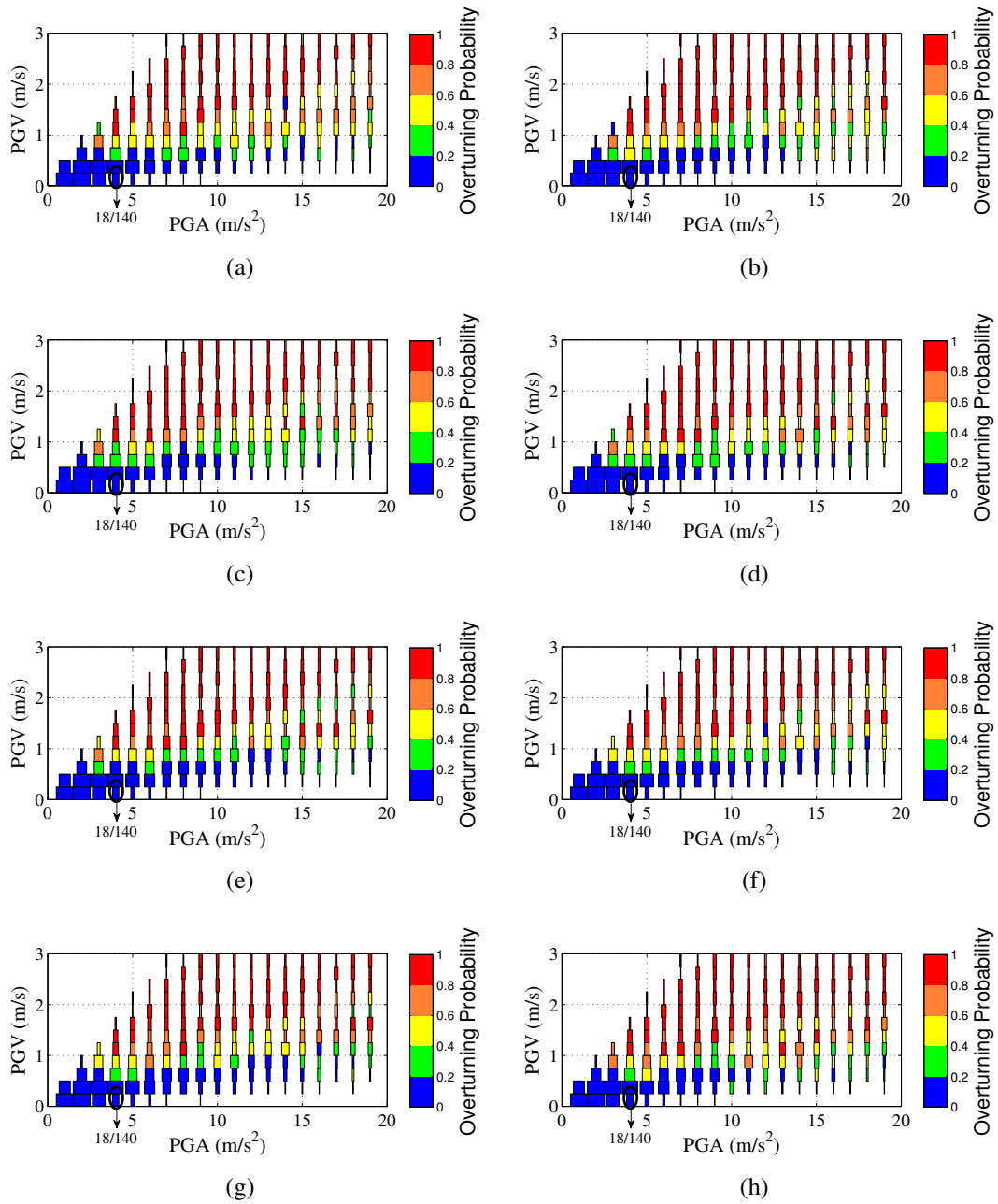


Figure C.1: Overturning probability of the Echo Cliff PBR as a function of PGV and PGA for dominant horizontal ground motion applied to the pedestal at (a) 0° , (b) 45° , (c) 90° , (d) 135° , (e) 180° , (f) 225° , (g) 270° , and (h) 315° CCW from the X axis. Each column in these figures contain 140 earthquakes scaled to a given PGA level. The varying thicknesses of the column are proportional to the fraction of earthquakes (out of 140) that are sampled in a given PGV bin.

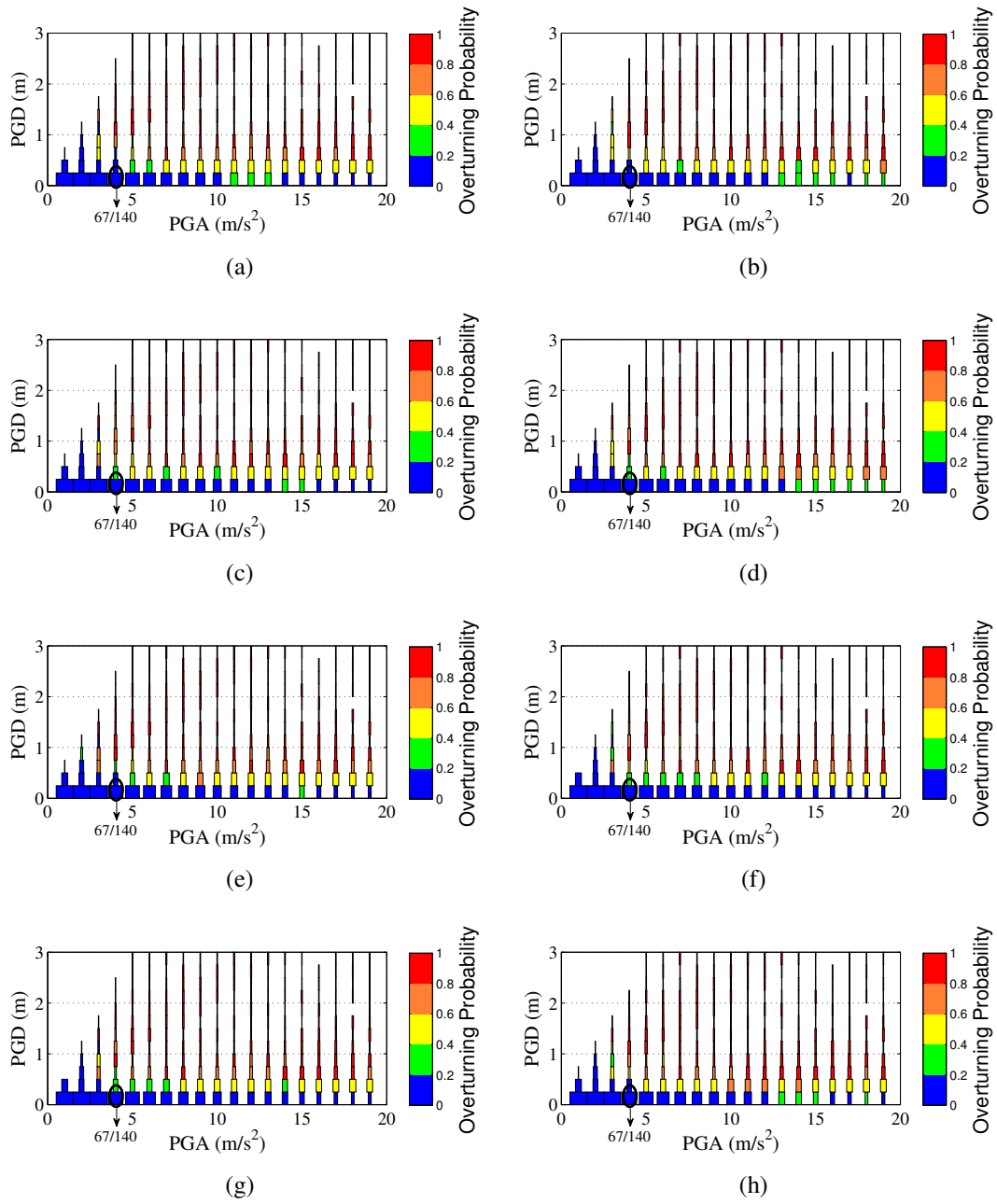


Figure C.2: Overturning probability of the Echo Cliff PBR as a function of PGD and PGA for dominant horizontal ground motion applied to the pedestal at (a) 0° , (b) 45° , (c) 90° , (d) 135° , (e) 180° , (f) 225° , (g) 270° , and (h) 315° CCW from the X axis. Each column in these figures contain 140 earthquakes scaled to a given PGA level. The varying thicknesses of the column are proportional to the fraction of earthquakes (out of 140) that are sampled in a given PGD bin.

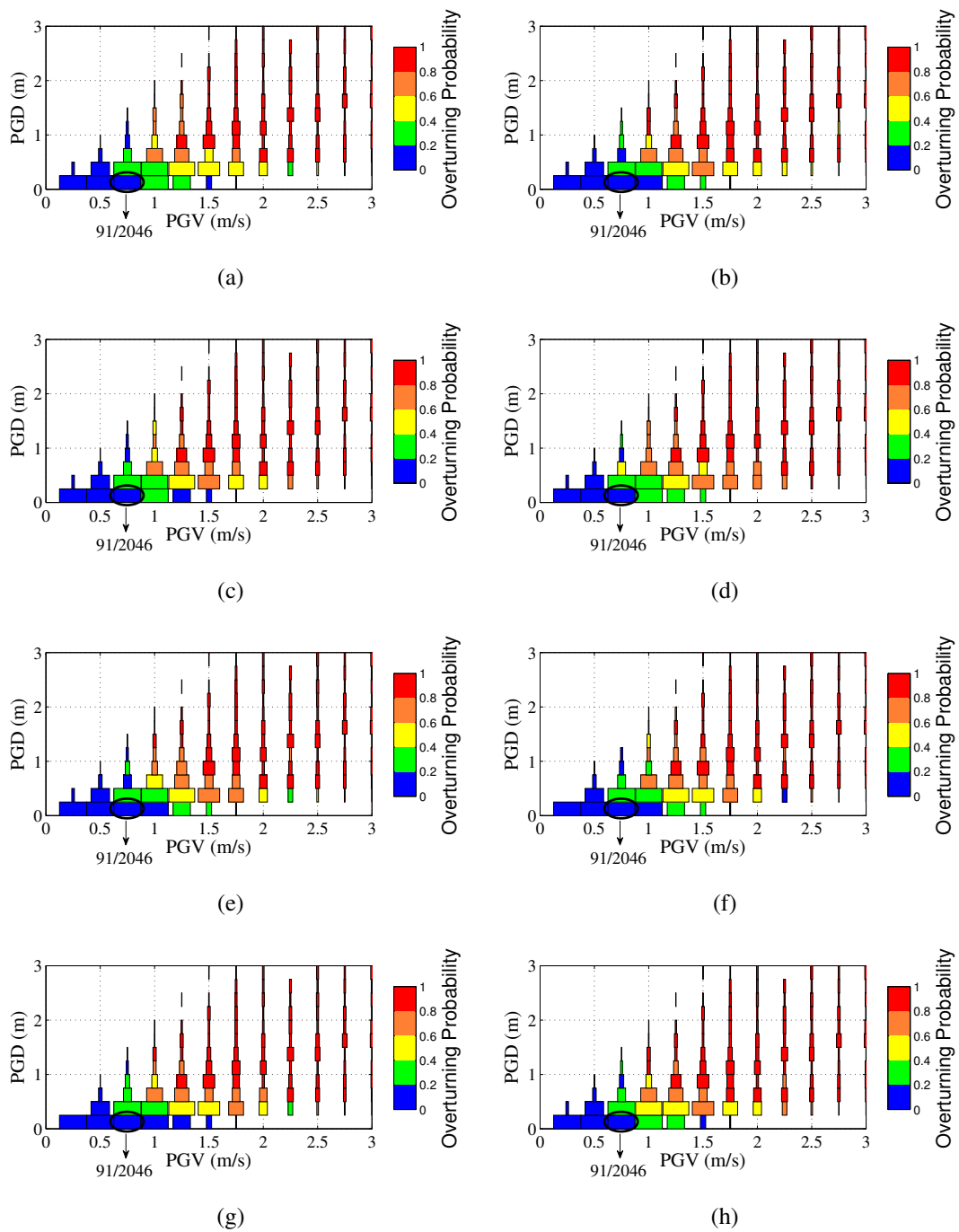


Figure C.3: Overturning probability of the Echo Cliff PBR as a function of PGD and PGV for dominant horizontal ground motion applied to the pedestal at (a) 0° , (b) 45° , (c) 90° , (d) 135° , (e) 180° , (f) 225° , (g) 270° , and (h) 315° CCW from the X axis. 2046 out of the 2660 scaled earthquake records which have PGV and PGD less than 3 m/s and 3 m, respectively, are used for these figures. The 2046 earthquakes are divided into bins of width 0.25 m/s in PGV and 0.25 m in PGD. The varying thicknesses of the column are proportional to the fraction of earthquakes (out of 2046) that are sampled in a given PGV and PGD bin.

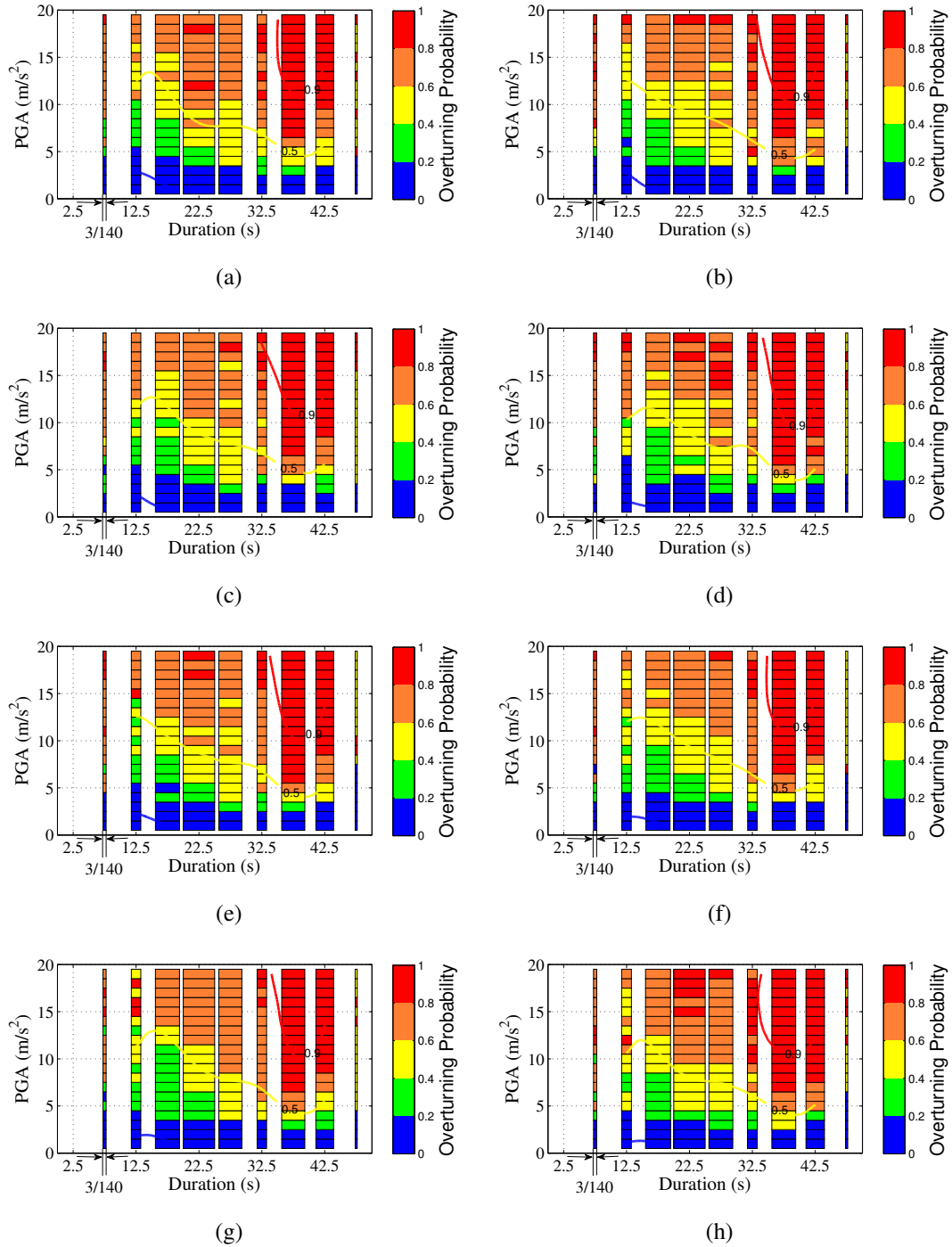


Figure C.4: Overturning probability of the Echo Cliff PBR as a function of PGA and duration for dominant horizontal ground motion applied to the pedestal at (a) 0° , (b) 45° , (c) 90° , (d) 135° , (e) 180° , (f) 225° , (g) 270° , and (h) 315° CCW from the X axis. Each row in these figures contain 140 earthquake records scaled to a given PGA level. The column thicknesses are proportional to the fraction of earthquakes (out of 140) that are sampled in a given duration bin.

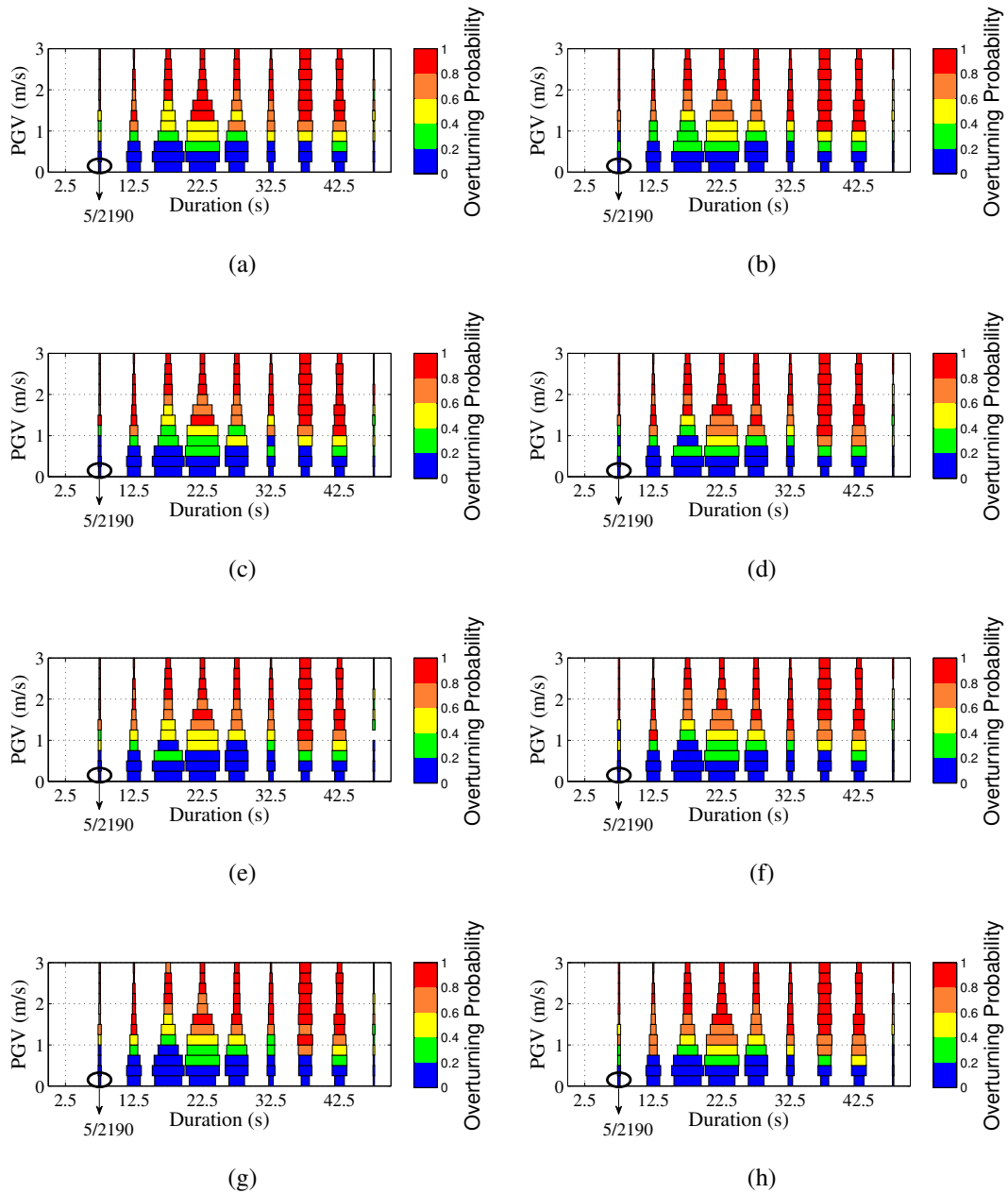


Figure C.5: Overturning probability of the Echo Cliff PBR as a function of PGV and duration for dominant horizontal ground motion applied to the pedestal at (a) 0° , (b) 45° , (c) 90° , (d) 135° , (e) 180° , (f) 225° , (g) 270° , and (h) 315° CCW from the X axis. 2190 out of the 2660 scaled earthquake records which have PGV less than 3 m/s and duration less than 50 s are used for these figures. The 2190 earthquakes are divided into bins of width 0.25 m/s in PGV and 5 s in duration. The varying thicknesses of the column are proportional to the fraction of earthquakes (out of 2190) that are sampled in a given PGV and duration bin.

Bibliography

- [1] Insight3d. <http://insight3d.sourceforge.net/>.
- [2] PhotoModeler. <http://www.photomodeler.com/index.html>.
- [3] ASCE/SEI Standard 43-05. Seismic design criteria for structures, systems and components in nuclear facilities. *American Society of Civil Engineers and Structural Engineering Insitute*.
- [4] B. T. Aagaard, T.M. Brocher, D. Dolenc, D. Dreger, R. W. Graves, S. Harmsen, S. Hartzell, S. Larsen, K. McCandless, S. Nilsson, N. A. Petersson, A. Rogers, B. Sjogreen, and M. L. Zoback. Ground motion modeling of the 1906 San Francisco earthquake, part II: Ground motion estimates for the 1906 earthquake and scenario events. *Bulletin of the Seismological Society of America*, 98(2):1012–1046, 2008.
- [5] B. T. Aagaard, T.M. Brocher, D. Dolenc, D. Dreger, R. W. Graves, S. Harmsen, S. Hartzell, S. Larsen, K. McCandless, S. Nilsson, N. A. Petersson, A. Rogers, B. Sjogreen, and M. L. Zoback. Data files for ground motion simulations of the 1906 San Francisco earthquake and scenario earthquakes on the Northern San Andreas fault. <http://pubs.usgs.gov/ds/413/>, 2009.
- [6] N.A. Abrahamson and W.J. Silva. Summary of the Abrahamson and Silva NGA ground-motion relations. *Earthquake Spectra*, 24(1):67–97, 2008.
- [7] R. H. Allen and X. Duan. Effects of linearizing on rocking-block toppling. *Journal of Structural Engineering*, 121(5):1146–1149, 1995.

- [8] J. G. Anderson. Quantitative measure of goodness of fit of synthetic seismographs. In *Proceedings of the 13th World Conference on Earthquake Engineering, August 1-6, 2004, Vancouver, B.C., Canada, 2004*.
- [9] A. Anooshehpour, J. N. Brune, and Y. Zeng. Methodology for obtaining constraints on ground motion from precariously balanced rocks. *Seismological society of America Bulletin*, 94(1):285–303, 2004.
- [10] A. Anooshehpour, T. H. Heaton, B. Shi, and J.N. Brune. Estimates of the ground accelerations at Point Reyes station during the 1906 San Francisco earthquake. *Bulletin of the Seismological Society of America*, 89(4):845–853, 1999.
- [11] M. Aslam, W. G. Godden, and D. T. Scalise. Earthquake rocking response of rigid bodies. *Journal of Structural Engineering*, 106(2):377–392, 1980.
- [12] K. Aydin. Rocking response of unanchored rectangular rigid bodies to simulated earthquakes. *Structural Engineering and Mechanics*, 18(3):343–362, 2004.
- [13] D. Baraff. Fast contact force computation for nonpenetrating rigid bodies. In *Computer Graphics Proceedings(SIGGRAPH)*, 1994.
- [14] P. Bazzurro and C. A. Cornell. Vector-valued probabilistic seismic hazard analysis. In *Proceedings 7th U.S. National Conference on Earthquake Engineering, Boston, MA, July 21-25, 2002, 2002*.
- [15] J. W. Bell, J. N. Brune, T. Liu, M. Zerda, and J. C. Yount. Dating the precariously balanced rocks in seismically active parts of California and Nevada. *Geology*, 26:495–498, 1998.
- [16] J. Bender, D. Finkenzeller, and A. Schmitt. An impulse-based dynamic simulation system for VR applications. In *Proceedings of Virtual Concept 2005(Biarritz, France, 2005), Springer, 2005*.

- [17] J. Bender and A. Schmitt. Constraint-based collision and contact handling using impulses. In *Proceedings of the 19th international conference on computer animation and social agents (Geneva (Switzerland))*, pages 3–11, 2006.
- [18] P. Bierman, A. Gillespie, M. Caffee, and D. Elmore. Estimating corrosion rates and exposure ages with ^{36}Cl produced by neutron activation. *Geochimica et Cosmochimica Acta*, 59:3779–3798, 1995.
- [19] G.S. Bjorkman. Influence of ISFSI design parameters on the seismic response of dry storage casks. In *Proceedings of the Packaging and Transport of Radioactive Materials Conference, London*, 2010.
- [20] Boore and W.J. Silva. Boore-Atkinson NGA ground motion relations for the geometric mean horizontal component of peak and spectral ground motion parameters. *Pacific Earthquake Engineering Research Center*, 2008.
- [21] D. M. Boore. Strong-motion recordings of the California earthquake of April 18, 1906. *Bulletin of the Seismological Society of America*, 67(3):561–577, 1977.
- [22] B.A. Bradley and M. Cubrinovski. Near-source strong ground motions observed in the 22 February 2011 Christchurch earthquake. *Seismological Research Letters*, 82(6), 2011.
- [23] J. J. Braverman, J. Xu, B. R. Ellingwood, C. J. Costantino, R. J. Morante, and C. H. Hofmayer. Evaluation of the seismic design criteria in ASCE/SEI standard 43-05 for application to nuclear power plants. *NUREG/CR-6926*, 2007.
- [24] B. Bruhn and B. P. Koch. Heteroclinic bifurcations and invariant manifolds in rocking dynamics. *Zeitschrift für Naturforschung*, 46:481–490, 1991.
- [25] J. N. Brune. Precariously balanced rocks and ground motion maps for southern California. *Seismological society of America Bulletin*, 86(1A):43–54, 1996.

- [26] J. N. Brune, A. Anooshehpour, M. D. Purvance, and R. J. Brune. Band of precariously balanced rocks between Elsinore and San Jacinto, California, fault zones: Constraints on ground motion for large earthquakes. *Geology*, 34(3):137–140, 2006.
- [27] J. Byerlee. Friction of rocks. *Pure and applied geophysics*, 116(4-5):615–628, 1978.
- [28] K. W. Campbell and Y. Bozorgnia. NGA ground motion model for the geometric mean horizontal component of PGA, PGV, PGD and 5% damped linear elastic response spectra for periods ranging from 0.01 to 10 s. *Earthquake Spectra*, 24(1):139–171, 2008.
- [29] A. Cayley. Sur quelques propriétés des déterminants gauches. *Journal für die Reine und Angewandte Mathematik*, 32:119–123, 1846.
- [30] M. N. Chatzis and A. W. Smyth. Modeling of the 3D rocking problem. *Journal of Non-Linear Mechanics*, 47(4):85–98, 2012.
- [31] M. N. Chatzis and A. W. Smyth. Three-dimensional dynamics of a rigid body with wheels on a moving base. *Journal of Engineering Mechanics*, 139(4):496–511, 2013.
- [32] H. A. Coombs, W. G. Milne, O. W. Nuttli, and D. B. Slemmons. Report of the review panel on the Decemeber 14, 1872 earthquake. *A report to the utilities of the Pacific Northwest*, 1976.
- [33] R.W. Cottle and G.B. Dantzig. *Complementary pivot theory of mathematical programming*. 1968.
- [34] R.W. Cottle, J.S. Pang, and R.E. Stone. *The Linear Complementarity Problem*. 1992.
- [35] P. A. Cundall. Formulation of a three-dimensional distinct element model. Part I: A scheme to detect and represent contacts in a system composed of many polyhedral blocks. *International Journal of Rock Mechanics*, 25(3):107–116, 1988.

- [36] B. Delaunay. Sur la sphère vide. a la mémoire de georges voronoi. *Bulletin de l'Académie des Sciences de l'URSS. Classe des sciences mathématiques et na*, 6:793–800, 1934.
- [37] A. B. Dickenson, R. Graves, T. Wurm, and A. Graves. Narrow gauge to the Redwoods. *Trans-Angle Books, Glendale, California*, 1967.
- [38] G. Farkas. Über die theorie der einfachen ungleichungen. *Journal für die Reine und Angewandte Mathematik*, 124:1–27, 1902.
- [39] E. Field, G. Biasi, P. Bird, T. Dawson, K. Felzer, D. Jackson, K. Johnson, T. Jordan, C. Madden, A. Michael, K. Milner, M. Page, T. Parsons, P. Powers, B. Shaw, W. Thatcher, I. Weldon, and Y. Zeng. Uniform California Earthquake Rupture Forecast, version 3 (UCERF3) the time-independent model. *U.S. Geological Survey Open-File Report 20131165*, 2013.
- [40] M. Fleisher, T. Liu, W. S. Broecker, and W. Moore. A clue regarding the origin of rock varnish. *Geophysical Research Letters*, 26:103–106, 1995.
- [41] D. Garcia and T. Soong. Sliding fragility of block-type non-structural components. *Earthquake Engineering and Structural Dynamics*, 32:111–129, 2003.
- [42] V. Graizer, C.G. Munson, and Y. Li. North Anna nuclear power plant strong-motion records of the Mineral, Virginia, earthquake of 23 August 2011. *Seismological Research Letters*, 84(3):551–557, 2013.
- [43] R. W. Graves, B.T. Aagaard, and K. W. Hudnut. The ShakeOut Earthquake source and ground motion simulations. *Earthquake Spectra*, 27(2):273–291, 2011.
- [44] Itasca Consulting Group. 3DEC (Three dimensional discrete element code). <http://www.itascacg.com/software/3dec>, 2008.
- [45] R. Hart, P. A. Cundall, and J. Lemos. Formulation of a three-dimensional distinct element model. Part I: Mechanical calculations for motion and interaction of a system

composed of many polyhedral blocks. *International Journal of Rock Mechanics*, 25(3):117–125, 1988.

- [46] Youssef Hashash. DEEPSOIL. <https://nees.org/resources/866>, 2012.
- [47] D.A. Heacock and E.S. Grecheck. Dominion North Anna power station restart readiness. 2011.
- [48] S. Hogan. On the dynamics of rigid-block motion under harmonic forcing. *Proceedings of the Royal Society of London*, 425:441–476, 1989.
- [49] S. Hogan. The many steady state responses of a rigid block under harmonic forcing. *Earthquake Engineering and Structural Dynamics*, 19(7):1057–1071, 1990.
- [50] S. Hogan. Slender rigid block motion. *Journal of Engineering Mechanics*, 120(1):11–24, 1994.
- [51] S. Hough, T. Taniguchi, and Altidor J.R. Estimation of peak ground acceleration from horizontal rigid body displacement: A case study in Port-au-Prince, Haiti. *Bulletin of the Seismological Society of America*, 102(6):2704–2713, 2012.
- [52] G. W. Housner. The behavior of inverted pendulum structures during earthquakes. *Bulletin of the Seismological Society of America*, 53(2):403–417, 1963.
- [53] K. W. Hudnut, B.T. Aagaard, R. W. Graves, L. Jones, T. Jordan, L. Star, and J. Stewart. ShakeOut Earthquake source description, surface faulting and ground motions. *United States Geological Survey Open File Rep 1150*, 2008.
- [54] K. W. Hudnut, W. Amidon, G. Bawden, J. Brune, S. Bond, R. Graves, D. E. Haddad, A. Limaye, D. K. Lynch, D. A. Phillips, E. Pounders, and D. Rood. The Echo Cliffs precariously balanced rock: Discovery and terrestrial laser scanning. In *SCEC 2009 Annual Meeting*, pages Poster 1–044. Southern California Earthquake Center, 2009.
- [55] I.M. Idriss. Empirical model for estimating the average horizontal values of pseudo-absolute spectral accelerations generated by crustal earthquakes. *Interim report for USGS Review*, 2007.

- [56] R. Ikegami and F. Kishinouye. A study on the overturning of rectangular columns in the case of the Nankai Earthquake on December 21, 1946. *Bulletin of Earthquake Research Institute*, 25:49–55, 1947.
- [57] R. Ikegami and F. Kishinouye. The acceleration of earthquake motion deduced from overturning of the gravestones in case of the Imaichi Earthquake on December 26, 1949. *Bulletin of Earthquake Research Institute*, 28:121–128, 1950.
- [58] Y. Ishiyama. Review and discussions on the overturning of bodies by earthquake motions. *BRI Research Paper No. 85, Ministry of Construction*, pages 1–115, 1980.
- [59] Y. Ishiyama. Motions of rigid bodies and criteria for overturning by earthquake excitations. *Earthquake Engineering and Structural Dynamics*, 10:635–650, 1982.
- [60] R. N. Iyengar and C. S. Manohar. Rocking response of rectangular rigid blocks under random noise base excitations. *International Journal of Non-Linear Mechanics*, 26(6):885–892, 1991.
- [61] S. G. Johnson. The NLOpt nonlinear-optimization package. <http://ab-initio.mit.edu/nlopt>.
- [62] D.S. Jordan. The earthquake rift of 1906. In *The California Earthquake of 1906, 1907*.
- [63] M. Kaneko and Y. Hayashi. A proposal for simple equations to express a relation between overturning ratios or rigid bodies and input excitation. In *Proceedings and Abstracts of the 13th World Conference on Earthquake Engineering, August 1-6, 2004, Vancouver, B.C., Canada, 2004*.
- [64] T.R. Kimura and K. Iida. On the rocking of rectangular columns (I). *Zisin*, 6(3):125–149, 1934.
- [65] T.R. Kimura and K. Iida. On the rocking of rectangular columns (II). *Zisin*, 6(4):165–212, 1934.

- [66] P. Kirkpatrick. Seismic measurements by the overthrow of columns. *Bulletin of Seismological Society of America*, 17(2):95–109, 1927.
- [67] M. D. Kohler, H. Magistrale, and R. W. Clayton. Mantle heterogeneities and the SCEC reference three- dimensional seismic velocity model version 3. *Bulletin of the Seismological Society of America*, 93(2):757–774, 2003.
- [68] D. Kraft. Algorithm 733: TOMP-Fortran modules for optimal control calculations. *ACM Transactions on Mathematical Software*, 20(3):262–281, 1994.
- [69] A. Lawson and H. Reid. The California earthquake of April 18, 1906. *Report of the State Earthquake Investigation Commisiion*, 1908.
- [70] S. Lenci and G. Rega. Overturning thresholds of a rocking block subjected to harmonic excitation: Computer simulations and analytic treatment. In *Proceedings of the International Mechanical Engineering Congress, Washington, D.C., November 15-21, 2003*.
- [71] H. Lin and S. Yim. Nolinear rocking motions. I: Chaos under noisy periodic excitations. *Journal of Engineering Mechanics*, 122(8):719–727, 1996.
- [72] D. L. Linton. The problem of tors. *Geographical Journal*, 121(4):470–487, 1955.
- [73] T. Liu. Blind testing of rock varnish microstratigraphy as a chronometric indicator: results on late Quaternary lava flows in the Mojave Desert, California. *Geomorphology*, 53:209–234, 2003.
- [74] A. Lomax. A reananlysis of the hypocentral location and related observations for the great 1906 California earthquake. *Bulletin of the Seismological Society of America*, 95:861–877, 2005.
- [75] P. Lötstedt. Numerical simulation of time-dependent contact and friction problems in rigid body mechanics. *SIAM Journal on Scientific and Statistical Computing*, 5(2):370–393, 1984.

- [76] V.K. Luk, B.W. Spencer, and I.P. Lam. Parametric evaluation of seismic behavior of freestanding spent fuel dry cask storage systems. *Sandia National Laboratories*, 2005.
- [77] H. Magistrale, S. Day, R. W. Clayton, and R. Graves. The SCEC southern California reference three- dimensional seismic velocity model version 2. *Bulletin of the Seismological Society of America*, 90(6B):S65–S76, 2000.
- [78] H. Magistrale, K. McLaughlin, and S. Day. A geology-based 3D velocity model of the Los Angeles basin sediments. *Bulletin of the Seismological Society of America*, 86(4):1161–1166, 1996.
- [79] N. Makris and Y. Rousson. Rocking response and overturning of equipment under horizontal pulse-type motions. *PEER Report*, 1998.
- [80] R. Mallet. The Great Neopolitan Earthquake of 1857. *London: Chapman and Hall*, 1862.
- [81] J. P. McCalpin. Application of paleoseismic data to seismic hazard assessment and neotectonic research. *International Geophysics*, 95, 2009.
- [82] J. Milne and F. Omori. On the overturning and fracturing of brick and other columns by horizontally applied motion. *Seismological Journal of Japan*, 1:59–85, 1893.
- [83] T. Mochizuki and K. Kobayashi. A study on the acceleration of earthquake motion deduced from the movement of a column: An analysis on the movement of a column. *Transactions of AIJ*, 248:63–70, 1862.
- [84] R. Mourhatch and S. Krishnan. Risk analysis using rupture-to-rafter simulations: Inferring probabilities of scenario earthquakes from the Uniform California Earthquake Rupture Forecast (in submission). *Seismological Research Letters*, 2015.
- [85] N. M. Newmark and W. J. Hall. Earthquake spectra and design. *Earthquake Engineering Research Institute: El Cerrito, California*, 1982.

- [86] Petersen, D. Mark, Frankel, D. Arthur, Harmsen, C. Stephen, Mueller, S. Charles, Haller, M. Kathleen, Wheeler, L. Russell, Wesson, L. Robert, Zeng, Yuehua, Boyd, S. Oliver, Perkins, M. David, Luco, Nicolas, Field, H. Edward, Wills, J. Chris, Rukstales, and S. Kenneth. Documentation for the 2008 update of the united states national seismic hazard maps. *United States Geological Survey Open-File Report 20081128*, 2008.
- [87] R. Plaut, W. Fielder, and L. Virgin. Fractal behavior of an asymmetric rigid block overturning due to harmonic motion of a tilted foundation. *Chaos, Solitons and Fractals*, 7(2):177–196, 1996.
- [88] M. Purvance, A. Anooshehpour, and J. N. Brune. Freestanding block overturning fragilities: Numerical simulation and experimental validation. *Earthquake Engineering and Structural Dynamics*, 37:791–808, 2008.
- [89] M. Purvance, A. Anooshehpour, and J. N. Brune. Fragilities of sensitive geological features on Yucca mountain, Nevada. *PEER report*, 2009.
- [90] M. Purvance, J. Brune, A. Anooshehpour, and R. Brune. Evidence of large fault parallel/perpendicular PGV ratios. In *Proceedings and Abstracts of the Southern California Earthquake Center 2004 Annual Meeting*, 2004.
- [91] M. D. Purvance. Overturning of slender blocks: Numerical investigation and application to precariously balanced rocks in Southern California. In *Ph.D. Dissertation, University of Nevada, Reno*, 2005.
- [92] M. D. Purvance, J. N. Brune, N. A. Abrahamson, and J. G. Anderson. Consistency of precariously balanced rocks with probabilistic seismic hazard estimates in Southern California. *Bulletin of Seismological Society of America*, 98(6):2629–2640, 2008.
- [93] North Anna ISFSI SAR. North Anna independent spent fuel storage installation. In *Final Safety Analysis Report Revision 6*, 2008.
- [94] Y. Shao and C. Tung. Seismic response of temporary structures. *Nuclear Engineering Design*, 181:267–274, 1998.

- [95] H.W. Shenton. Criteria for initiation of slide, rock, and slide-rock rigid-body modes. *Journal of Engineering Mechanics*, 122:690–693, 1996.
- [96] B. Shi, A. Anooshehpour, Y. Zeng, and J. N. Brune. Rocking and overturning of precariously balanced rocks by earthquakes. *Seismological society of America Bulletin*, 86:1364–1371, 1996.
- [97] R. Smith. Open Dynamics Engine. <http://www/ode.org>, 2000.
- [98] S. G. Song, G. C. Beroza, and P. Segall. A unified source model for the 1906 San Francisco earthquake. *Bulletin of the Seismological Society of America*, 98(2), 2008.
- [99] P. D. Spanos and A. S. Koh. Rocking of rigid blocks due to harmonic shaking. *Journal of Engineering Mechanics*, 117:1627–1642, 1984.
- [100] T. Taniguchi and T. Miwa. A simple procedure to approximate slip displacement of freestanding rigid body subjected to earthquake motions. *Earthquake Engineering and Structural Dynamics*, 36:481–501, 2007.
- [101] B.P. Tripathi. SFST staff’s perspective on status of ISFSIs at North Anna nuclear power plant after the seismic event of August 23, 2011. In *2011 SFST Technical Exchange*, 2011.
- [102] W. K. Tso and C. M. Wong. Steady state rocking response of rigid blocks. Part 1: Analysis. *Earthquake Engineering and Structural Dynamics*, 18:89–106, 1989.
- [103] C. R. Twidale and E. M. Campbell. On the origin of pedestal rocks. *Zeitschrift für Geomorphologie*, 36:1–13, 1992.
- [104] USGS. Earthquake hazards 101 - the basics. <http://earthquake.usgs.gov/hazards/about/basics.php>.
- [105] E. Voyagaki, G. Mylonakis, and L. N. Psycharis. Rigid block sliding to idealized acceleration pulses. *Journal of Engineering Mechanics*, 138:1071–1083, 2012.

- [106] E. Voyagaki and D. Vamvatsikos. Probabilistic characterization of overturning capacity for simply-supported rigid blocks. In *Proceedings of the Second European Conference on Earthquake Engineering and Seismology, Istanbul, August 25-29, 2014*, 2014.
- [107] D.J. Wald, V. Quitoriano, Heaton T.H., and H. Kanamori. Relationships between peak ground acceleration, peak ground velocity, and modified mercalli intensity in california. *Earthquake Spectra*, 15:557–564, 1999.
- [108] D. Weichert. Omak rock and the 1872 Pacific Northwest earthquake. *Seismological society of America Bulletin*, 84(2):444–450, 1994.
- [109] R. Weinstein, J. Teran, and R. Fedkiw. Dynamic simulation of articulated rigid bodies with contact and collision. *IEEE Transactions on Visualization and Computer Graphics*, 12(3):365–374, 2006.
- [110] C. M. Wong and W. K. Tso. Steady state rocking response of rigid blocks. Part 2: Experiment. *Earthquake Engineering and Structural Dynamics*, 18:107–120, 1989.
- [111] C. Yim, A. K. Chopra, and J. Penzien. Rocking response of rigid blocks to earthquakes. *Earthquake Engineering and Structural Dynamics*, 8:565–587, 1980.
- [112] C. S. Yim and H. Lin. Chaotic behavior and stability of free-standing offshore equipment. *Ocean Engineering*, 18(3):225–250, 1991.
- [113] C. S. Yim and H. Lin. Nonlinear impact and chaotic response of slender rocking objects. *Journal of Engineering Mechanics*, 117(9):2079–2099, 1991.
- [114] C. S. Yim and H. Lin. Nonlinear impact and chaotic response of slender rocking objects. *Journal of Engineering Mechanics*, 117(9):2079–2099, 1991.
- [115] J. Zhang and N. Makris. Rocking response of free-standing blocks under cycloidal pulses. *Journal of Engineering Mechanics*, 127:473–483, 2001.